AD-A032 389 AIR FORCE AERO PROPULSION LAB WRIGHT-PATTERSON AFB OHIO F/G 20/4
HEAT ADDITION TO A SUPERSONIC FLOW.(U)
OCT 76 W C BURSON
UNCLASSIFIED AFAPL-TR-76-57 NL

1 OF 2
ADA032389

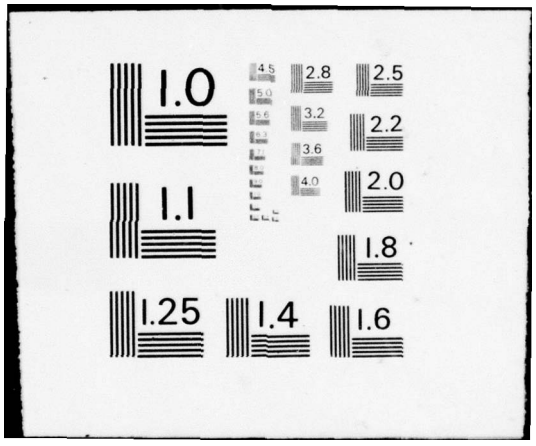
1.0
1.1
1.25
1.4
1.6
1.8
2.0
2.2
2.5
2.8
3.2
3.6
4.0
4.5
5.0
5.6

AD A032389

AFAPL-TR-76-57

HEAT ADDITION TO A SUPERSONIC FLOW

RAMJET APPLICATIONS BRANCH
RAMJET ENGINE DIVISION

DDC
RECEIVED
NOV 23 1976
B

OCTOBER 1976

TECHNICAL REPORT AFAPL-TR-76-57
FINAL REPORT FOR PERIOD 1 SEPTEMBER 1972 to 1 JANUARY 1974

Approved for public release; distribution unlimited

AIR FORCE AERO PROPULSION LABORATORY
AIR FORCE WRIGHT AERONAUTICAL LABORATORIES
AIR FORCE SYSTEMS COMMAND
WRIGHT-PATTERSON AIR FORCE BASE, OHIO 45433

NOTICE

When Government drawings, specifications, or other data are used for any purpose other than in connection with a definitely related Government procurement operation, the United States Government thereby incurs no responsibility nor any obligation whatsoever; and the fact that the Government may have formulated, furnished, or in any way supplied the said drawings, specifications, or other data, is not to be regarded by implication or otherwise as in any manner licensing the holder or any other person or corporation, or conveying any rights or permission to manufacture, use, or sell any patented invention that may in any way be related thereto.

This report has been reviewed by the Information Office, (ASD/OIP) and is releasable to the National Information Service (NTIS). At NTIS, it will be available to the general public, including foreign nations.

This technical report has been reviewed and is approved for publication.

Dr. William C. Burson Jr.
DR. WILLIAM C. BURSON, Jr., GS-13
Aerospace Engineer
Ramjet Applications Branch
Ramjet Engine Division

FOR THE COMMANDER

William E Supp
WILLIAM E. SUPP, Technical Manager
Strategic Missile Propulsion
Ramjet Applications Branch
Ramjet Engine Division

Copies of this report should not be returned unless return is required by security considerations, contractual obligations, or notice on a specific document.

AIR FORCE - 8 NOVEMBER 76 - 125

Unclassified

SECURITY CLASSIFICATION OF THIS PAGE (When Data Entered)

REPORT DOCUMENTATION PAGE

READ INSTRUCTIONS BEFORE COMPLETING FORM

1. REPORT NUMBER: AFAPL-TR-76-57	2. GOVT ACCESSION NO.
3. RECIPIENT'S CATALOG NUMBER	
4. TITLE (and Subtitle): Heat Addition to a Supersonic Flow	5. TYPE OF REPORT & PERIOD COVERED: Final rept. 1 Sep 1972 - 1 Jan 1974
6. PERFORMING ORG. REPORT NUMBER	
7. AUTHOR(s): Dr. William C. Burson, Jr.	8. CONTRACT OR GRANT NUMBER(s): 14
9. PERFORMING ORGANIZATION NAME AND ADDRESS: AFAPL/RJA, Wright-Patterson AFB, Ohio 45433	10. PROGRAM ELEMENT, PROJECT, TASK AREA & WORK UNIT NUMBERS: 62203F 30121403
11. CONTROLLING OFFICE NAME AND ADDRESS: Air Force Aero Propulsion Laboratory, Ramjet Engine Division, AFAPL/RJA, Wright-Patterson AFB, OH 45433	12. REPORT DATE: October 1976
	13. NUMBER OF PAGES: 145
14. MONITORING AGENCY NAME & ADDRESS (if different from Controlling Office): 156p.	15. SECURITY CLASS. (of this report): Unclassified
	15a. DECLASSIFICATION/DOWNGRADING SCHEDULE: N/A

16. DISTRIBUTION STATEMENT (of this Report)

Approved for public release; distribution unlimited.

17. DISTRIBUTION STATEMENT (of the abstract entered in Block 20, if different from Report)

18. SUPPLEMENTARY NOTES

19. KEY WORDS (Continue on reverse side if necessary and identify by block number)

Supersonic Flow
Jet Propulsion
Plasma Flow
Gas Dynamics

20. ABSTRACT (Continue on reverse side if necessary and identify by block number)

Advanced propulsion engines of the future, which may fly at Mach numbers greater than five, will depend upon the supersonic heat addition process for efficient operation. In supersonic heat addition, the gas flow remains supersonic before, during, and after the heating process. The advantages of supersonic heat addition compared to subsonic heat addition are a lower static temperature and a lower static pressure for a given energy input.

Two supersonic heat addition modes are available. One is the subsonic diffusion flame propagating into a supersonic flow where the normal or

→ next page

Continued . . .

DD FORM 1 JAN 73 1473 EDITION OF 1 NOV 65 IS OBSOLETE

Unclassified

SECURITY CLASSIFICATION OF THIS PAGE (When Data Entered)

011570 AB

perpendicular component of the flow velocity with respect to the flame front is subsonic. The disadvantage of the subsonic diffusion flame is the relatively long combustor length resulting from the subsonic normal component of the flow velocity. The other supersonic heat addition mode is a weak detonation wave where the thermal wave or flame front is supersonic relative to the heated and unheated gas. The purpose of this effort was to experimentally investigate the weak detonation wave by simulating it in a gas flow and a water flow. The gas flow weak detonation wave was produced by radio frequency (R.F.) heating of a supersonic Argon flow using an R.F. coil wrapped around a Boron Nitride duct. The water flow weak detonation wave was simulated by mass addition to a supersonic water stream.

A quasi-one-dimensional theory based on average properties was developed which can analyze axisymmetric duct flows with wall friction, varying area, heat addition, and mass exchange occurring simultaneously. The theory was used for comparison with the experimental results.

ACCESSION for
NTIS White Section ☒
DDC Buff Section ☐
UNANNOUNCED ☐
JUSTIFICATION
BY
DISTRIBUTION/AVAILABILITY CODES
Dist. AVAIL. and/or SPECIAL
A

FOREWORD

This report contains the results of an investigation of heat addition to a supersonic flow. The work was performed in the Ramjet Engine Division of the Air Force Aero Propulsion Laboratory, Air Force Systems Command, Wright-Patterson AFB, Ohio, under Project 3012, Task 14, and Work Unit 03. The work effort was conducted by William C. Burson, Jr., during the period September 1972 to January 1974. Mr. Stanley R. Double of AFAPL/TFP served as technician for the effort.

The author wishes to express here his gratitude to Professor R. Edse for the guidance and encouragement received as his advisor in the doctoral program at The Ohio State University. The author wishes also to give recognition to the Air Force Institute of Technology, particularly to Dr. Andrew Shine and Dr. Harold Wright of the Aerospace-Mechanical Engineering Department, who permitted the use of their water table test facility; to Mr. Stanley Double, the technician at AFAPL for his able assistance in preparing and performing many of the experiments; to Mr. Kenneth Johnston of the Air Force Computer Center for his assistance in preparing and debugging the computer programs used in this effort; and to Miss Cynthia Lines for the exceptionally well handled typing task.

TABLE OF CONTENTS

SECTION		PAGE
I	INTRODUCTION	1
II	BACKGROUND	4
III	THEORETICAL ANALYSIS	12
	Flow Equations	12
	Water Table Theory	41
	Electric Probe Theory	44
	R.F. Energy Addition	60
IV	EXPERIMENTAL EQUIPMENT AND PROCEDURE	64
	Gas Flow Apparatus	64
	Flow Measurement Probes	69
	Water Table Apparatus	78
V	EXPERIMENTS	83
	Water Table Experiments	83
	Gas Flow Experiments	90
VI	SUMMARY AND CONCLUSIONS	129
	Experiments	129
	Radial and Axial Variations	130
	Average Properties for Gas Experiments	133
	Conclusions	135
LIST OF REFERENCES		141

PRECEDING PAGE BLANK-NOT FILMED

LIST OF ILLUSTRATIONS

Figure		Page
1	Hugoniot and Rayleigh Curves for Heat Addition	7
2	Mass Flow Ratio vs. Area Ratio	28
3	Mass Flow Ratio vs. Mach Number.	29
4	Area Ratio vs. Mach Number	30
5	Total Temperature Ratio vs. Mach Number.	31
6	Static Temperature Ratio vs. Mach Number	32
7	Static Pressure Ratio vs. Mach Number.	33
8	Total Pressure Ratio vs. Mach Number	34
9	Velocity Ratio vs. Mach Number	35
10	Total Temperature Ratio vs. Mach Number.	36
11	Area Ratio vs. Mach Number	37
12	Static Temperature Ratio vs. Mach Number	38
13	Static Pressure Ratio vs. Mach Number.	39
14	Velocity Ratio vs. Mach Number	40
15	Schematic of the Langmuir Probe Characteristic Curve	46
16	Voltage-Current Characteristic of the Double Probe	48
17	General Potential Diagram for the DPM	48
18	Comparison of Experimental and Theoretical DPM Traces	50
19	Domain of Validity for Probe Theories With Data Points Shown.	52
20	Schematic of Power Circuit	66

LIST OF ILLUSTRATIONS (CONTD)

Figure		Page
21	Test Apparatus	66
22	Photograph of Test Apparatus With Power Input to the Gas	67
23	Photograph of Apparatus for Supersonic Gas Flow Energy Addition Tests	68
24	Pressure Probes	70
25	Static and Total Pressure Probes Along Side of a Boron Nitride Duct	70
26	Pressure Measurement Schematic	72
27	Total Temperature Probe Schematic	74
28	Double Probe	75
29	Double Probe Schematic	76
30	Schematic of Double Probe Circuit	77
31	Schematic of Collector	79
32	Collector As Seen Inside the Vacuum Chamber. To the Right Is the Port In Which the Collector Is Placed During Gas Flow Tests	79
33	Water Table Schematic	80
34	Water Table with Nozzle Direct-Connect Duct and Porous Injection Plate	81
35	Water Table Test with Free Inlet Duct	81
36	Water Table Results	84
37	Side View of Duct Directly Connected to Nozzle	85
38	Mass Addition or Heat Addition Greater Than in Figure 37	85
39	Side View of Free Inlet Duct Without and With Mass Addition (Heat) Addition	86
40	Side View of Free Inlet Duct. Mass Addition Greater Than in Figure 39	87
41	Side View of Free Inlet Duct. Mass Addition Greater Than in Figure 40	87

LIST OF ILLUSTRATIONS (CONTD)

Figure		Page
42	Side View. No Mass Addition and Ink in Water.	88
43	No Mass Addition. Length of Duct Extended Illustrating the Effect of Friction	88
44	Static Press. vs. Axial Position	89
45	Varying Area Duct for Heat Addition.	91
46	Pressure for Wall Taps & Static Pressure Probe	95
47	Pressure Measured by Wall Taps	96
48	Pressure Measured by Wall Taps	98
49	Probes In Flow At Duct Exit.	98
50	Mach Number vs. Radial Position.	101
51	Mach Number vs. Radial Position.	102
52	Average Mach No. vs. Axial Position.	103
53	Average Press. Ratio vs. Axial Position.	104
54	Static Press. Ratio vs. Radial Position.	105
55	Total Press. Ratio vs. Radial Position	106
56	Average Total Press. Ratio vs. Axial Position.	107
57	Static Temp. Ratio vs. Radial Position	108
58	Static Temp. Ratio vs. Radial Position	109
59	Total Temp. Ratio vs. Radial Position.	110
60	Total Temp. Ratio vs. Radial Position.	111
61	Velocity Ratio vs. Radial Position	112
62	Density Ratio vs. Radial Position.	113
63	Watts Per Sq. Inch vs. Radial Position	114
64	Mass Flow Ratio vs. Radial Position.	115
65	Total Pressure vs. Total Temperature Ratio for Constant Area and Diverging Ducts	136

LIST OF ILLUSTRATIONS (CONCL'D)

Figure — Page

66 Mass Flow Ratio Caused by Heat Addition vs. Total Temperature Ratio for Constant Area & Diverging Ducts 137

LIST OF TABLES

Table

1 T^{o} - Measured By Probe. 93

2-4 Comparison of Experiment and Theory Constant Area Duct. 116

5-7 Comparison of Experiment and Theory Area Ratio of 1.60. 119

8-10 Comparison of Experiment and Theory Area Ratio of 2.0 122

11 Double Probe Data For Three Total Temperature Ratios as a Function of Radial Position. Constant Area Duct 128

LIST OF SYMBOLS (CONCL'D)

RO	Duct Radius
S	Entropy
T	Static Temperature
T_e	Electron Temperature
T_i	Ion Temperature
T^o	Total Temperature
T_o	Total Temperature
u	Velocity
V	Velocity, Voltage
v	Specific Volume
x	Distance or Displacement
y	Mass Injection Velocity Component Parallel to Main Flow Divided by the Main Flow Velocity
ϕ	Compressor Ratio
ϕ	4f + 4m (1-y)n
ρ	Density
ρ_p	r_p/λ_D
γ	Ratio of Specific Heats
θ	Divergence or Convergence Angle
α	Degree of Ionization
λ_D	Debye Length
λ_c	Mean Free Path
μ	Mobility
ν	Collision Frequency
ω	Power Source Frequency
ε_o	Permittivity

LIST OF SYMBOLS (CONT'D)

k	Boltzman's Constant
K.E.	Kinetic Energy
l	Length of Tungsten Wire
L	Duct Length
LN	n
Ln	Natural Logarithm
m	2 tanθ
m_i	Ion Mass
m_e	Electron Mass
m_n	Neutral Particle Mass
$\dot{m}$	Mass Flow Rate
M	Mach Number
n	Variable Parameter
n_o	Ion Particle Density
n_e	Electron Particle Density
n_m	Metastable Number Density
N	Variable Parameter, Power Setting
P	Static Pressure, Power Density
Pow	Power
P^o	Total Pressure
PH	f/tanθ
Q	Specific Energy Input to the Gas
q	Water Mass Injection Term
r	Recovery Factor
r_p	Probe Radius
R	Radius

LIST OF SYMBOLS

A	Area
$\bar{c}_i$	Ion Average Velocity
C_p	Specific Heat at Constant Pressure
C_v	Specific Heat at Constant Volume
D	Diameter
e	Electronic Charge
E_a	Effective Applied Electric Field
E_m	Energy Difference Between Metastable and Ionization Level
EV	Recombination Energy
f	Friction Factor
F	Froude Number
g	Gravity Acceleration
g_m	Statistical Weight of Metastable State
g_i	Statistical Weight of Ion Ground State
g_e	Statistical Weight of an Electron
G	Ratio of Specific Heats
h	Water Height, Enthalpy, Planck's Constant
i	Electric Current
I_+	Ion Saturation Current
I	Axial Duct Position
J	Current Density

SECTION I
INTRODUCTION

Advanced propulsion engines of the future, which may fly at Mach numbers greater than five, will depend upon the supersonic heat addition process for efficient operation. In supersonic heat addition, the gas flow remains supersonic before, during, and after the heating process. The advantages of supersonic heat addition compared to subsonic heat addition are a lower static temperature and a lower static pressure for a given energy input. The lower pressure and temperature provide a less severe structural requirement for the vehicle; also, the lower temperature results in less dissociation of the gas. Dissociation is an energy loss if recombination does not occur within the engine.

Two supersonic heat addition modes are available. One is the subsonic diffusion flame propagating into a supersonic flow where the normal or perpendicular component of the flow velocity with respect to the flame front is subsonic. The disadvantage of the subsonic diffusion flame is the relatively long combustor length resulting from the subsonic normal component of the flow velocity. The other supersonic heat addition mode is a weak detonation wave where the thermal wave or flame

front is supersonic relative to the heated and unheated gas. Supersonic flame speeds are virtually impossible to obtain by thermal ignition but may be possible by photochemical ignition. The advantage of the weak detonation wave is the short combustor length that it would require.

The purpose of this effort was to experimentally investigate the weak detonation wave by simulating it in a gas flow and a water flow. The gas flow weak detonation wave was produced by radio frequency (R.F.) heating of a supersonic Argon flow using an R.F. coil wrapped around a Boron Nitride duct. The coil length represents the wave region since the heating is by electrons which is quite rapid. Comparison of the experimental measurements was made with a theoretical analysis. The water flow weak detonation wave was simulated by mass addition to a supersonic water stream. The water flow simulation was performed to determine if it could qualitatively predict what occurs in gas flow heat addition.

The water flow experiments were performed on a water table using a two-dimensional nozzle to simulate a Mach 2 exit flow. The "combustor" at the nozzle exit consisted of two plexiglas walls, one on each side of a porous injection plate that allowed mass injection to the main flow. The results of the water table experiments did predict the phenomena seen in the gas flow experiments.

Supersonic heat addition to supersonic Argon gas flow was achieved in constant area and varying area ducts. The low Reynolds number (35,000) of the flow caused some difficulty in obtaining good pressure measurements and permitted considerable upstream influence of the pressure rise generated by heat addition. A pressure rise and decrease within the duct was observed during heat addition. This pressure

variation within the duct could be caused by two phenomena. First, a separation region and reattachment could occur; and, second, due to the non-uniform radial energy addition, the rapid heating near the wall within the coil region causes a rapid expansion next to the wall, forcing more mass flow towards the center which effectively decreases the flow area. Downstream of the coil, radial heat conduction occurs, thus relieving the pressure. Measurements were made with a static pressure probe, a total pressure probe, a total temperature probe, and an electric double probe for determination of the ionization level. The degree of ionization had to be known in order to make a correction to the total temperature measurement.

A quasi-one-dimensional theory based on average properties was developed which can analyze axisymmetric duct flows with wall friction, varying area, heat addition, and mass exchange occurring simultaneously. The theory was used for comparison with the experimental results. Satisfactory agreement between theory and experiment was obtained if the average of the measured temperature was obtained by averaging with a radial mass flow variation rather than just averaging with the radius.

SECTION II

BACKGROUND

Heat addition to a supersonic flow is of great interest in the design of advanced propulsion systems. A thermodynamic analysis, based on the Brayton Cycle, shows that for the maximum exit Mach number or thrust of a jet engine the compressor pressure ratio (ϕ) approaches one when the flight Mach number (Ma) is 3.87 and the total temperature ratio (total temperature measured after heat input divided by the ambient air temperature, T_2°/T_a) is four. A total temperature ratio equal to four is based on limiting the uncooled turbine blade temperatures to 2000°R for an ambient temperature of 500°R. Of course, cooled turbine blades will allow higher flight Mach numbers than 3.87 for $\phi \rightarrow 1.0$ at the maximum thrust condition. The optimum compressor ratio for the above is:

$$\phi = \left\{ \frac{1}{2} \left[1 + \frac{T_2^{\circ}}{T_1^{\circ}} \cdot \frac{1}{1+\frac{\gamma-1}{2}M_a^2} \right] \right\}^{\gamma/\gamma-1}$$

A compressor ratio approaching one indicates that a ramjet instead of a turbojet engine should be used. The ramjet engine consists of an inlet, diffuser, burner, and exhaust nozzle. In the Mach 3 to 5 region, satisfactory operation of the ramjet is possible by means of supersonic diffusion through several oblique shocks which are followed by a normal shock and subsonic diffusion so that energy is added by subsonic combustion. The overall efficiency of the ramjet at Mach numbers of 5 and greater depends very much on the mode of heat addition. It appears that

the most advantageous process involves diffusion to a lower Mach number which is still supersonic while the energy addition or combustion occurs in this supersonic air stream.

The advantages of supersonic heat addition or combustion compared to the subsonic case are less chemical dissociation of the gases due to a lower static temperature, and a less severe structures requirement as a result of the lower static pressures and temperatures. Heat addition in a supersonic flow may lead to a strong detonation or a weak detonation wave as shown in Figure (1) which represents the pressure-specific volume relationships between initial and final state. The Rayleigh lines represent conditions of constant mass flow with varying energy exchange, while the Hugoniot curves represent (for a fixed energy input and initial static temperature and pressure) varying mass flow, Mach number, total temperatures, and final static temperature and pressure. The weak detonation mode represents a true supersonic combustion process, supersonic flame speed, which does not involve shock waves of any kind; the flows of both heated and unheated gases are supersonic. The only known example of a thermal initiated weak detonation is the phenomena of "knock" in a piston engine in which the combustion propagates almost at an infinite speed throughout the gas mixture. In the strong detonation, a normal shock precedes the combustion process so that energy addition takes place in the flow which is subsonic relative to the shock wave. The Chapman-Jouguet mode is the strong detonation case in which the Mach number of the flow after heat addition is one relative to the shock wave. Whereas the traveling strong detonation waves are easily obtained and have been the subject of many studies, stationary strong detonation waves resulting

from chemical energy release are very difficult to obtain or maintain because of difficulties in stabilizing the wave. Standing weak detonations in fuel-air mixtures are difficult to achieve because of the difficulty in obtaining ignition. Flame speed and ignition is a strong function of the static gas temperature and high static temperatures are difficult to obtain in a supersonic flow.

The final pressure and volume conditions denoted by "x" on Figure (1) can be reached by the weak detonation as discussed above or by a subsonic diffusion flame propagating in a supersonic stream. The weak and strong detonation modes can occur only in premixed mixtures of fuel and air. Combustion in non-premixed gas mixtures depend primarily on the rate of injection, mixing, diffusion of the fuel, and chemical kinetics. The length of the heat addition region for diffusion flames will be much longer than the weak detonation because of the processes of mixing and diffusion and the fact that the normal component of the flame velocity with respect to the incoming mixture does not propagate at a supersonic speed in diffusion flames which results in a small flame angle to the flow.

There is a wealth of papers dealing with the problem of energy addition to a supersonic flow and subsonic diffusion flames propagating in a supersonic stream. Only a few of the important ones will be referenced here.

Weber and MacKay [1] showed that if achieving sonic flow at the combustor exit was not possible due to structural or fuel limitations, then maintaining a shock free flow during energy addition is desirable for good overall engine efficiency. They also noted that the thrust and,

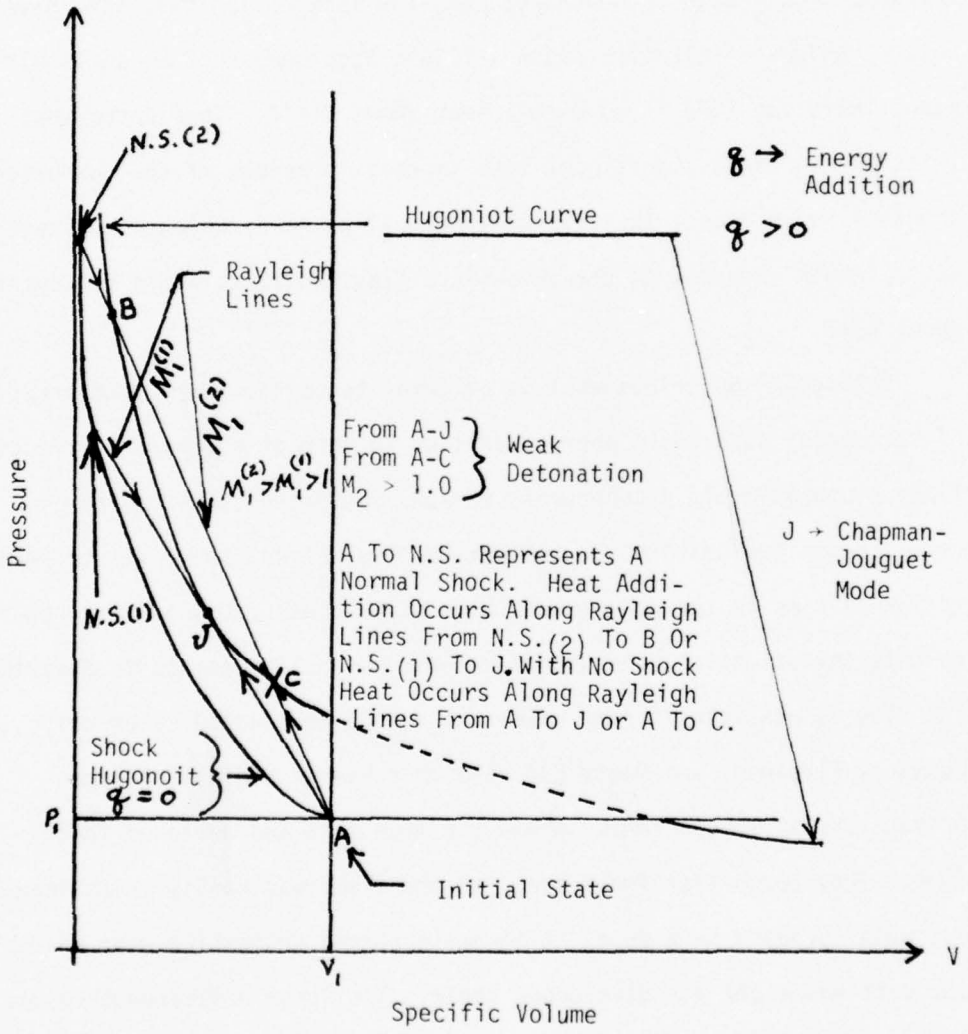

Figure (1). Hugoniot and Rayleigh Curves for Heat Addition.

in some cases, the engine efficiency can be increased by using a combustor with an increasing flow area. There exists a combustor temperature below which the supersonic combustion ramjet (SCRJ) has a better overall engine efficiency compared to the conventional ramjet (CRJ). Compared with a double cone inlet CRJ, the isentropic inlet SCRJ gives better engine efficiencies above a flight Mach number of 5, while with a wedge inlet the SCRJ is more efficient above M = 7. They noted that friction can cause significant loss in total pressure if the combustor length is very great; thus the weak detonation wave, which would have a short length compared to the subsonic diffusion flame, would be advantageous here.

Billig [2] describes what is believed to be the first demonstration of stationary supersonic energy addition in form of a subsonic diffusion flame propagating in a supersonic stream. He noted that the energy released was low compared to the maximum theoretical value due to short residence time in the experimental two-dimensional combustor. According to this investigation, the use of one-dimensional equations to describe the flow is possible in some cases but cannot be adopted "a priori". Cookson, Flanagan, and Penny [3] studied subsonic diffusion flames propagating in a supersonic stream for free jets and enclosed (duct) flow. They found that for a free jet the flame was easily maintained, but when enclosed in a duct, it became a strong detonation wave unless the duct had a certain divergence angle. Too large a divergence angle would extinguish the flame. They used a one-dimensional analysis for comparison with experiments where pressure and area ratios were exponential functions of distance or the area ratio is a function of the

pressure ratio (before and after energy addition) raised to some power. Their pressure measurements were within 5% of those predicted by the theory; the theory qualitatively agreed with the Mach number variation as a function of total temperature variation.

The weak detonation wave is difficult to generate in the laboratory with combustible mixtures since the absence of heating by a shock wave requires heating the mixture of a supersonic gas flow or a photochemical process to obtain ignition. The chemical reactions or burning must take place very fast (supersonic flame speed) if a weak detonation wave is to be produced. Heating of a supersonic flow of a fuel-air mixture is virtually impossible. Pre-heating a high enthalpy mixture in a stagnation reservoir before expansion may cause premature ignitions. Thus, an experimental investigation of a thermally-initiated weak detonation wave appears to be very difficult in the laboratory. Injection of the fuel into supersonic flow of the proper total temperature and Mach number will result in oblique shocks behind which subsonic diffusion flames propagate releasing a large amount of the energy in the region near the surface where injection takes place.

One possible approach for obtaining a weak detonation is by photochemical ignition of a combustible mixture. Thermal ignition delay times for fuel-air mixtures are rather long when static pressures and temperatures are only slightly above the thermal explosion limit. These long times can result in very long combustor lengths, thus if photochemical ignition is possible, then the ignition times may be substantially less resulting in shorter and lighter weight combustors. Experiments by Levy, Cerkanowicz, and McAlevy, III [4] demonstrated

that short photochemical ignition delay times are possible; they investigated flash photolysis of hydrogen-air and methane-air mixtures in the vacuum ultraviolet from 1350 to 1700 Angstroms. Rice [5] investigated the formation of a weak detonation wave by exposing hydrogen-chlorine and chlorine sensitized oxygen hydrogen mixtures to visible and near ultraviolet light. A shock tube was used to generate the gas flow and a Xenon flash lamp provided the radiation. Experimental measurements and theoretical calculations showed that the chemical reactions resulting from photochemical initiation are fast enough to form a weak detonation. However, to sustain the combustion of the system studied, very high power levels on the order of hundreds of kilowatts are necessary for the photon source.

The purpose of this dissertation was to generate in constant and varying area a weak detonation wave by radio frequency (R.F.) heating of a supersonic inert gas and by mass addition to a supersonic water stream. To establish the supersonic thermal wave, an R.F. coil is wrapped around an electrically non-conducting duct through which gas flows. The coil is connected to an R.F. power supply. The length of the coil will represent the wave region since the heating is accomplished by electrons and consequently will be quite rapid. Thus one could measure the flow properties of a supersonic flow through the duct and compare them to the equations for a weak detonation. Since heating by an R.F. coil restricts the major energy input to a region about one-half the distance from the wall to the center of the duct because of space charge effects, a variation of temperature with duct radius can be studied so that a good check can be made on the ideal quasi-one-dimensional equations which are based on

average properties across the duct radius. R.F. heating of a gas is relatively inefficient, only about 10% of the power generated can be transferred to the gas; hence, for an actual engine this would have to be greatly increased before R.F. heating can be considered as a practical form of energy in powerplants.

Oppenheim and Tearnen extended the hydraulic analogy theory to include the energy addition case for comparison of water and gas flows. In the basic analogy water behaves like a gas with a specific heat ratio (γ) equal to two and gas pressure ratios are represented by water height ratios squared. The energy addition analogy is qualitative and not quantitative. Oppenheim [6] and Tearnen [7] experimentally investigated the case of the strong detonation wave (hydraulic jump created by mass addition to the main stream flow) but did not experimentally check the weak detonation mode. In this dissertation the simulation of a weak detonation wave by mass addition to a supersonic water flow was attempted to determine if it would qualitatively predict the phenomena obtained in the gas flow tests. This effort would validate the use of the hydraulic analogy to obtain an insight into energy addition to a flowing gas for any velocity.

SECTION III

THEORETICAL ANALYSIS

Flow Equations

The quasi-one-dimensional theory for gas flow is based on average properties (with respect to radius, $\langle M \rangle = \int_0^R MRdR / \int_0^R RdR$) across the radius of an axisymmetric duct. From Shapiro [8], one may find the special conditions for energy addition based on constant area, constant Mach number, constant pressure, etc. However, for the general case of energy addition simultaneous with area variation, friction, and mass exchange, a different approach must be taken. For a comparison with experimental results which are based on energy exchange in varying area ducts, it is necessary to have a theory which includes these effects.

Two approaches were considered. A rigorous analysis retaining all terms of the fundamental equations is very tedious and entails great difficulties in working out a computer program. This first approach starts with the Navier Stokes equations and makes no simplifying assumptions. To solve the equations, initial profiles (along with radial derivatives) across the radius for pressure, temperature, and velocity are assumed, and all axial derivatives are written in finite difference notation. The energy input term is given as a function of radius and axial position. The finite difference terms are written based on one point in front of present location and up to four points behind it. This method allows one to solve for the ΔU, ΔT, etc. that are required

for going from the present location to the next one. The solution is obtained at each point across the radius by varying the pressure increment until an agreement is reached between the radial velocity component in the continuity equation and the radial velocity component in the radial momentum equation. Once this calculation is accomplished across the radius, the values of the properties are known and their first and second derivatives can be calculated by a SPLINE computer routine which fits a curve through a set of given data points. After the new derivatives are known, the process is repeated for the next axial increment. The difficulty of the above analysis lies in providing a realistic initial profile (particularly near the wall) for the axial and radial velocities. Too large an increment in velocity was usually calculated near the wall or a solution was not obtainable. When a solution was obtained across the radius, calculation of the second derivative of velocity with respect to radius resulted in values with alternating signs thus preventing continuation of the solution. Because of these difficulties, this effort has been discontinued until a better method for calculating second derivatives can be developed.

In a second approach the problem has been analyzed successfully by a procedure which is an extension of Shapiro's [8] method. Following Shapiro, the Navier Stokes equations are used for the case that the coefficient of viscosity is constant, contributions to the shear stress by $\partial u/\partial x$ is negligibly small, the flow is axisymmetric, average properties $(\overline{P})$ defined by $(\overline{P}) = \int_0^R (P)RdR / \int_0^R RdR$ are used, and a friction factor f is defined. For this case it can be shown that:

$$\frac{d\bar{\rho}}{\bar{\rho}} + \frac{d\bar{u}}{\bar{u}} + \frac{dA}{A} = \frac{d\dot{m}}{\dot{m}} \qquad \text{Continuity} \quad (1)$$

$$\bar{\rho}\bar{u}\frac{d\bar{u}}{dx} + \frac{d\bar{p}}{dx} + \frac{1}{2}\bar{\rho}\bar{u}^2\left[\frac{4f}{D} + \frac{2(1-y)}{\dot{m}}\cdot\frac{d\dot{m}}{dx}\right] = 0.0 \qquad \text{Momentum} \quad (2)$$

$$\frac{d\bar{T}^\circ}{\bar{T}^\circ} = \frac{d\bar{T}}{\bar{T}} + \frac{\frac{\gamma-1}{2}\bar{M}^2}{1+\frac{\gamma-1}{2}\bar{M}^2}\cdot\frac{d\bar{M}^2}{\bar{M}^2} \qquad \text{Energy} \quad (3)$$

$$\frac{d\bar{p}}{\bar{p}} = \frac{d\bar{\rho}}{\bar{\rho}} + \frac{d\bar{T}}{\bar{T}} \qquad \text{Equation of State} \quad (4)$$

D is the diameter of the duct and y is the injected mass flow velocity component parallel to the main stream velocity divided by the main stream velocity. Defining a conical flow area we can write:

$$A = \frac{\pi D^2}{4}\ ,\quad D = mx + D_1\ ,\quad \frac{dA}{A} = \frac{2\,dD}{D} = \frac{2m\,dx}{mx+D_1} \quad (5)$$

where $m = 2\tan\theta$ and θ is the divergence angle of the duct. In the following work, the average sign (-) will be dropped from the equations.

Multiplying the momentum equation (2) by dx and dividing by pressure p and using equation (1) we get:

$$\frac{\gamma M^2}{2}\frac{du^2}{u^2} + \frac{d\rho}{\rho} + \frac{dT}{T} + \frac{\gamma M^2}{2}\left[\frac{4f\,dx}{D} + 2(1-y)\cdot\frac{d\dot{m}}{\dot{m}}\right] = 0.0 \quad (6)$$

$$M^2 = \frac{u^2}{\gamma RT}\ ,\quad \frac{dM^2}{M^2} + \frac{dT}{T} = \frac{du^2}{u^2} \quad (7)$$

$$\therefore \quad \frac{du^2}{u^2} = \frac{dM^2}{M^2} + \frac{dT^\circ}{T^\circ} - \frac{\frac{\gamma-1}{2}M^2}{1+\frac{\gamma-1}{2}M^2} \cdot \frac{dM^2}{M^2} \tag{8}$$

To extend Shapiro's analysis, the following two assumptions are made:

$$\frac{T_2^\circ}{T_1^\circ} = \left[\frac{A_2}{A_1}\right]^N \quad ; \quad \frac{dT^\circ}{T^\circ} = N\frac{dA}{A} \tag{9}$$

$$\frac{\dot{m}_2}{\dot{m}_1} = \left[\frac{A_2}{A_1}\right]^n \quad ; \quad \frac{d\dot{m}}{\dot{m}} = n\frac{dA}{A} \tag{10}$$

These two assumptions will permit the analysis of a flow in which total temperature change, area change, and mass flow exchange can occur simultaneously.

Substituting equations (1), (3), (4), (8), (9), and (10) into (6) and rearranging results in:

$$\frac{(M^2-1)\cdot dM^2}{M^2(a+bM^2+cM^4)} = \frac{m\,dx}{mx+D_1} \tag{11}$$

where

$$a = 2(1-n) - N$$

$$b = \left[2(1-n) - N\right]\frac{\gamma-1}{2} - \gamma\left[\frac{\phi}{2m} + N\right]$$

$$c = \frac{\gamma(1-\gamma)}{2}\left[\frac{\phi}{2m} + N\right]$$

$$\frac{\phi}{2m} = \frac{4f}{2m} + 2(1-\gamma)n$$

To determine the proper integral to use for evaluating the integral of $\frac{-dM^2}{M^2(a+bM^2+cM^4)}$ on the left side of equation (11), it is necessary to examine the quantity $q = 4ac - b^2$, or:

$$q = -\left[\gamma^2\left(\frac{\phi}{2m} + N + 2n\right)^2 + 2\gamma\cdot(2-N-2n)\cdot\frac{\gamma-1}{2}\cdot\left(\frac{\phi}{2m} + N + 2n\right) + (2-M-2n)\,\frac{(\gamma-1)^2}{4}\right] \tag{12}$$

Taking the first derivative of q with respect to $\phi/2m$, and setting equal to zero gives:

$$\frac{\phi}{2m} = -\left[\frac{\gamma+1}{2\gamma}(N+2n) + \frac{\gamma-1}{\gamma}\right] \tag{13}$$

Also setting q = 0 and solving for $\phi/2m$, we get:

$$\frac{\phi}{2m} = -\left[\frac{\gamma+1}{2\gamma}(N+2n) + \frac{\gamma-1}{\gamma}\right] \tag{14}$$

Taking the second derivative of q with respect to $\phi/2m$, we get:

$$\frac{d^2q}{d(\phi/2m)^2} = -2\gamma^2 \tag{15}$$

Hence, since the function is concave downward and the maximum occurs at the same $\phi/2m$ value where q = 0, q is always $\leq$ zero. This condition determines the type of integral to use from the integral tables.

Now integrating both sides of equation (11) and combining terms, we finally arrive at:

$$\frac{A_2}{A_1} = \left[1 + \frac{Q}{C_p T_1^\circ}\right]^{1/N} = \left[\frac{T_2^\circ}{T_1^\circ}\right]^{1/N} =$$

$$\left[\frac{1 + \frac{\gamma-1}{2} M_2^2}{1 + \frac{\gamma-1}{2} M_1^2} \cdot \frac{2(1-N) - N - \gamma\left(\frac{\phi}{2m} + N\right) M_1^2}{2(1-N) - N - \gamma\left(\frac{\phi}{2m} + N\right) M_2^2}\right]^{\psi} \cdot$$

$$\left[\left(\frac{M_1}{M_2}\right)^4 \cdot \frac{a + bM_2^2 + cM_2^4}{a + bM_1^2 + cM_1^4}\right]^{1/2a} \cdot$$

$$\left[\left(\frac{2cM_2^2 + b - \sqrt{-g}}{2cM_1^2 + b - \sqrt{-g}} \cdot \frac{2cM_1^2 + b + \sqrt{-g}}{2cM_2^2 + b + \sqrt{-g}}\right)^{b/\sqrt{-g}}\right]^{1/2a} \tag{16}$$

where $\psi = \dfrac{2}{(\gamma+1)N + 2[\gamma(\phi/2m + 1) - (1-n)]}$

Equation (16) allows us to calculate the other properties for heat addition with simultaneous varying area, mass flow exchange, and friction by utilizing the equations:

$$\frac{\rho_2 V_2 A_2}{\rho_1 V_1 A_1} = \left[\frac{A_2}{A_1}\right]^n \tag{17}$$

$$T^\circ = T\left[1 + \frac{\gamma-1}{2} M^2\right] \tag{18}$$

which result in:

$$\frac{T_2}{T_1} = \left[\frac{A_2}{A_1}\right]^N \cdot \left[\frac{1 + \frac{\gamma-1}{2} M_1^2}{1 + \frac{\gamma-1}{2} M_2^2}\right] \tag{19}$$

$$\frac{P_2}{P_1} = \left[\frac{A_2}{A_1}\right]^{\frac{N+2(n-1)}{2}} \cdot \frac{M_1}{M_2} \cdot \left[\frac{1+\frac{\gamma-1}{2}M_1^2}{1+\frac{\gamma-1}{2}M_2^2}\right]^{1/2} \tag{20}$$

$$\frac{\rho_2}{\rho_1} = \left[\frac{A_2}{A_1}\right]^{\frac{-N+2(n-1)}{2}} \cdot \frac{M_1}{M_2} \cdot \left[\frac{1+\frac{\gamma-1}{2}M_2^2}{1+\frac{\gamma-1}{2}M_1^2}\right]^{1/2} \tag{21}$$

$$\frac{P_2^\circ}{P_1^\circ} = \left[\frac{A_2}{A_1}\right]^{\frac{N+2(n-1)}{2}} \cdot \frac{M_1}{M_2} \cdot \left[\frac{1+\frac{\gamma-1}{2}M_2^2}{1+\frac{\gamma-1}{2}M_1^2}\right]^{\left(\frac{\gamma+1}{2(\gamma-1)}\right)} \tag{22}$$

$$\frac{S_2 - S_1}{R} = \ln\left[\frac{M_2}{M_1}\left(\frac{A_2}{A_1}\right)^{\frac{N(\gamma+1)}{2(\gamma-1)}-n+1} \cdot \left(\frac{1+\frac{\gamma-1}{2}M_1^2}{1+\frac{\gamma-1}{2}M_2^2}\right)^{\frac{\gamma+1}{2(\gamma-1)}}\right] \tag{23}$$

With these equations [(16) through (23)], using n or N as variable parameters, and including friction by means of the friction factor f, one can analyze flows in axisymmetric ducts with area change, energy exchange, and variable mass flow. The assumptions (9) and (10) are reasonable since eight special cases satisfy this relation:

1. Zero energy exchange $N = n = 0.0$
2. Constant area duct $N \to \infty$ $n \to \infty$
3. Constant Mach number

$$N = \frac{2(1-n) - \gamma\left[\frac{f}{\tan\theta} + 2(1-\gamma)n\right]M_1^2}{\gamma M_1^2 + 1}$$

f → friction factor

θ → divergence angle

y → injection velocity/flow velocity

4. Constant total pressure

$$N = -\frac{f}{\tan\theta} - 2(1-y)n$$

5. Constant static pressure ($M \leq 0.5$)

$$N = 1 - n - \frac{f}{\tan\theta}$$

6. Constant density and Mach number

$$N = -\frac{\left(\frac{f}{\tan\theta} + 2(1-y)n\right)}{\left(2/\gamma M_1^2 + 1\right)}$$

7. Constant temperature and Mach number

$$N = 0.0$$

$$\frac{f}{\tan\theta} = (1-n)\frac{2}{\gamma M_1^2} - 2n(1-y)$$

8. Constant pressure and Mach number

$$N = -f/\tan\theta - 2(1-y)n$$

$$\frac{f}{\tan\theta} = \frac{2(1-n)}{\gamma M_1^2 + 1} + 2(1-y)\cdot n\left[1 - \frac{\gamma M_1^2}{\gamma M_1^2 + 1}\right]$$

The special case (6) (constant density and Mach number) will be demonstrated here. Starting with equation (6) we can write:

(24)

$$\frac{\gamma M^2}{2}\frac{dT^\circ}{T^\circ} + \frac{dT^\circ}{T^\circ} + \frac{\gamma M^2}{2}\left[\frac{4f}{2m} + 2(1-\gamma)n\right]\frac{dA}{A} \tag{25}$$

$$\frac{dT^\circ}{T^\circ} = N\frac{dA}{A} \tag{26}$$

$$N\left[\frac{\gamma M^2}{2} + 1\right] + \frac{\gamma M^2}{2}\left[\frac{4f}{2m} + 2(1-\gamma)n\right] = 0.0 \tag{27}$$

Therefore, for constant density and Mach number:

$$N = -\frac{\gamma M^2}{2}\left(\frac{4f}{2m} + 2(1-\gamma)n\right)\Big/\left(\frac{\gamma M^2}{2} + 1\right) \tag{28}$$

It should be mentioned that the constant total pressure condition (4) cannot be achieved if the energy exchange is dependent on friction by Reynolds analogy; and, condition (4) requires energy removal from the flow to counteract the effect of friction. Condition (4) does not hold for heat addition. Total temperature based on Reynolds analogy can be written:

$$\frac{dT^\circ}{T^\circ} = 2f\frac{dx}{D}\left(\frac{T_w}{T^\circ} - 1\right) \tag{29}$$

T_w - wall temperature

From special condition (4) for zero mass transfer, we can write the following:

$$\left[\frac{A_2}{A_1}\right]^{-f/\tan\theta} = \frac{T_2^\circ}{T_1^\circ} \tag{29a}$$

$$-\frac{f}{\tan\theta}\ln\left(\frac{A_2}{A_1}\right)=\ln\left(\frac{T_2^\circ}{T_1^\circ}\right);\quad -\frac{f}{\tan\theta}\frac{dA}{A}=\frac{dT^\circ}{T^\circ}$$

$$-\frac{f}{\tan\theta}\frac{4\tan\theta\,dx}{D}=\frac{dT^\circ}{T^\circ}$$

$$\therefore\quad \frac{dT^\circ}{T^\circ}=-4f\frac{dx}{D} \tag{30}$$

Equation (30) can also be directly obtained from the momentum equation (2) by the appropriate substitutions resulting in:

$$\frac{dP^\circ}{P^\circ}+\frac{\gamma M^2}{2}\frac{dT^\circ}{T^\circ}+\frac{\gamma M^2}{2}\cdot\frac{4f\,dx}{D}=0.0 \tag{2}$$

which for constant total pressure results in equation (30). Equation (30) is different from equation (29), thus the cooling of the flow must be achieved by an ideal process which tends to lower the gas temperature and not by heat transfer across the duct wall.

If LN (n) is zero, there is no friction, and $N \to \infty$, then equation (16) reduces to:

$$1+\frac{Q}{C_p T_1^\circ}=\left[\frac{1+\frac{\gamma-1}{2}M_2^2}{1+\frac{\gamma-1}{2}M_1^2}\cdot\frac{1+\gamma M_1^2}{1+\gamma M_2^2}\right]^{3/2}\cdot \left[\frac{1+\frac{3\gamma-1}{2}M_1^2+\frac{\gamma-1}{2}\gamma M_1^4}{1+\frac{3\gamma-1}{2}M_2^2+\frac{\gamma-1}{2}\gamma M_2^4}\right]^{1/2}\cdot\left[\frac{M_2}{M_1}\right]^2 \tag{31}$$

Now, if this is correct, then for a normal shock ($q/CpT_1^0 = 0.0$) the right-hand side of equation (31) reduces to 1.0. To check this result,

let $M_1 = 4$, the Mach number behind the shock $M_2 = 0.435$, and $\gamma = 1.4$. Substituting into equation (31) gives:

$$\left[1 + \frac{Q}{C_p T_1^\circ}\right] = (0.457)^{1.5} \cdot (0.0118) \cdot (75)^{1/2} \tag{32}$$

$$\left[1 + \frac{Q}{C_p T_1^\circ}\right] = (9.8) \cdot (0.0118) \cdot (8.66) = 1.0 \tag{33}$$

Hence, we have demonstrated that equation (16) is correct and equation (31) holds for constant area and no friction.

There are probably some values of N and n and M_1 for which the conditions of constant pressure, constant temperature, or constant density are approximated; however, it will be more convenient to start with the basic equations to evaluate these conditions retaining only the expression $\dot{m}_2/\dot{m}_1 = \left[A_2/A_1\right]^n$. Below, the necessary equations for calculating the constant conditions mentioned above are given.

Constant Pressure

$$\ln \frac{A_2}{A_1} = \ln\left[\frac{M_1}{M_2}\right] \cdot \frac{2}{1 - n + \phi/4m} \tag{34}$$

$$\frac{T_2}{T_1} = \left[\frac{M_1}{M_2}\right]^{\left(\frac{2(1-n-\phi/4m)}{(1-n+\phi/4m)}\right)} \tag{35}$$

Constant Temperature

For no friction

$$\frac{A_2}{A_1} = \left[\frac{M_1}{M_2}\, e^{\left(\frac{\gamma M_1^2}{2}\left\{\left(\frac{M_2}{M_1}\right)^2 - 1\right\}\right)}\right]^{\frac{1}{1-n}} \tag{36}$$

$$\frac{P_2}{P_1} = \frac{M_1}{M_2}\left(\frac{A_2}{A_1}\right)^{(n-1)} \tag{37}$$

For friction

$$\frac{A_2}{A_1} = \left(\frac{M_1}{M_2}\right)^{\frac{1}{(1-n)}} \cdot \left[\frac{1-\left(n+\frac{\phi}{2m}\gamma\frac{M_2^2}{2}\right)}{1-\left(n+\frac{\phi}{2m}\gamma\frac{M_1^2}{2}\right)}\right]^{\left(\frac{\phi-4m(1-n)}{2\phi(1-n)}\right)} \tag{38}$$

Constant Density

$$\frac{A_2}{A_1} = \left[\frac{M_2}{M_1}\sqrt{\frac{\frac{\gamma}{2}\left(1+\frac{\phi}{4m(n-1)}\right)M_1^2+1}{\frac{\gamma}{2}\left(1+\frac{\phi}{4m(n-1)}\right)M_2^2+1}}\right]^{\frac{1}{1-n}} \tag{39}$$

$$\frac{T_2}{T_1} = \frac{\frac{\gamma}{2}\left(1+\frac{\phi}{4m(n-1)}\right)M_1^2+1}{\gamma/2\left(1+\frac{\phi}{4m(n-1)}\right)M_2^2+1} \tag{40}$$

Now a few special conditions that can occur in equation (16) will be examined. Consider the exponent

$$\psi = \frac{2}{(\gamma+1)N + 2\left[\gamma(1+\phi/2m)-1+n\right]} \tag{41}$$

and the expression

$$\left[\frac{1+\frac{\gamma-1}{2}M_2^2}{1+\frac{\gamma-1}{2}M_1^2}\right]\cdot\left[\frac{2(1-n)-N-\gamma(\phi/2m+N)M_1^2}{2(1-n)-N-\gamma(\phi/2m+N)M_2^2}\right]^{\psi} = \eta^{\psi} \tag{42}$$

When the denominator of ψ is 0, then $\psi \to \infty$ and

$$N = -2\left[\gamma\left(1+\frac{\phi}{2m}\right)-(1-n)\right]\Big/(\gamma+1) \tag{43}$$

also

$$\frac{A_2}{A_1} \to \infty \qquad \eta > 1 \tag{44}$$

$$\frac{A_2}{A_1} \rightarrow \text{finite when } \eta = 1 \tag{45}$$

$$\frac{A_2}{A_1} \rightarrow 0 \text{ when } \eta < 1 \tag{46}$$

Writing $\eta \gtreqless 1$ and solving for $\phi/2m$, it is found that:

$$\frac{\phi}{2m} \gtreqless -\frac{\gamma+1}{2\gamma}\cdot N + \frac{1-n}{\gamma} - (1-n) \tag{47}$$

also, from (43) we can write:

$$\frac{\phi}{2m} \gtreqless -\frac{\gamma+1}{2\gamma}\cdot N + \frac{1-n}{\gamma} - 1 \tag{48}$$

The last two equations are equal for n = 0; hence, when $\psi \rightarrow \infty$ the equation then reduces to $\eta^{\psi} = (1)^{\infty} = 1$ and a solution exists to equation (16). Next, if the terms in equation (16) of $2(1-n)-N-\gamma M_2^2\left(\frac{\phi}{2m}+N\right)$, $a+bM_2^2+cM_2^4$ and $2cM_2^2+b+\sqrt{-q}$ are set equal to zero, it is found that:

$$M_2^2 = \frac{2(1-n)-N}{\gamma(\phi/2m+N)} \tag{49}$$

for each term and likewise for the corresponding M_1 terms:

$$M_1^2 = \frac{2(1-n)-N}{\gamma(\phi/2m+N)} \tag{50}$$

For the constant Mach number case $M_2 = M_1$; hence, solving for N one arrives at:

$$N = \frac{2(1-n)-\gamma M^2\left(\frac{f}{\tan\theta}+2(1-\gamma)n\right)}{\gamma M^2+1} \tag{51}$$

which is the third special case listed earlier. If N = 0 = n, equation (51) gives $\tan\theta = \gamma f M^2/2$, which is the case of constant Mach number for friction as presented in Shapiro, Vol. I [18]. From the above it is seen that for a solution to exist for constant M then:

$$\frac{2(1-n)-N}{\gamma(\phi/2m+N)} \geq 0.0 \tag{52}$$

In equation (16) another term that needs to be examined is the exponent $1/2a = 1/(2\,[2\,(1-n) - N])$ when the denominator equals zero; $2\,(1-n) - N = 0$ or $N = 2\,(1-n)$. When a is zero, $b/\sqrt{-q} = 1$ or $b = -\gamma\,(\phi/2m + N)$, $c = (\gamma-1)/2\,b$, and equation (16) reduces to

$$\frac{A_2}{A_1} = \left[\frac{M_1^2}{M_2^2} \cdot \frac{M_2^2 + \frac{\gamma-1}{2}M_2^4}{M_1^2 + \frac{\gamma-1}{2}M_1^2} \cdot \frac{\frac{\gamma-1}{2}M_1^2 + 1}{\frac{\gamma-1}{2}M_2^2 + 1}\right]^{1/0.0} \cdot \left[\frac{1 + \frac{\gamma-1}{2}M_2^2}{1 + \frac{\gamma-1}{2}M_1^2} \cdot \frac{M_1^2}{M_2^2}\right]^{\psi} \tag{53}$$

or

$$\frac{A_2}{A_1} = (1)^{\infty} \cdot \frac{1 + \frac{\gamma-1}{2}M_2^2}{1 + \frac{\gamma-1}{2}M_1^2} \cdot \frac{M_1^2}{M_2^2} \tag{54}$$

$$\frac{A_2}{A_1} = \left[\frac{1 + \frac{\gamma-1}{2}M_2^2}{1 + \frac{\gamma-1}{2}M_1^2}\right] \cdot \left[\frac{M_1}{M_2}\right]^2 \qquad (\text{for } a = 2\,(1-n) - N = 0.0) \tag{55}$$

Hence, a solution exists for this condition.

Equation (16) has been discussed and analyzed in some detail so it is obvious that a large range of flow conditions can be investigated with it. Equation (16) is used for comparing theory with the

experimental results in Tables 2-10. Some examples of flow utilizing equation (16) are shown in Figures (2)-(9). These figures represent flow with area change, mass change, and total temperature change occurring simultaneously. For LN (or n) equal to 1000, this represents the constant area case. Figures (10)-(14) represent area change (decreasing) simultaneous with total temperature change with no friction. For N equal 1000, the area ratio equals one. The fact that equation (16) reduces to the constant area for LN (n) or $N \to \infty$ can be checked by choosing values off the above figures and comparing them against the constant area case in Shapiro [8]. The figures were obtained by a computer program which was written to analyze equations (16) through (21).

As an example of how to use the curves, assume you have a duct with an area ratio of $A_2/A_1 = 2.0$, a mass addition ratio of 1.6, and the total temperature ratio proportional to $(A_2/A_1)^{-0.5}$, while $M_1 = 4.0$. From Figure (2), this corresponds to n or LN = 0.7, which is one of the parametric curves based on various n values; $\dot{m}_2/\dot{m}_1 = (A_2/A_1)^n$. From Figures (3) and (4) it is found that $M_2 = 1.5$. Figures (5)-(9) then give the following values: $T_2^o/T_1^o = 0.7$, $T_2/T_1 = 2.1$, $P_2/P_1 = 3.75$, $P_2^o/P_1^o = 0.075$, and $V_2/V_1 = 0.54$. If one is interested in an initial Mach number other than $M_1 = 4.0$, then it is necessary to take the ratio of the y axis values for the desired initial and final Mach numbers.

NOTATION FOR FIGURES (2) THROUGH (14)

G → γ

M1 → M_1, P1 → P_1, etc.

LN → n

$\dot{M}1$ → $\dot{m}_1$ mass flow rate

PH → friction parameter ($f/\tan\theta$)

N = 0.00 → constant total temperature

N = 1000 → constant area

n = LN = 1000 → constant area

n = LN = 0.0 → 0.0 mass flow

Mass flow variation assumed to occur by parallel injection or removal of mass.

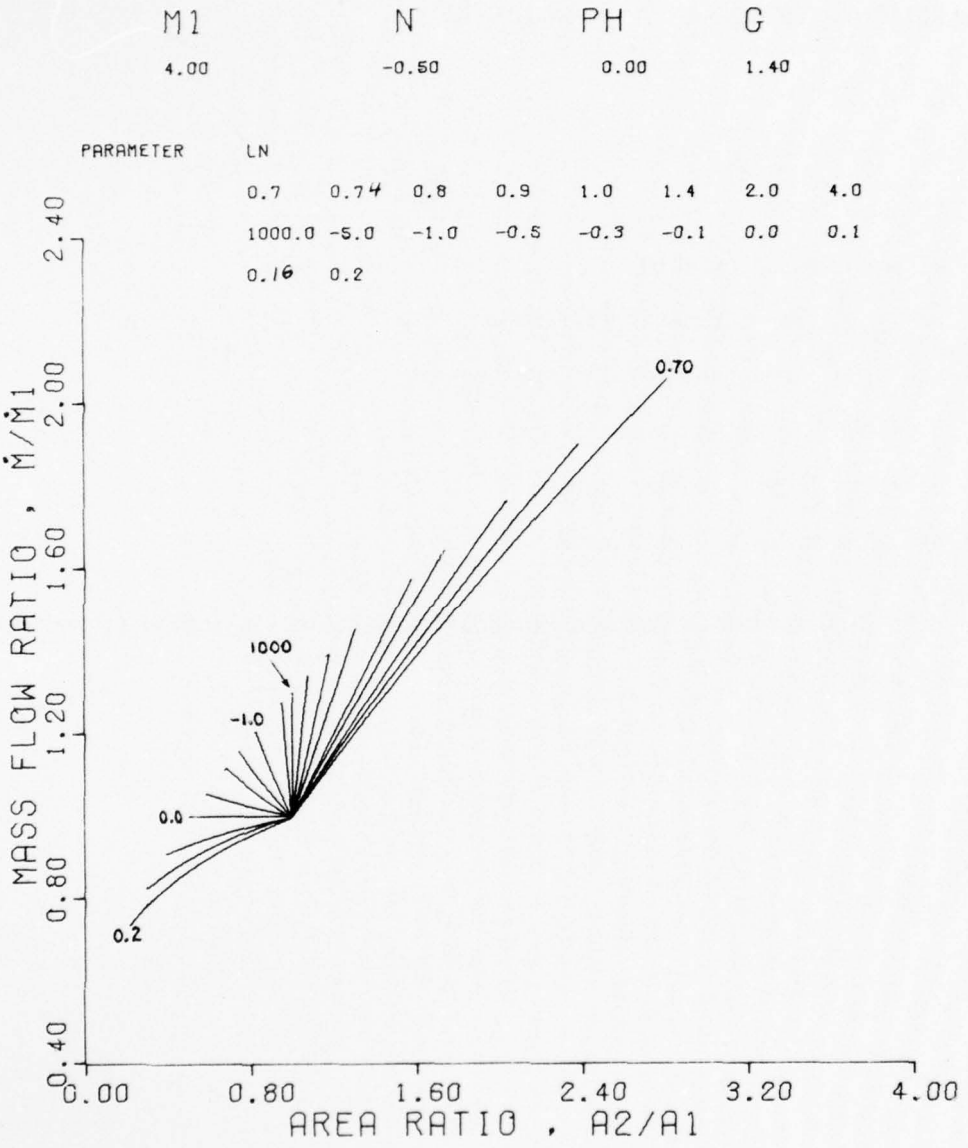

FIGURE 2 . MASS FLOW RATIO VS. AREA RATIO

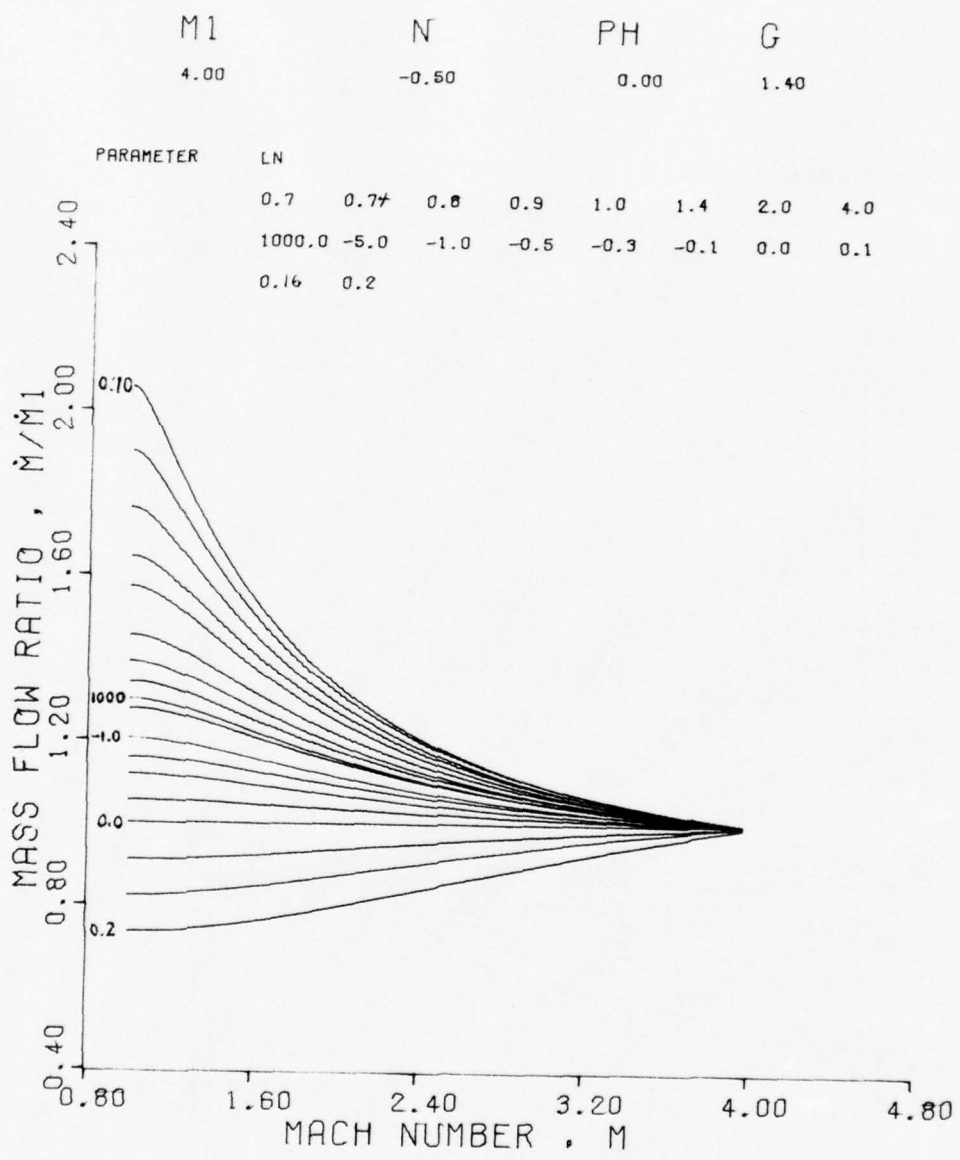

FIGURE 3 . MASS FLOW RATIO VS. MACH NUMBER

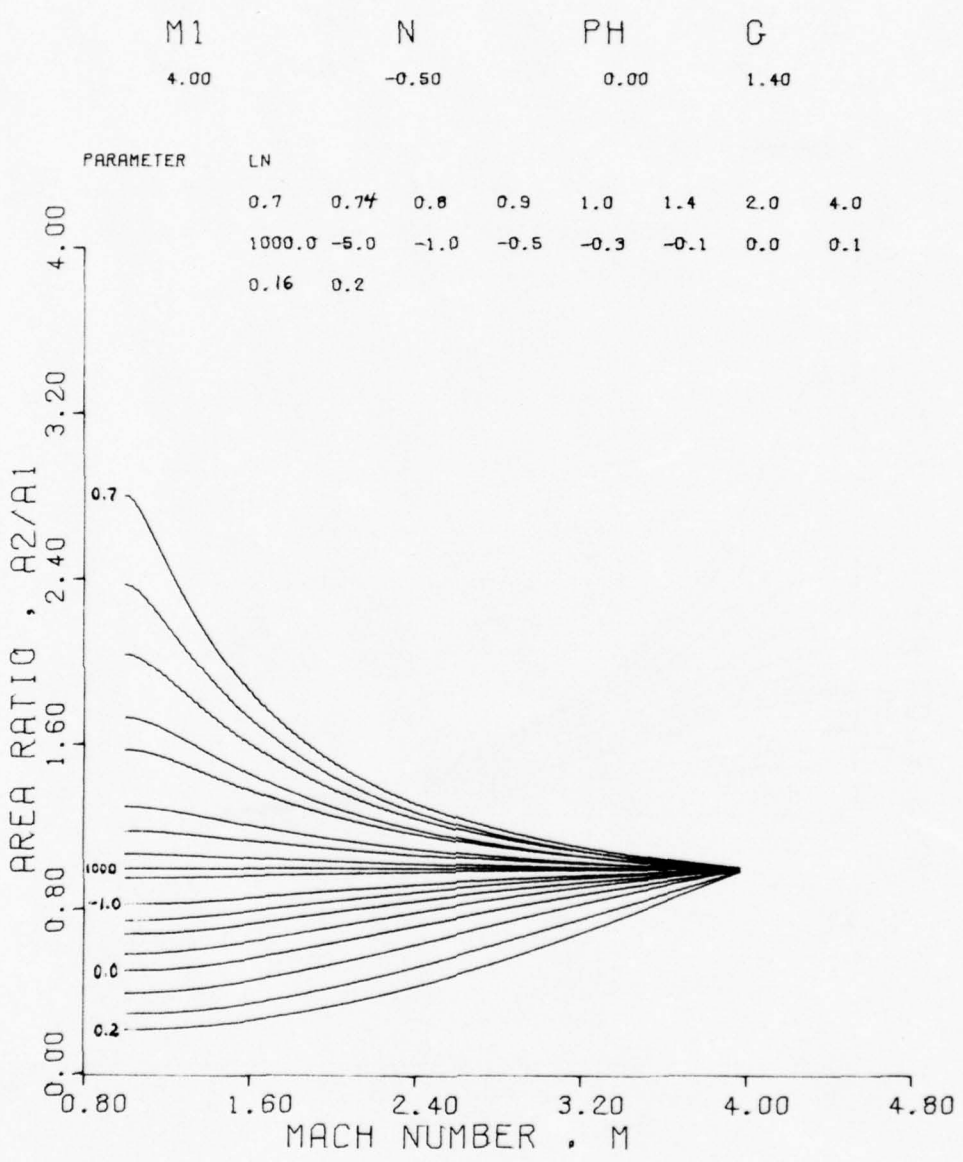

FIGURE 4 . AREA RATIO
MACH NUMBER

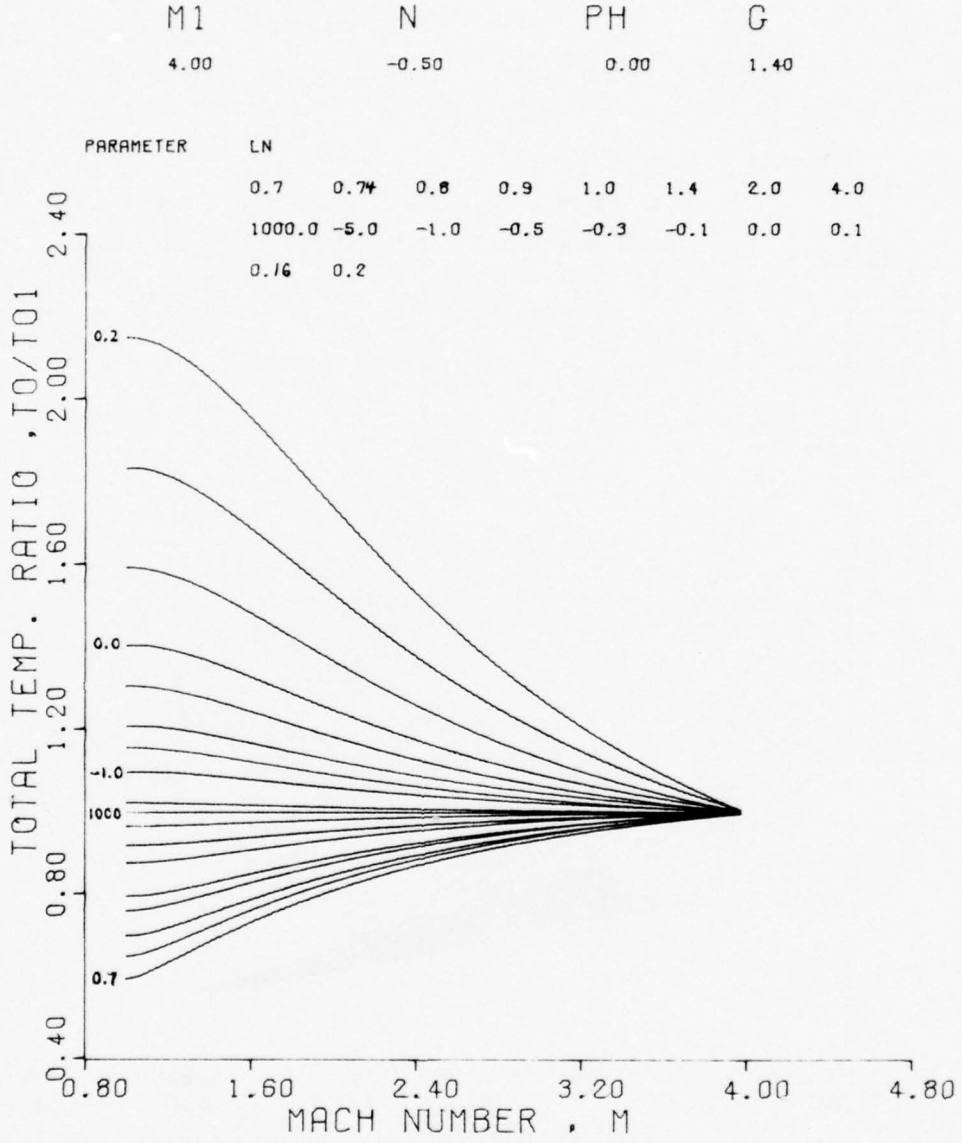

FIGURE 5 . TOTAL TEMPERATURE RATIO VS. MACH NUMBER

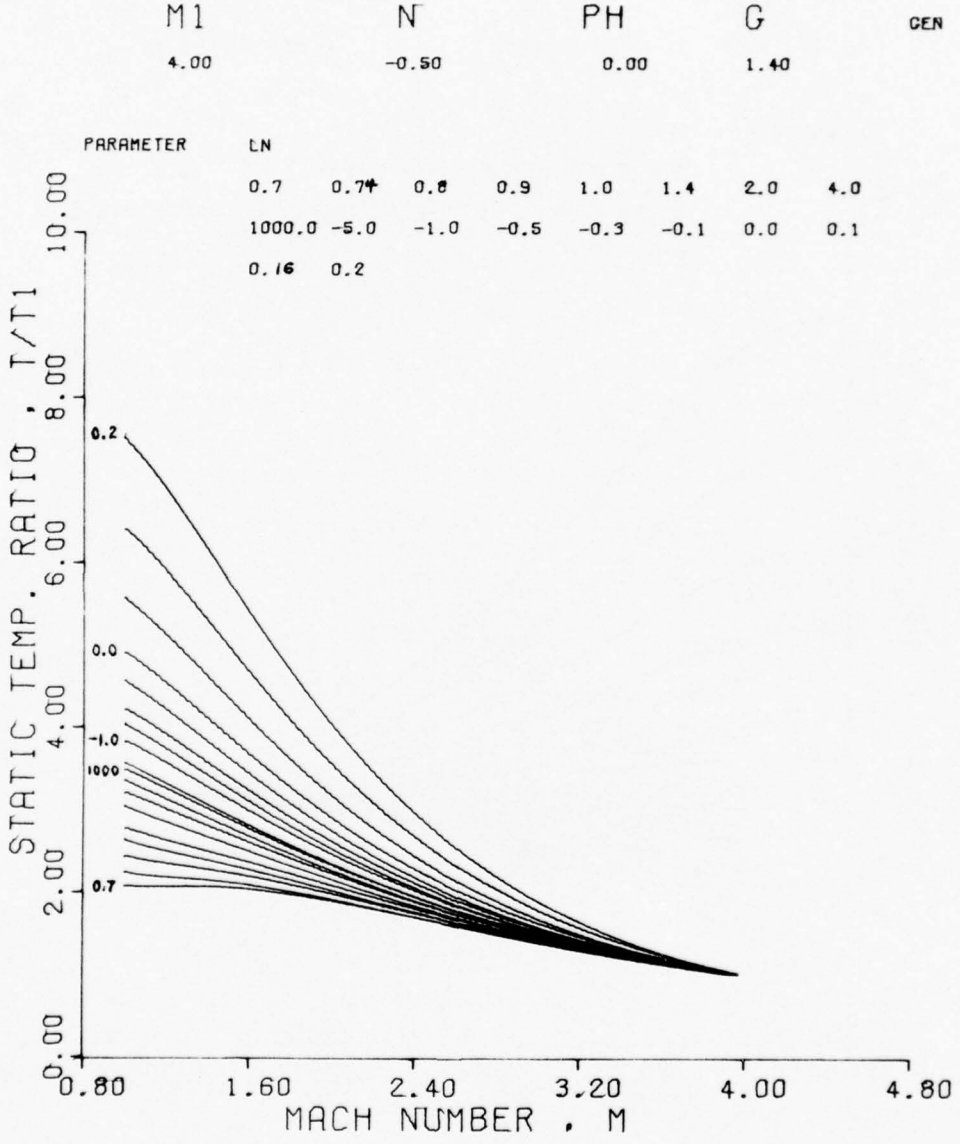

FIGURE 6 . STATIC TEMPERATURE RATIO VS. MACH NUMBER

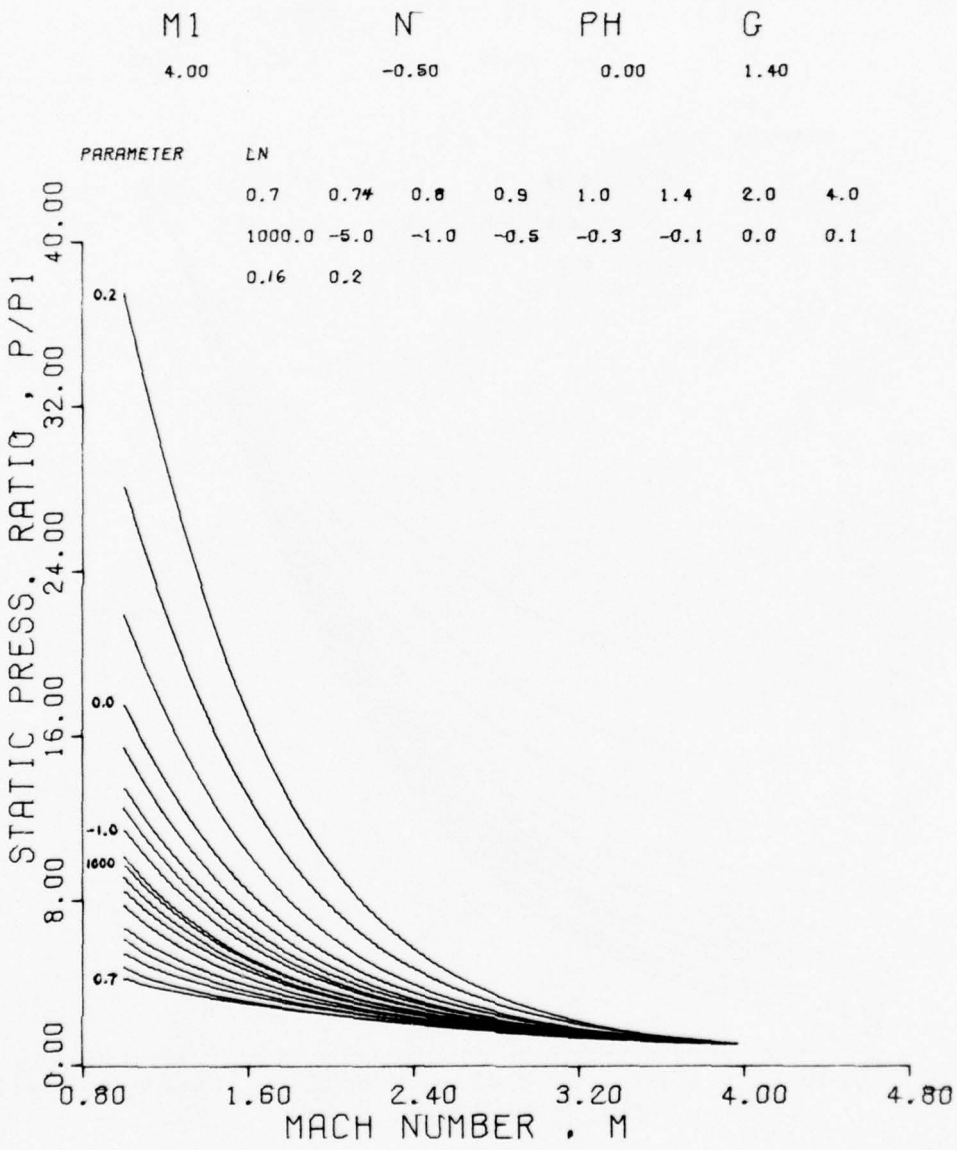

FIGURE 7 . STATIC PRESSURE RATIO VS. MACH NUMBER

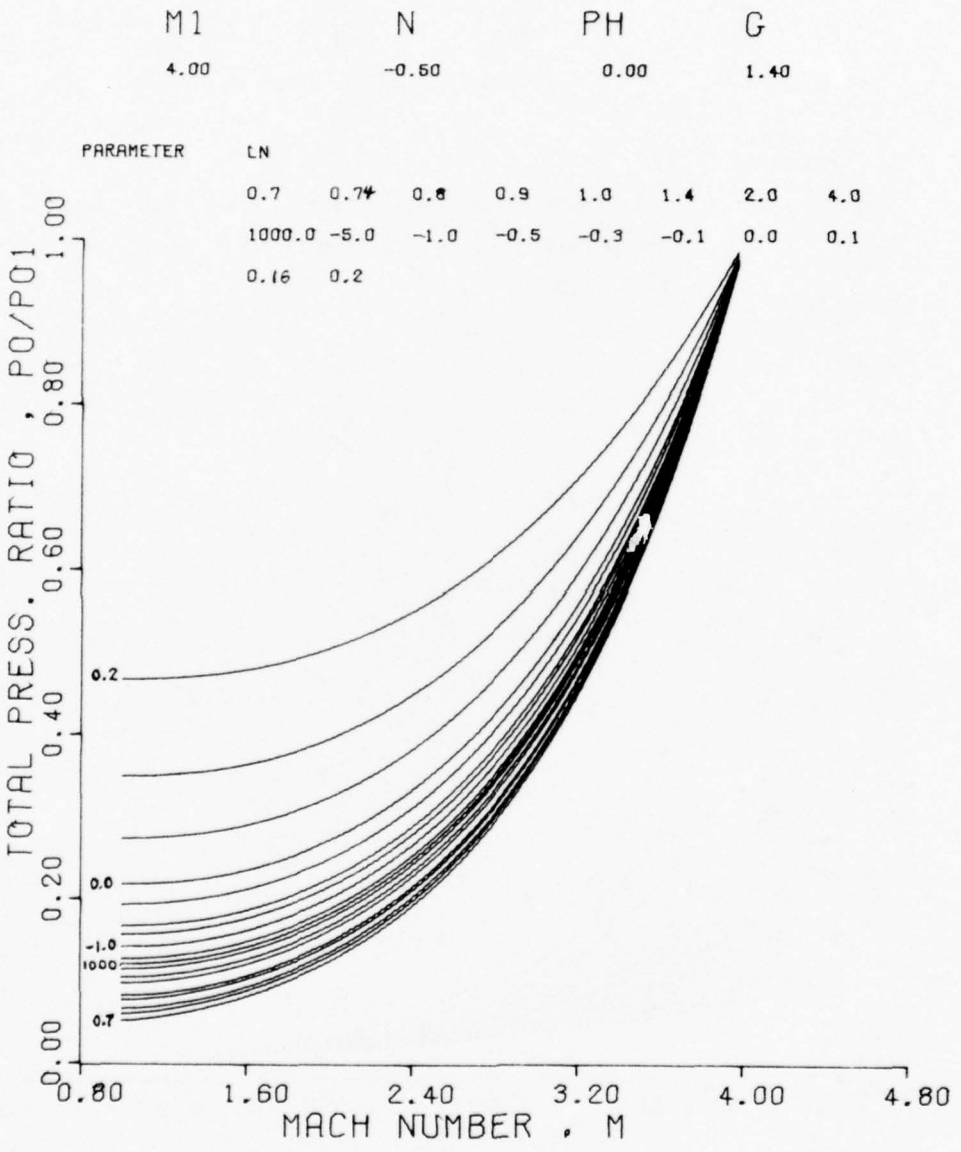

FIGURE 8 . TOTAL PRESSURE RATIO VS. MACH NUMBER

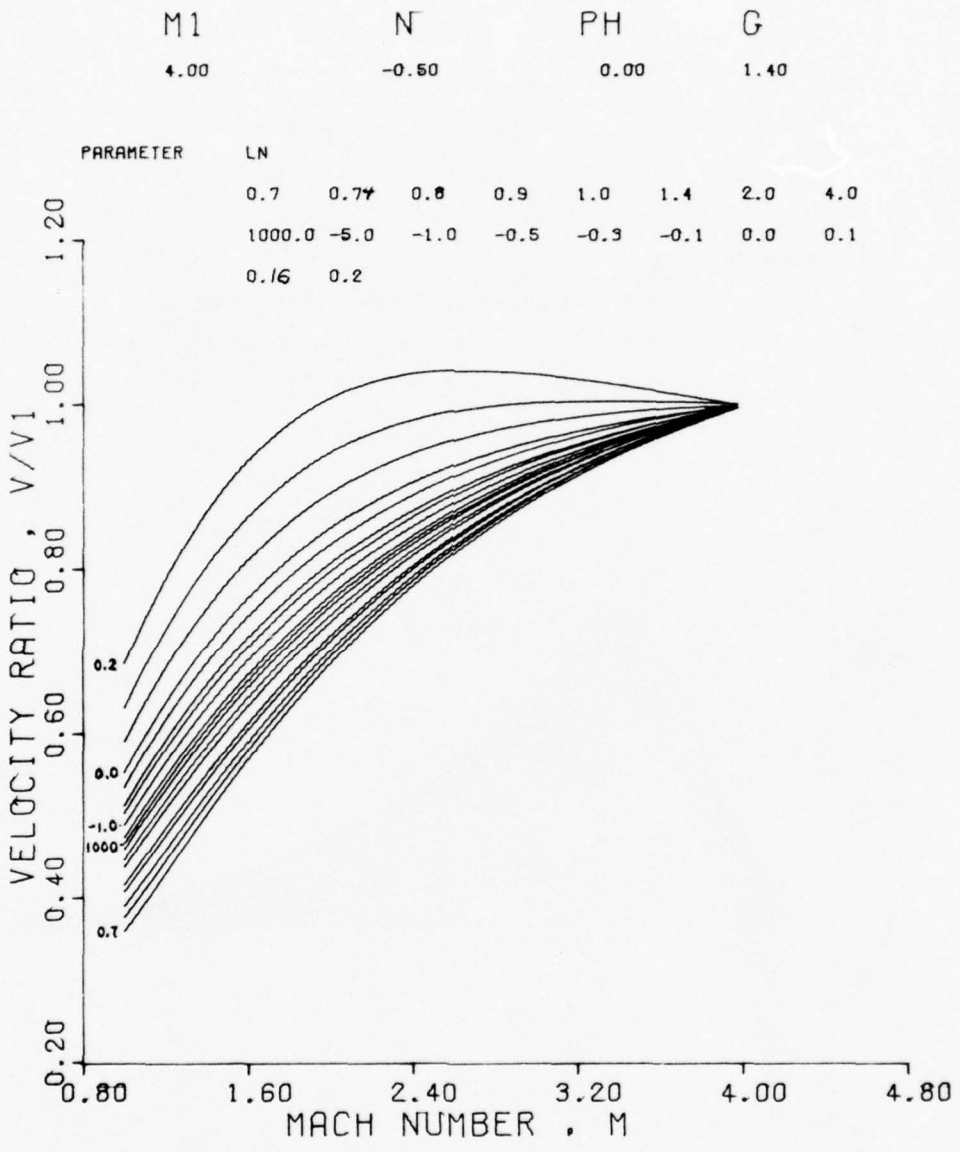

FIGURE 9 . VELOCITY RATIO VS. MACH NUMBER

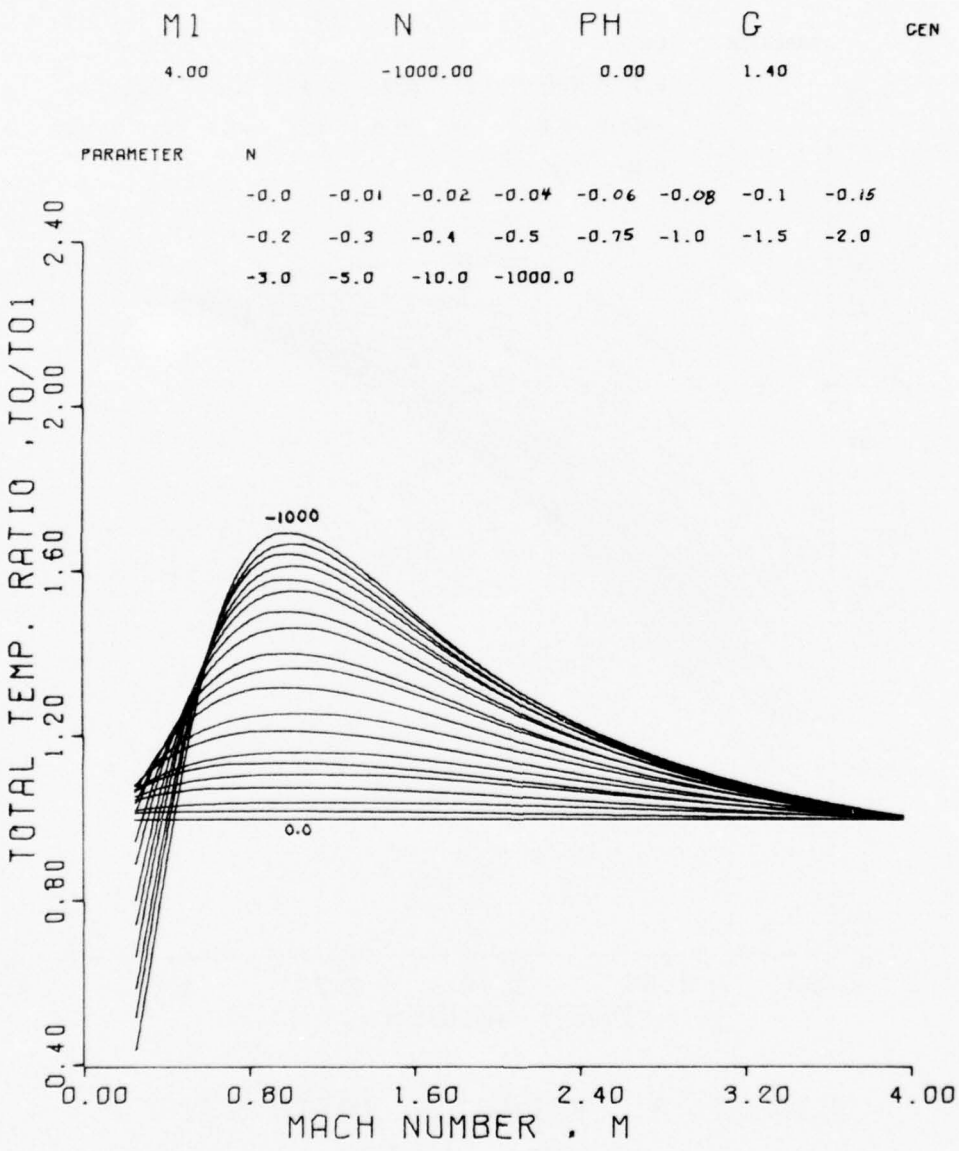

FIGURE 10 . TOTAL TEMPERATURE RATIO VS. MACH NUMBER

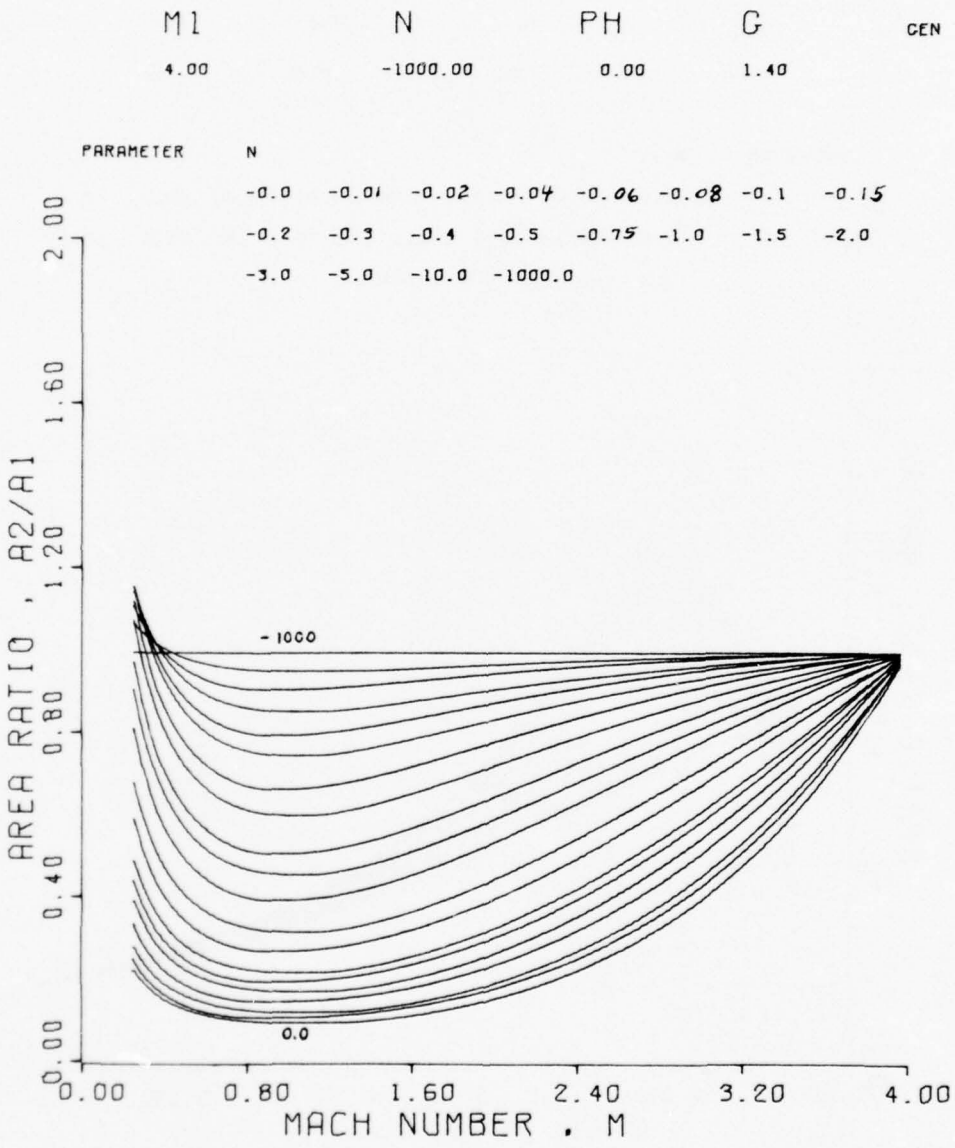

FIGURE 11 . AREA RATIO
MACH NUMBER

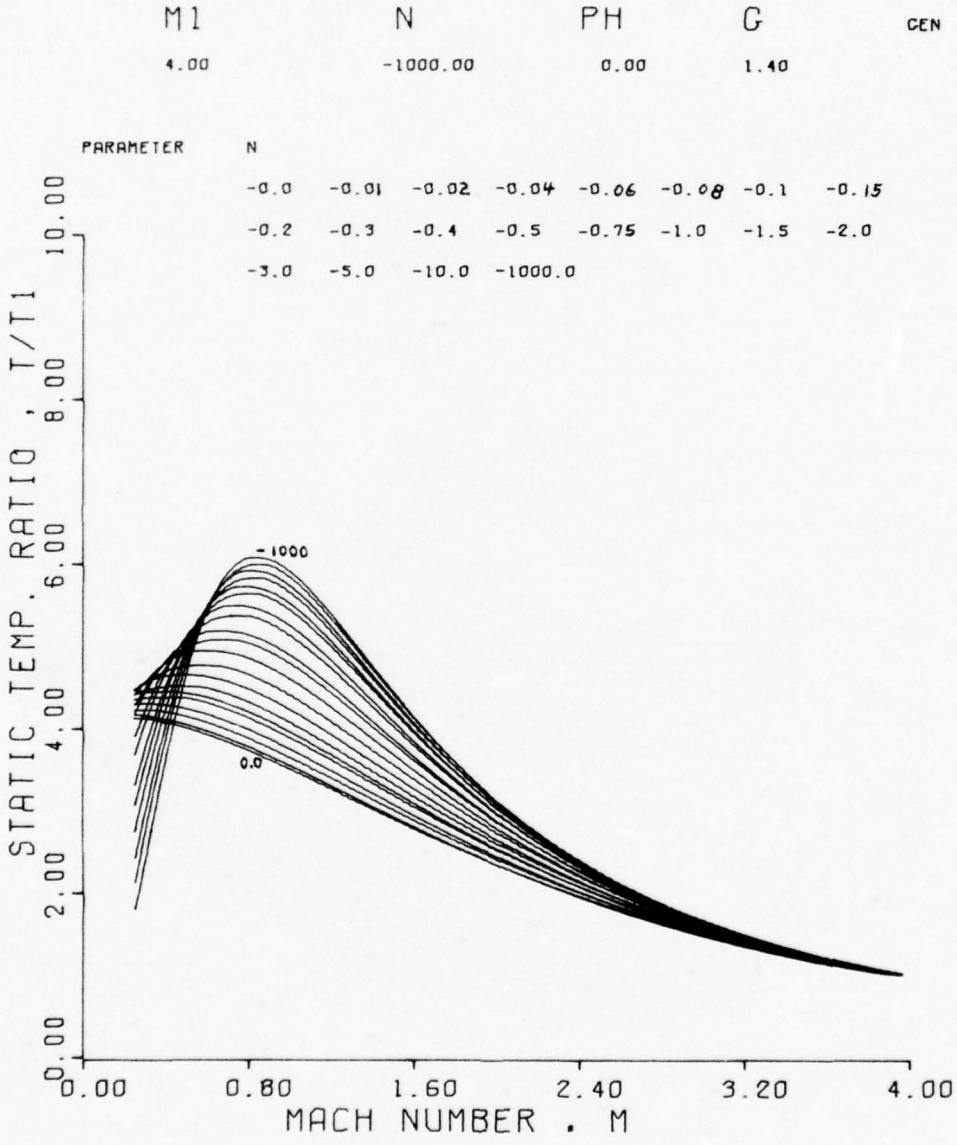

FIGURE 12 . STATIC TEMPERATURE RATIO VS. MACH NUMBER

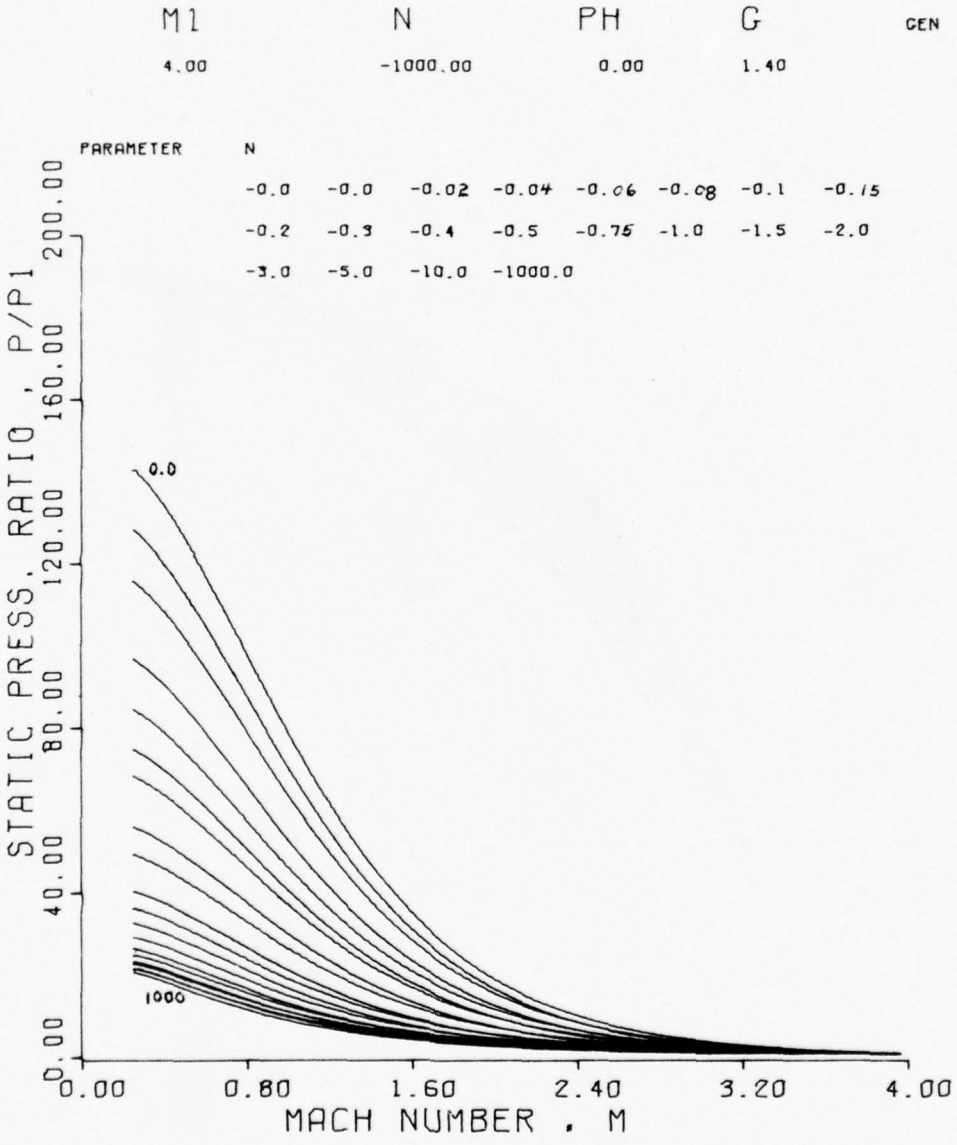

FIGURE 13 . STATIC PRESSURE RATIO VS. MACH NUMBER

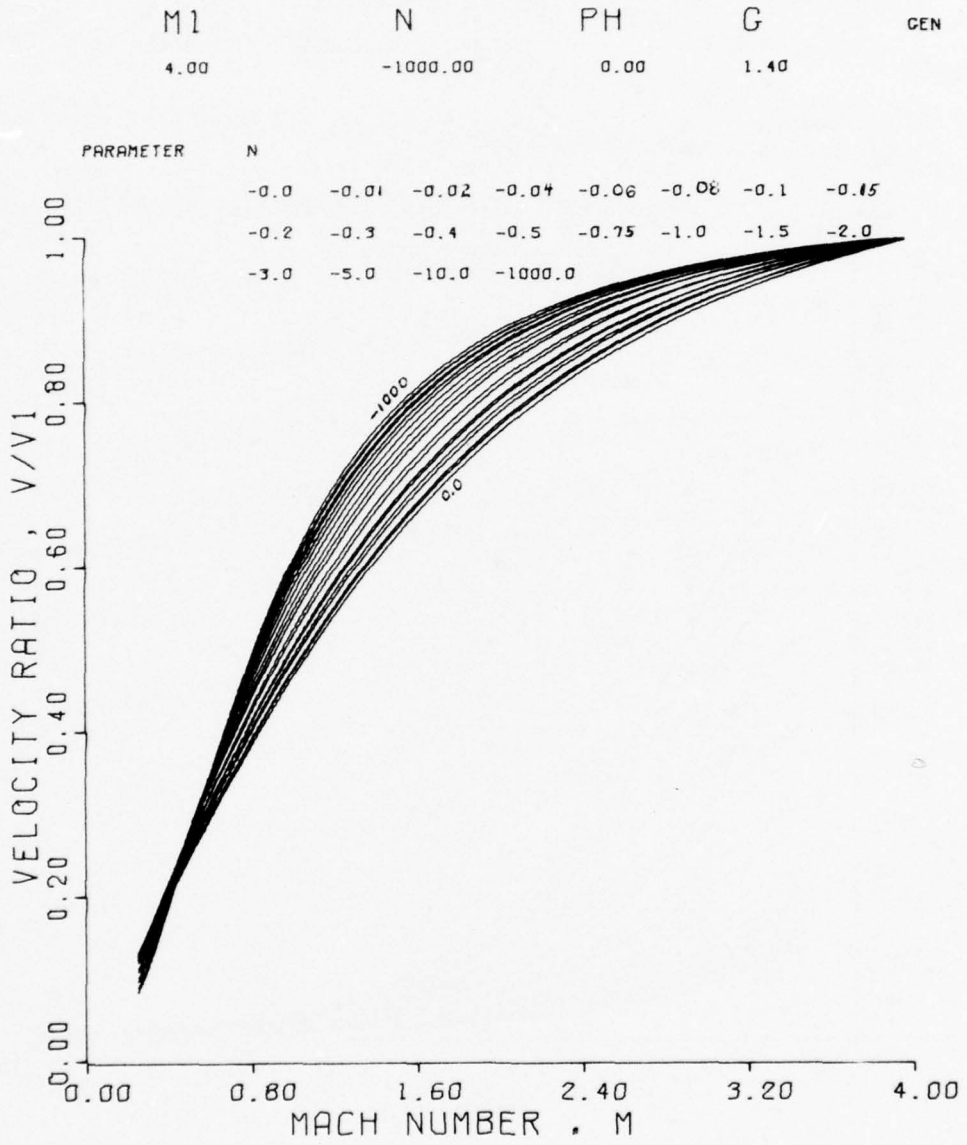

FIGURE 14 . VELOCITY RATIO VS. MACH NUMBER

Water Table Theory

It was noted in the introduction that there exists an analogy between gas flow and water flow, both subsonic and supersonic, which makes it possible to study aerodynamic problems on a water table. The analogy will now be presented in a mathematical form. See Ref. [6] and Ref. [7], which discuss the strong detonation wave analogy.

For steady-state water flow in a constant area channel we can write: (h = water depth; w = channel width) (mass injection normal to the flow)

$$\dot{m}v + g\rho W\frac{h^2}{2} = \dot{m}_1 v_1 + g\rho W\frac{h_1^2}{2} \tag{56}$$

$$\frac{\dot{m}v}{\rho W} + g\frac{h^2}{2} = \frac{\dot{m}_1 v_1}{\rho W} + g\frac{h_1^2}{2} \tag{57}$$

$$q = \frac{\dot{m}}{\rho W} = vh \tag{58}$$

$$\therefore\ v^2 h + g\frac{h^2}{2} = v_1^2 h_1 + g\frac{h_1^2}{2}$$

$$\frac{q^2}{h} + g\frac{h^2}{2} = \frac{q_1^2}{h_1} + g\frac{h_1^2}{2}$$

$$\frac{\lambda^2 q_1^2}{h} + g\frac{h^2}{2} = \frac{q_1^2}{h_1} + g\frac{h_1^2}{2} \tag{59}$$

where $\lambda = \frac{q_2}{q_1} = 1 + \frac{q_s}{q_1}$

q_s = injected mass

For gas flow we can write:

$$P + \rho V^2 = P_1 + \rho_1 V_1^2 \tag{60}$$

By comparing (59) and (60), we see an analogy: $gh^2/2 \rightarrow p$, $\lambda^2/h \rightarrow v$ (specific volume). Pressure is proportional to the water depth squared. Let $gh^2/2 = y$ be equivalent to pressure. Let $\lambda^2/h = x$ be equivalent to specific volume. Thus, equation (59) becomes:

$$x\, q_1^2 + y = x_1\, q_1^2 + y_1 \tag{61}$$

or $$q_1^2 = \left[\frac{q}{\lambda}\right]^2 = \left[\frac{y_1}{x_1}\right]\left[\frac{1 - y/y_1}{x/x_1 - 1}\right]$$

which is the Rayleigh Line analogy. The slope of the Rayleigh Line is $\tan\alpha = dy/dx = q_1^2 = -h_1^2 V_1^2$, or $\sqrt{\tan\alpha} = h_1 V_1$, which is similar to the gas case where $\sqrt{\tan\alpha} = \gamma M_1$.

Defining F as the ratio of velocity to gravity wave speed, we have:

$$F = \frac{V}{c} = \frac{q/h}{\sqrt{gh}} = \frac{q}{\lambda}\sqrt{\frac{x}{2y}} \tag{62}$$

and for a gas

$$M = \frac{V}{c} = \frac{\frac{\dot{m}}{A}\cdot\frac{1}{\rho}}{\sqrt{\gamma RT}} = \frac{\dot{m}}{A}\sqrt{\frac{1}{\gamma P \rho}} \tag{63}$$

Thus, by analogy $\dot{m}/A \rightarrow q/\lambda$ and $\gamma \rightarrow 2$.

It is apparent that water flow is analogous to a gas flow having a ratio of specific heats equal to 2. The Rayleigh analog can also be written:

$$\frac{1 - Y/Y_1}{x/x_1 - 1} = \frac{q_1^2}{y_1/x_1} = 2F_1^2 \tag{64}$$

and the gas case as

$$\frac{1 - P/P_1}{\rho_1/\rho - 1} = \gamma M_1^2 \tag{65}$$

From the definition of entropy

$$dS = C_v \frac{dT}{T} + R \frac{dv}{v}$$

$$\frac{\Delta S}{C_v} = \ln \frac{T_2}{T_1} + \ln \left(\frac{v_2}{v_1}\right)^{(\gamma-1)}$$

$$\frac{P_2}{P_1} \left[\frac{v_2}{v_1}\right]^{\gamma} = e^{\Delta S/C_v} \tag{66}$$

we can write for a gas that:

$$P v^{\gamma} = P_1 v_1^{\gamma} e^{\Delta S/C_v} \tag{67}$$

Thus to get an analogy for water, we can calculate:

$$y x^2 \equiv P v^{\gamma}$$

$$y x^2 = \frac{g}{2}\left[1 + \frac{q_s}{q_1}\right]^4 = \frac{g}{2}\left[1 + q_s \frac{x_1 - x}{y - y_1}\right]^4 \tag{68}$$

For the initial point $y_1 x_1^2 = g/2$; hence, we can write the Hugoniot analog as:

$$\frac{y}{y_1}\cdot\left[\frac{x}{x_1}\right]^2 = \left[1+\frac{q_s}{2y_1/x_1}\cdot\sqrt{\frac{1-x/x_1}{y/y_1-1}}\right]^4 \tag{69}$$

or

$$\frac{x}{x_1} = \left[\frac{(y/y_1)^{1/4}\cdot(y/y_1-1)}{\sqrt{y/y_1}\cdot(y/y_1-1)+2\epsilon^2}\right]\cdot$$

$$\left[1\pm\sqrt{1-\frac{(y/y_1-1-2\epsilon^2)(\sqrt{y/y_1}\cdot(y/y_1-1)+2\epsilon^2)}{\sqrt{y/y_1}\,(y/y_1-1)^2}}\right]^2 \tag{70}$$

where $\epsilon = q_s/\sqrt{gh_1^3}$

This Hugoniot curve for mass addition differs from the gas heat addition case since it passes through the point $y/y_1 = x/x_1 = 1.0$ and the gas case doesn't. The above analysis shows that an analog exists between mass addition to a water flow and heat addition to a gas flow. Although one cannot get a quantitative analysis for the gas flow from the water table, it is possible to gain a qualitative insight of what to expect in a similar gas flow situation. The nozzles fabricated for the water table were based on a sharp-edged throat and a gamma of 2.0 utilizing the two-dimensional approach outlined in Shapiro, Vol. I [8].

Electric Probe Theory

To analyze the results of the R.F. energy addition experiments, it is necessary to make total temperature measurements across the duct exit with a total temperature probe. However, since there is ionization of the gas, it is necessary to account for the energy released in the probe by electron recombination. An electric double probe was used to determine the ionization level so that a correction could be made to the

measured total temperature in order to account for electron-ion recombination and the electron temperature. The probe theory will now be discussed in some detail.

The original single probe theory as developed by Langmuir [9] applied to plasmas (ionized gases) where the mean free path of the particles was much larger than the radius of the probe. According to this technique, a voltage is applied from the probe to one of the discharge electrodes and the resulting current is measured as the voltage sweeps from negative to positive. Langmuir showed how the electron temperature can be determined from the slope of the electron current vs. voltage curve and that the electron density is derived from the current magnitude and electron temperature. See Figure (15) for a sketch of the probe characteristic. The negative voltage part of the curve is the ion collection part of the characteristic; this is the part of the curve that is relevant to the double probe theory.

Johnson and Malter [10] developed a theory for the use of a double probe for measuring electron temperature. They pointed out that the single probe method (SPM) is valid only if the cathode plasma potential, electron temperature, and random electron current do not change with the cathode probe potential. However, as the electron current (i_e) increases, one often observes changes in the discharge patterns, especially if i_e is an appreciable fraction of the main discharge current. The probe is then disturbing the very quantities it is intended to determine. As can be shown for the double probe method (DPM), the total current to the probe can never exceed the positive ion current to them; and, since this current is hundreds of times smaller than the electron current for the SPM,

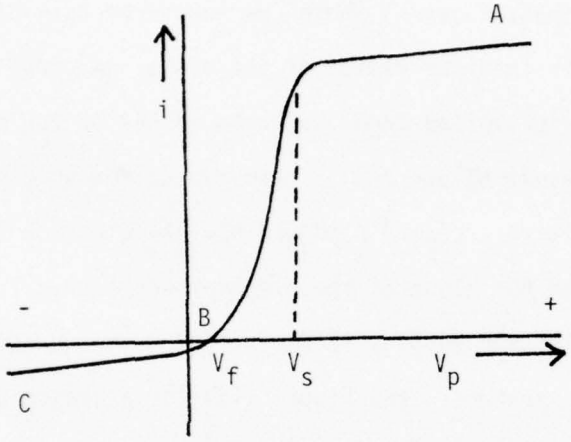

V_p - Probe Potential w.r.t. Arbitrary Reference Point

V_f - Floating Potential, Electron and Ion Currents Are Equal

V_s - Space Potential, Probe at Same Potential as Plasma

A-B - Electron Collection

B-C - Ion Collection, Part Relevant to the Double Probe Analysis

Figure 15. Schematic of the Langmuir Probe Characteristic Curve.

the DPM appears to have an advantage in this respect. Also, in an electrodeless type discharge as used in the experiments to be discussed later where there is no reference electrode for the SPM, it is advantageous to use the DPM.

The equation developed by Johnson and Malter for the electron temperature is:

$$T_e = \frac{e}{k} \frac{\sigma}{(1+\sigma)^2} \left[\Sigma i_p \cdot \frac{dV_d}{di_d} \right] \tag{71}$$

where

e = electronic charge

k = Boltzman constant

$$\sigma = \left[\frac{\Sigma i_p}{i_{e_2}} - 1 \right]_{V_d=0} = \frac{A_1 j_{o1}}{A_2 j_{o2}} e^{\frac{eV_s}{kT_e}}$$

$i_p = i_{p1} + i_{p2}$

dV_d/di_d = the equivalent resistance or slope of the current vs. voltage curve at the origin.

See Figures (16) and (17) for diagrams illustrating the above quantities. For the case where the probes are of equal area, random current density at both probes are equal, the constant emf between the probes is zero, and the space potential near both probes is the same, then equation (71) reduces to

$$T_e = \frac{e}{k} \frac{i_+}{2} \frac{dV_d}{di_d} \tag{72}$$

If the current magnitudes are not the same but the curve passes near or through the zero point, then a good approximation can be made by writing:

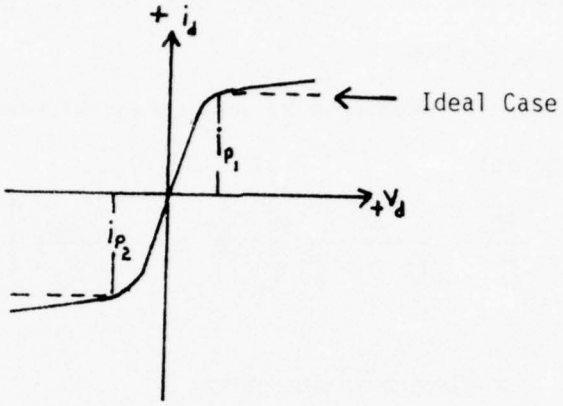

Figure 16. Voltage-Current Characteristic of the Double Probe.

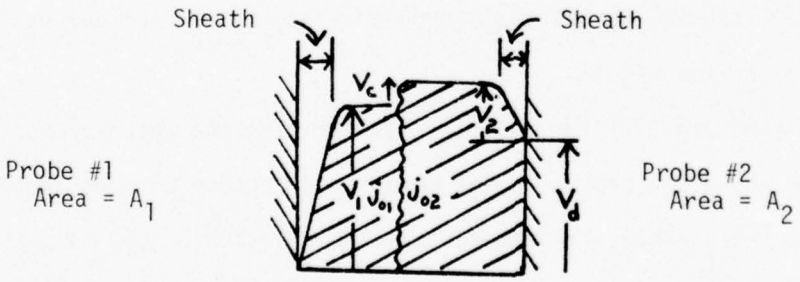

Figure 17. General Potential Diagram for the DPM.

j_{o1} = Electron Space Current Near Probe #1
j_{o2} = Electron Space Current Near Probe #2
v_1 = Probe to Plasma Potential Probe #1
v_2 = Probe to Plasma Potential Probe #2
v_c = Contact EMF Between Probes (= 0 for Symmetrical Probes)

$$T_e = \frac{e}{K} \frac{i_{p_1} \cdot i_{p_2}}{i_{p_1} + i_{p_2}} \cdot \left(\frac{d V_d}{d i_d} \right)_{V_d = 0} \tag{73}$$

For the nearly symmetrical probe characteristic, it can be shown that:

$$\frac{i_d}{i_{p_1}} = \tanh \left[\frac{e V_d}{K T_e \cdot 2} \right] \tag{74}$$

The traces made in the experiments closely followed this relationship, see Figure (18) for a typical double probe trace from the R.F. experiments. Johnson and Malter noted in their article that only the electrons sampled in the DPM are the top few percent of the distribution and thus the electron temperature determined will be somewhat higher than the average Maxwellian temperature. The electron mean free path in the experiments was about ten times the probe diameter and Langmuir's theory for electron collection would be approximated.

Now that a method is available for determining the electron temperature, it is necessary to find an equation which will give the ion density utilizing T_e. For the pressures involved in the experiments, it was not possible to use the collision-free Langmuir model for ion collection. For density measurements at high pressures, the papers of the following authors were consulted: Waymouth [11], Cohen [12], and Su and Lam [13]. These investigators analyzed spherical probes that collected current in dense plasmas where the mean free path is much smaller than or on the order of the probe radius. If one takes their final equations and reduces them for ion collection at high negative potentials and $T_e >> T_i$, they all approach the same form as will be shown.

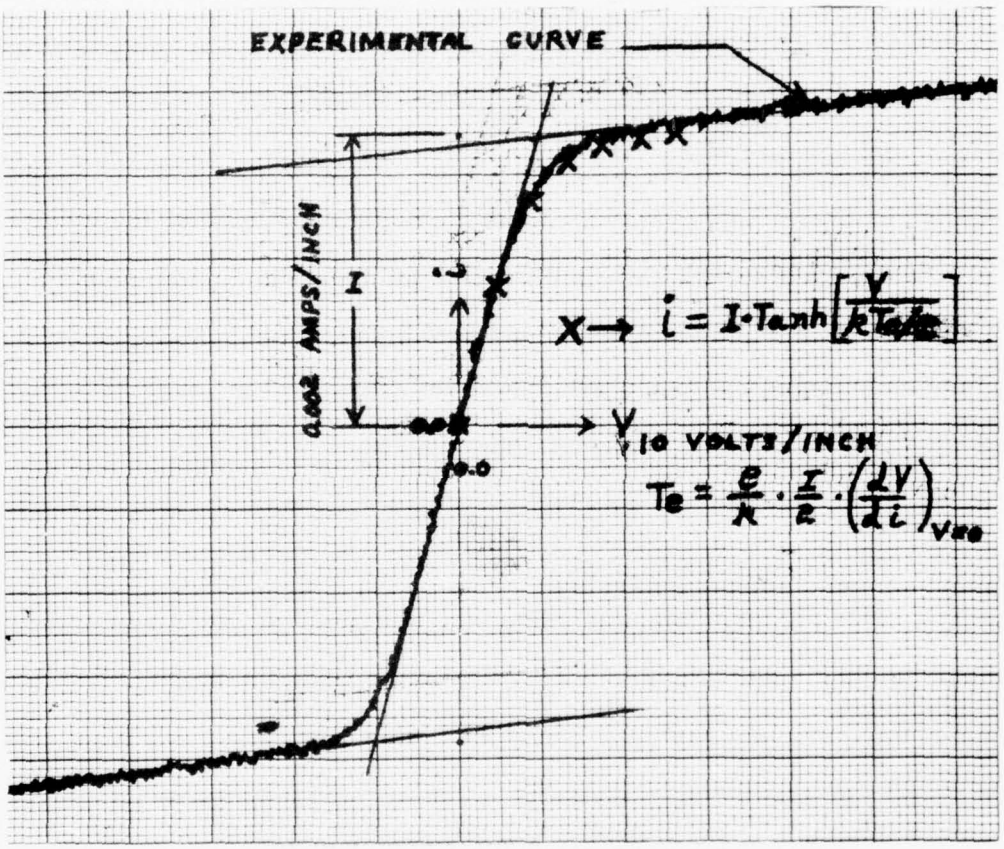

Figure 18. Comparison of Experimental and Theoretical D.P.M. Traces.

Waymouth based his derivation on the assumptions that $\lambda_c/r_p < 10$, $r_p/100\ \lambda_D > 1.0$, and $\lambda_c/\lambda_D > 10$, where λ_c is the particle mean free path, λ_D is the Debye length, and r_p is the probe radius. The potential of any chosen ion or electron in a plasma drops off as $q/r \cdot e^{-r/\lambda D}$ instead of q/r as in free space. The field of the chosen ion can be regarded as being effectively screened off at distances beyond λ_D where

$$\lambda_D = \sqrt{\frac{\epsilon_o k T_e}{n_e e^2}} \tag{75}$$

Su and Lam, along with Cohen, assumed that the probe radius is large compared with the Debye length. Su and Lam assumed very large probe potentials and very large T_e/T_i, while Cohen kept them finite in his analysis; for Cohen $\lambda_c \leq 10\ \lambda_D$. Figure (19) shows the regions of applicability based on the assumptions. On the figure are points calculated from the experiment. Since all theories reduced to essentially the same form for $T_e/T_i >> 1$ and large negative potentials, any data points falling within the Waymouth and Cohen regions can be analyzed by equation (97). Those few points falling outside the region were near the center of the duct where the electron density was low and the total temperature increase was quite small; hence, any errors here would have a small effect on the average total temperature calculation. See Table 11 for indications of the magnitude of ion number density and electron temperature.

First consider Su and Lam:

$$\epsilon = \frac{T_i}{T_e} \qquad T_i \text{ - ion temperature} \tag{76}$$

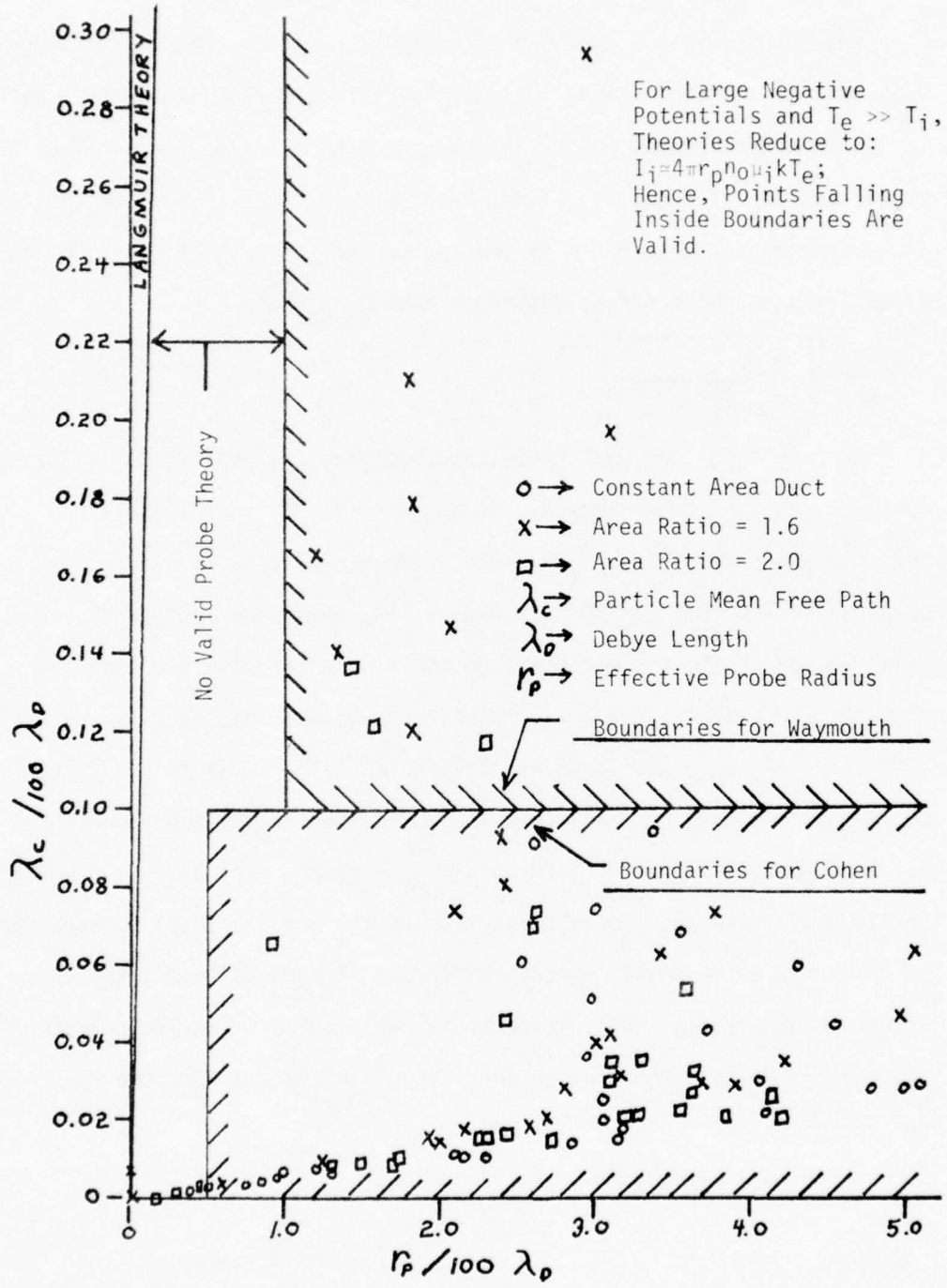

Figure 19. Domain of Validity for Probe Theories with Data Points Shown.

$$\frac{\epsilon}{\epsilon+1}\ \frac{I_i}{I_R} = c \qquad c \text{ - constant order (one)} \qquad (77)$$

$$I_R = 4\pi r_p n_o \mu_i k T_i \qquad \mu_i \text{ - ion mobility}, \quad n_o \text{ - ion density} \qquad (78)$$

$$I_i = c\,\frac{\epsilon+1}{\epsilon}\ 4\pi r_p n_o \mu_i k T_i \qquad (79)$$

$$I_i = c\,(\epsilon+1)\,4\pi r_p n_o \mu_i k T_e \qquad (80)$$

for $T_e \gg T_i$ (which is the case for the experiments)

$$I_i = c\,4\pi r_p n_o \mu_i k T_e \qquad (81)$$

From Waymouth we have:

$$J_i = \frac{e n_o}{1+Q_i}\sqrt{\frac{e V_{is}}{2\pi m_i}} \qquad V_{is} = kT_i/e,\quad V_e = kT_e/e \qquad (82)$$

$$Q_i = \frac{r_p}{\mu_i (V_e+V_{is})}\sqrt{\frac{e V_{is}}{2\pi m_i}} \qquad (83)$$

$$J_i = \frac{e n_o \sqrt{e V_{is}/2\pi m_i}\ \mu_i (V_e + V_{is})}{\mu_i (V_e + V_{is}) + r_p \sqrt{e V_{is}/2\pi m_i}} \qquad (84)$$

$$J_i = \frac{e n_o \mu_i (V_e + V_{is})}{\frac{\mu_i (V_e + V_{is})}{\sqrt{e V_{is}/2\pi m_i}} + r_p} \tag{85}$$

$$J_i = e n_o \mu_i \kappa \frac{T_e}{e} (1 + \epsilon) \tag{86}$$

$$T_i << T_e$$

$$I_i = 4\pi r_p n_o \mu_i \kappa T_e \tag{87}$$

Finally from Cohen

$$J_+ = (1 + \lambda/\epsilon)(1 - S_\rho / [\xi_\rho^{2/3}(1 + \tfrac{1}{\epsilon})^{1/3}]) \qquad \rho_\rho \to \infty \tag{88}$$

$$J_+ = (1 + \lambda/\epsilon)(1 - \xi_\rho / \xi_\rho^{2/3}) \qquad \rho_\rho \to \infty \; ; \; \frac{T_i}{T_e} \to 0 \tag{89}$$

where ρ_p is the radius of the probe divided by the Debye length and $\lambda = \epsilon(J_+ - J_-)/(\epsilon(J_+) + J_-)$. $\lambda \to 1$ as the potential becomes very negative and causes J_- to go to zero. J_+ can be written:

$$J_+ = \frac{I_+}{4\pi r_p^2} \cdot \frac{r_p}{e D_+ n_o} = \frac{I_+}{4\pi r_p} \cdot \frac{1}{e D_+ n_o} \tag{90}$$

where D_+ is the diffusion coefficient, and

$$D_+ = \frac{\kappa T_i}{e} \mu_i \tag{91}$$

where μ_i is the ion mobility. Utilizing the tables in Cohen, equations (88) and (89) can be written:

$$J_+ = \left(1+\frac{1}{\epsilon}\right)\left(1+\frac{10\epsilon}{21.5}\right) \cong 1.025\left(1+\frac{1}{\epsilon}\right) \tag{92}$$

$$J_+ = \left(1+\frac{1}{\epsilon}\right)\left(1+\frac{4}{21.5}\right) = 1.19\left(1+\frac{1}{\epsilon}\right) \tag{93}$$

or

$$J_+ = c\left(1 + T_e/T_i\right) \tag{94}$$

where C is the order one; thus, we can write:

$$I_+ = c \cdot e\, 4\pi r_p \mu_i \frac{kT_i}{e} n_o \left(1 + T_e/T_i\right) \tag{95}$$

and for $T_e >> T_i$:

$$I_+ = c\, 4\pi r_p n_o \mu_i k T_e \tag{96}$$

This is the same form as equations (81) and (88).

Thus the equation used for determining the ionization level was derived from:

$$I_+ = 4\pi r_p n_o \mu_i k T_e \tag{97}$$

where T_e is determined as shown earlier.

The ion mobility μ_i is determined by

$$\mu_i = \mu_{i_o} \frac{\rho_{io}}{\rho} \frac{T}{T_{io}} = \mu_{i_o} \frac{g_{io}}{g_i} \tag{98}$$

where ρ_{io} refers to the density at standard conditions and μ_{io} is the mobility for standard conditions which is a known constant.

$$\mu_i = \mu_{i_o} \frac{1.03 \times 10^5}{nkT} \cdot \frac{T}{273} \tag{99}$$

Hence, we can write:

$$I_+ = 4\pi r_p \frac{n_o}{n} \cdot \frac{\mu_{i_o}}{k} \cdot \frac{1.03 \times 10^3}{2.73} kT_e \tag{100}$$

and since $n_o/n = \alpha$, the degree of ionization, we have:

$$\alpha = 2.69 \times 10^{-3} \frac{I_+}{4\pi r_p \mu_{i_o} T_e} \tag{101}$$

$I_+ \rightarrow$ saturation ion current measured from I vs. V curve.

This is the equation used to determine α for correcting the total temperature measurement. The radius of the probe r_p is for a spherical probe; the probes used in the experiments were cylindrical. Waymouth [11] suggested, in light of the physical mechanism he considered, that two probes that draw the same current from a given plasma will cause the same perturbation; and since probes draw current in proportion to their areas, one could say the cylindrical probe has an effective radius equal to the radius of the sphere with the same surface area:

$$r_{p_{eff}} = \left(\frac{1}{2} r_p \ell\right)^{1/2} \quad \text{for wire probes,} \tag{102}$$

where r_p is cylindrical radius and ℓ is length of the wire.

$r_{p_{eff}}$ is the radius used in equation [101].

Next we will derive the equation for correcting the measured total temperature for ionization.

$$\frac{1}{2} u^2 + h + e_v = h \tag{103}$$

where

$$h = C_p T_A + C_{p_{em}} \cdot T_e$$

T_A → Argon gas static temperature

T_e → electron temperature

$$C_{P_{em}} = \propto C_{p_e} \frac{m_e}{m_N}$$

$$ev = \propto \frac{EV}{m_N}$$

EV → Energy for ionization of argon atom.

Thus assuming complete recombination, one may write:

$$\frac{u^2}{2} + C_p T_A + \propto C_{p_e} \frac{m_e}{m_N} T_e + \propto \frac{EV}{m_N} = C_p T^\circ \tag{104}$$

$$\frac{u^2}{2C_p T_A} + 1 + \frac{\propto C_{p_e} m_e T_e}{C_p m_N T_A} + \frac{\propto EV}{C_p T_A m_N} = \frac{T^\circ}{T_A} \tag{105}$$

$$\frac{\gamma-1}{2} M^2 + 1 + \propto \frac{T_e}{T_A} + \frac{\propto EV}{C_p T_A m_N} = \frac{T^\circ}{T_A} \tag{106}$$

or, since

$$\left[\left[\frac{\gamma-1}{2}\right] M^2 + 1\right] T_A = T^\circ_{ACTUAL} \tag{107}$$

$$T^\circ_{ACTUAL} = T^\circ - \propto \left(T_e + \frac{EV}{C_p m_N} \right) \tag{108}$$

This is the equation used for correcting the total temperature measurement, where $EV/C_p m_N$ for Argon is equal to 6.9×10^4 °K.

With regard to the errors arising from the electrostatic probe measurements, the comments of two authors are cited. Danikov and Gruglyakov [14] indicate that at pressures on the order of 1 mm Hg, the electron density determined by electrostatic probe measurements could be low by a factor of two. Schulz and Brown [15] indicate that plasma number densities, using single or double electrostatic probes, can be determined within a factor of two up to pressures of 6 mm Hg. Thus, based on the above observations, the error in measured electron number density or α in equation (108) should be on the order of two. However, the constants dropped from the Su & Lam and Cohen results were on the order of 1.1 and 1.2, which would indicate errors up to 20% if one ignored the higher than normal electron temperature mentioned earlier in Johnson and Malter's work.

The assumption that the recombination is 100 percent in the total probe and all the energy is converted into thermal energy of the particles is a reasonable one based on the results of a paper by Chen [18]. From his work, it is found that during recombination for Argon at the electron densities found in the experiments, about 90 percent of energy released is transferred to the electron gas and 10 percent is in the form of radiation. Thus, inside the total temperature probe, most of the radiation can be trapped by the surrounding walls and eventually transferred to the gas molecules through collisions. By collisions, thermal energy is transferred from the electron gas to the molecules. Even as the electron density approaches zero, 75 percent of the energy released

during recombination is carried away by other electrons to be transferred to the gas by collisions. Based on the probe I.D. and the diameter of the four bleed holes, the residence time in the probe is about 10^{-4} seconds. Based on an ion flux to the walls of $1/4\ n_i\ \bar{c}_i$, the 10^{-4} seconds is plenty of time for all the ions to travel to the wall and thermocouple and recombine, releasing the energy at the surface. Based on the above discussions, it is reasonable to assume complete recombination within the total temperature probe.

Another mode of energy loss may arise from existence of the metastable states of Argon. Following the method of Hinnov and Hirschberg [17], the number density of the metastable states will be calculated. The assumption is that the metastable states are in transient equilibrium with the electron temperature, which results in the equation:

$$\frac{n_m}{n_e} = n_e \frac{g_m}{g_i g_e} \left[\frac{h^2}{2\pi m_e k T_e} \right]^{3/2} \cdot e^{E_m/kT_e} \tag{109}$$

Substituting the appropriate values based on the experimental data, we have:

$$\frac{n_m}{n_e} = 9.15 \times 10^{13} \frac{2}{2 \cdot 4} \left[\frac{(6.62)^2 \times 10^{-68}}{2\pi \times 1.38 \times 1.84 \times 10^{-49}} \right]^{3/2} \cdot e^{\frac{4.15}{1.72}} \tag{110}$$

$$\therefore \frac{n_m}{n_e} = 3.65 \times 10^{-8} \tag{111}$$

Thus the equilibrium metastable population is insignificant when compared to the electron density, and the contribution to the energy can be ignored in the calculations. Calculations of the power radiated from

the gas due to recombination of ions and electrons using experimental and theoretical recombination coefficients indicated that it was insignificant compared to the heat input to the gas.

Since an R.F. field was used to heat the gas, magnetic fields were present due to the time varying electric field. It then is necessary to mention the effect of a magnetic field on the double probe operation. From Chen [18], it is observed that, for electrons in thermal equilibrium and an ion Larmor radius much larger than the probe dimensions (weak magnetic field), the usual theories of ion collection can be used. In the gas flow experiments, the electrons appeared to be Maxwellian, the probe was far enough downstream of the coil so that the magnetic field was weak, and ion collection was the probe's mode of operation; thus, under the test conditions, the magnetic field had no noticeable effect.

R.F. Energy Addition

The energy addition in the experiments was provided by radio frequency (R.F.) induction heating using a 5 KW Lepel R.F. generator. The electric field generated by the R.F. coil initially accelerates several free electrons to an energy where they can ionize Argon atoms leading to more electrons and an avalanche which provide an ionized gas or plasma. The energy transfer for heat addition can be considered due to electron collisions with the neutrals and ions which transfer energy rather than ionizing the molecule or atom. A simple analysis illustrates the power input to the gas by electrons.

The momentum equation can be written for elastic collisions as:

$$m_e \frac{d^2x}{dt^2} = e E_a \sin \omega t - \nu m_e \frac{dx}{dt} \tag{112}$$

The collision term is based on elementary collision theory where the electron behaves like a very light elastic sphere which loses all its momentum in any given direction at each collision with a much larger particle.

Equation (112) can be written:

$$(D^2 + \nu D)x = \frac{e E_a}{m_e} \sin \omega t \tag{113}$$

Assuming a particular solution of equation (113) in the form $x = C \cos\omega t + F \sin \omega t$ and substituting into equation (113) solving for C and F, it is found that:

$$x = \frac{eE_a}{m_e} \left[\frac{-\sin \omega t}{\nu^2 + \omega^2} - \frac{\omega \nu \cos \omega t}{(\omega\nu)^2 + \omega^4} \right] \tag{114}$$

the drift velocity is $V_d = dx/dt$, hence:

$$V_d = \frac{eE_a}{m_e} \left[\frac{-\omega \cos \omega t}{\nu^2 + \omega^2} + \frac{\nu \sin \omega t}{\nu^2 + \omega^2} \right] \tag{115}$$

the current density is

$$j = \frac{n_e e^2 E_a}{m_e} \left[\frac{-\omega \cos \omega t}{\nu^2 + \omega^2} - \frac{\nu \sin \omega t}{\nu^2 + \omega^2} \right] \tag{116}$$

The power density can be written $P = jE$, where $E = E_a \sin \omega t$ is the applied field. Making the appropriate substitutions, it is found that:

$$P = \frac{n_e e^2 E_a}{m_e} \left[\frac{-\omega \cos \omega t \sin \omega t}{\nu^2 + \omega^2} + \frac{\nu \sin^2 \omega t}{\nu^2 + \omega^2} \right] \tag{117}$$

Multiplying equation (117) by dt, dividing by the period $T = 1/f = 2\pi/\omega$, and integrating from 0 to T, the average power per unit volume is found to be:

$$\langle P \rangle = \frac{n_e e^2 E_a^2}{2 m_e} \cdot \frac{\nu}{\nu^2 + \omega^2} \tag{118}$$

By writing the kinetic energy of an electron K.E. = $1/2\ mV_d^2$, multiplying by dt, dividing by the period, and integrating from 0 to T, it can be shown that the average kinetic energy of an electron in terms of electron volts can be written:

$$\langle K.E. \rangle = \frac{e E_a^2}{m_e} \cdot \frac{1}{\nu^2 + \omega^2} \tag{119}$$

Dividing equation (118) by equation (119), we find:

$$\frac{\langle P \rangle}{\langle K.E. \rangle} = 2 n_e e \nu \tag{120}$$

or

$$\nu = \frac{\langle P \rangle}{\langle K.E. \rangle} \cdot \frac{1}{2 n_e e} \tag{121}$$

The electric field E_a will be calculated along with the ion temperature to see if the experimental data is reasonable.

<P> is determined by dividing the power into the gas by the volume of the coil region. The volume is given by Vol = $\pi L\ (r_1^2 - r_2^2)$ where L is the coil length and r_1 and r_2 are the radius boundaries of the maximum temperature region. Substituting the appropriate values, we find Vol $\approx 4 * 10^{-6}\ m^3$. The value of power is $\approx$ 100 watts, which is about the maximum in the experiments; hence, <P> = 2.5×10^7 watts/meter^3. The term <K.E.> is determined by the measured electron temperature.

Using the maximum values from the 1.6 area ratio experiments for electron temperature (3×10^4 °K) and electron density (10^{19} particles/meter^3), we find from equation (121) that $\nu = 2.22 \times 10^6$ collisions per second for $\omega = 2.5 \times 10^7$. Substituting the above values back into equation (119) and solving for E_a, it is found that $E_a \simeq 2.3$ volts/cm. This is a reasonable value for the electric field in the plasma based on data available in Brown [19].

Next let's calculate what the ion or neutral temperature will be in the region of maximum energy input. An electron in an elastic collision will transfer about $2m_e/m_i$ of its energy in an elastic collision. The residence time of the flow in the coil region is $t \simeq 10^{-4}$ seconds. The change in temperature experienced by the ions and neutrals can be written:

$$\Delta T_i = \frac{2 m_e}{m_i} \nu t \, T_e \qquad (122)$$

Substituting the values, it is found that:

$$\Delta T_i = 326°R \qquad (123)$$

$$T_i = 550 + 326 = 876°R \qquad (124)$$

550 is initial gas temperature

The above value for T_i compares well with the experimental value of T_i in the region near the wall, $T_{i_w} \simeq 1000°R$.

The above analysis shows that the measured values of T_e, n_e, and T_i are reasonably correct and the theory can describe the energy addition process. Using T_e to calculate, <K.E.> is reasonable since $\bar{c}_e = \sqrt{8KT_e/\pi m_e} = 8.7*10^5$ meters/second; and, $V_d = 1/2\ eEa/(m_e\omega)$, which <K.E.> depends upon, equals $7.4*10^5$ meters/second.

SECTION IV

EXPERIMENTAL EQUIPMENT AND PROCEDURE

Gas Flow Apparatus

For the radio frequency (R.F.) heating of the inert gas, an electrically non-conducting material was needed for duct fabrication. This was necessary to prevent the R.F. water-cooled copper coil (which surrounds the duct) from heating the duct by induction currents rather than heating the gas. Two materials were used to make the ducts, Pyrex glass and Boron Nitride, with the latter being used in the majority of experiments. Boron Nitride is a high temperature, easily-machined refractory material with a melting point of 2730°C; and, it is a good electrical insulator. Pyrex glass ducts were abandoned after the first few runs because they became plastic during high energy inputs to the gas. The gas chosen for the experiments was Argon, since it is easily ionized and relatively inexpensive. Ionization of the gas is necessary so that the electric fields generated by the R.F. coil can induce electric currents which result in gas heating.

The power required for heating the gas was provided by a 0.5 Kilowatt (KW) 11 megacycle R.F. power supply or a LEPEL 5 KW 4-8 megacycle power supply; the latter was used in the majority of the experiments. The R.F. power supply was connected to the R.F. coil as shown in Figure (20). A Jennings 15 KV 0-25 μμF variable capacitor

was used to tune the R.F. duct coil to the power supply. This tuning permitted one to find the breakdown point (ionization occurs) and to adjust for the most efficient power transfer. The copper coil wrapped around the duct was 10-11 turns of 1/8" O.D. water-cooled tubing of about one microhenry inductance.

To ionize and heat the Argon gas, pressures on the order of several millimeters of Hg are required. To achieve these low pressures, a vacuum pumping system was used that could maintain a back pressure of one millimeter of Hg at an Argon flow rate of 10^{-2} lb_m per second. Some of the initial experiments used a facility with about half the above capability. The pumping capacity and the low static pressures needed for ionization limited the total pressure in the nozzle chamber to 100 mm Hg; this total pressure restriction limited the Reynolds number of the flow. To achieve the high Mach number, low static pressure flow in the duct, two nozzles were fabricated using calculations based on the analysis of Foelsh [20]. His analysis provided for a parallel flow at the nozzle exit. The nozzles had design exit Mach numbers of 5 and 3.5 with an exit diameter of 0.969 inches. This diameter resulted from the fact that the Pyrex glass tubing used initially for the duct had an I.D. of 0.969 inches. The Reynolds number based on the duct diameter for the Mach 3.5 nozzle was about 35,000 and, as mentioned above, this could not be significantly increased due to ionization and pumping limitations.

Figures (21), (22), and (23) show a schematic and pictures of the nozzle and duct set-up. Experiments were made with the duct directly connected to the nozzle and separated from it, as shown in the

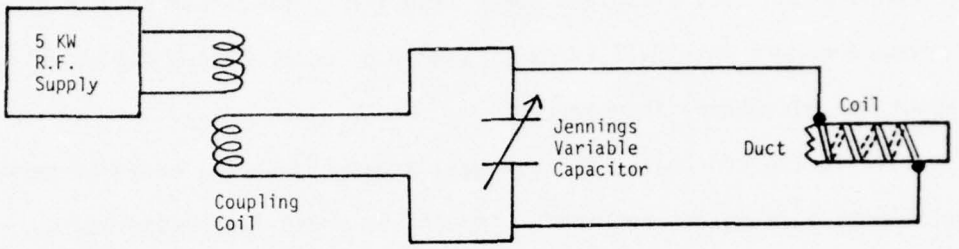

Figure 20. Schematic of Power Circuit.

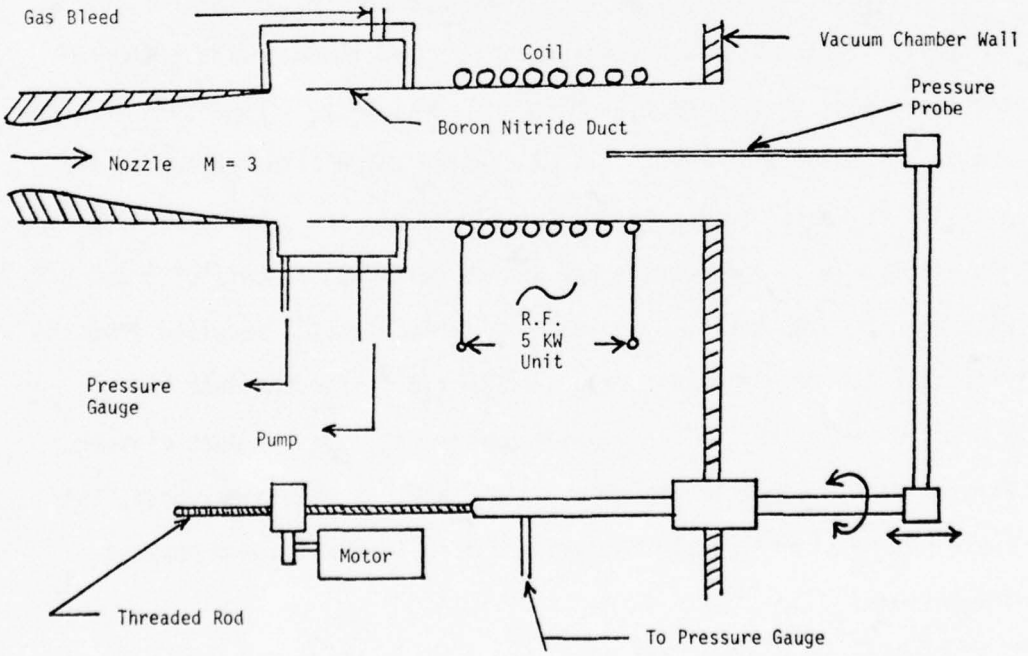

Figure 21. Test Apparatus.

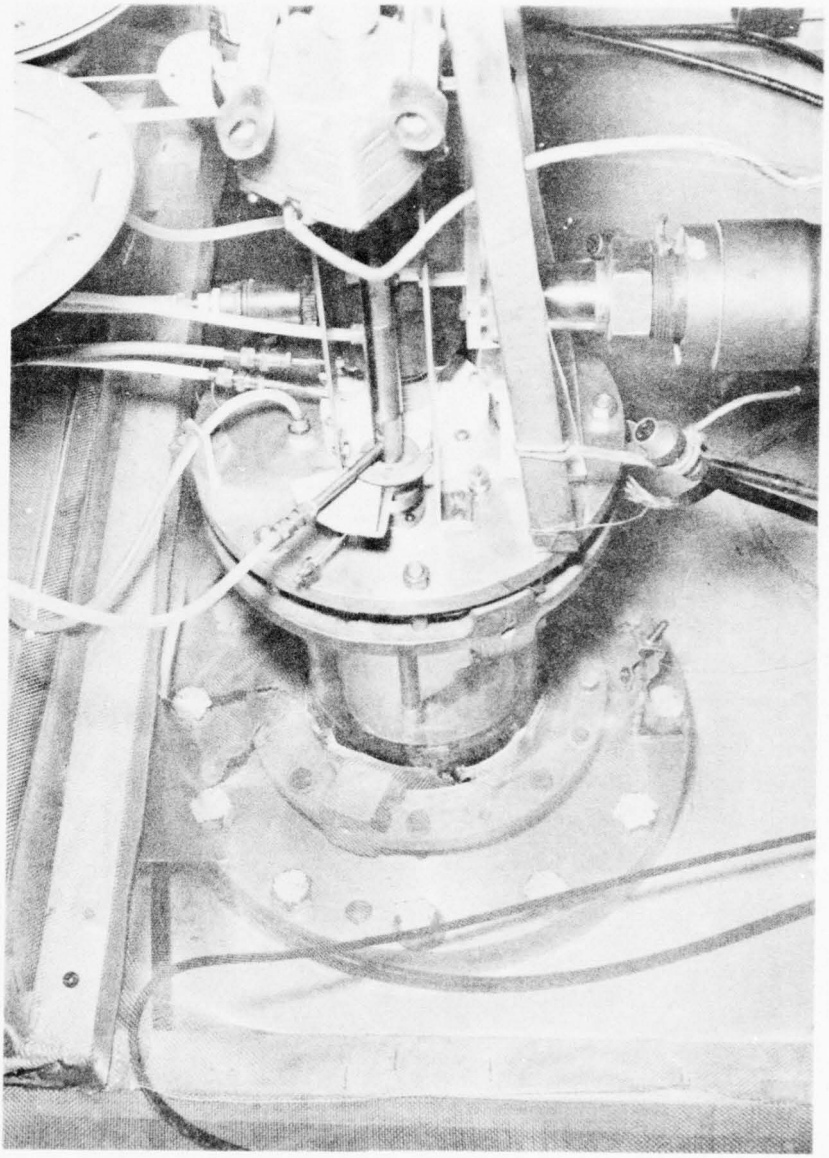

Figure 22. Photograph of Test Apparatus with Power Input to Gas.

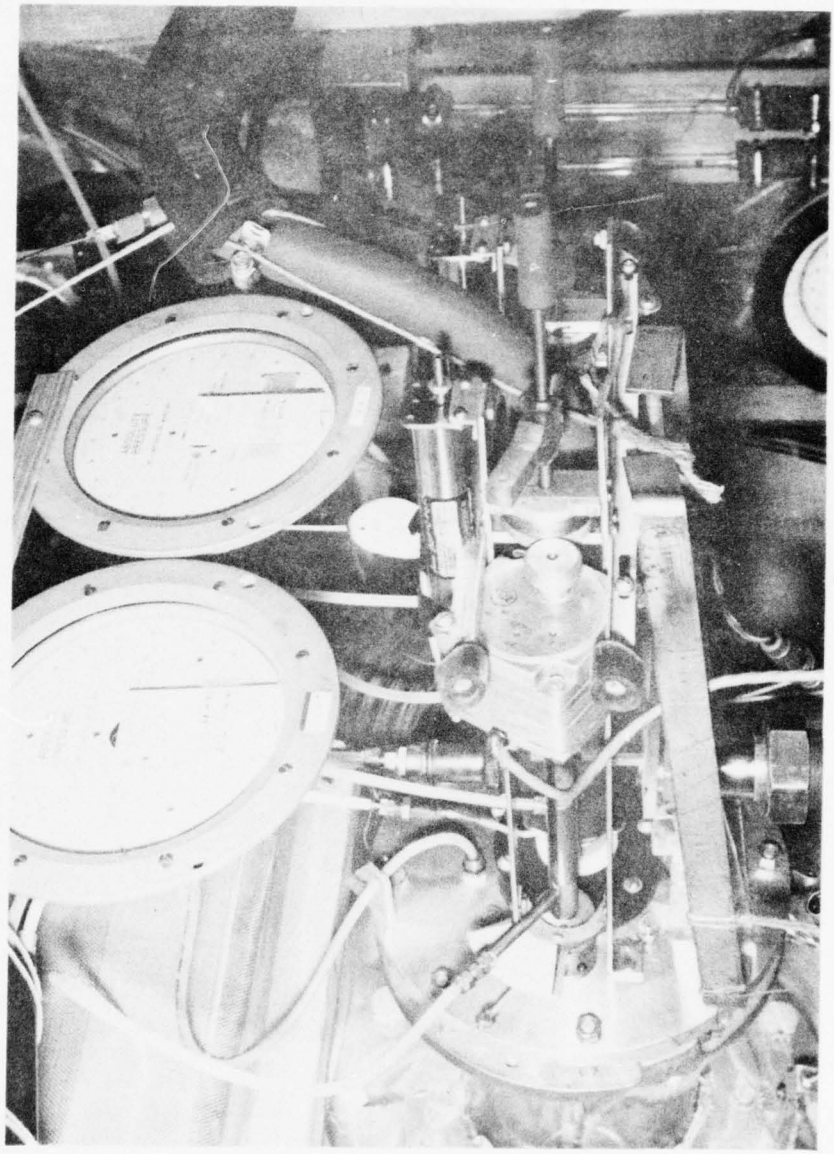

Figure 23. Photograph of Test Apparatus for Supersonic Gas Flow Energy Addition Tests.

schematic. To allow separations of the nozzle and duct, a small chamber made of phenolic was fabricated to which the duct and nozzle could be attached. The small chamber had two ports drilled in it which permitted a small gas bleed into one port and pumping on the other. This small chamber allowed for a free inlet operation of the duct by maintaining a constant pressure in between the nozzle exit and duct inlet. The pressure in the small chamber was maintained constant by having a small gas bleed (about four percent of the main flow) initially into the chamber which could be reduced as mass spillage occurred at the duct inlet due to heat addition. This operation permitted maintenance of a constant Mach number in front of the duct and mass spillage due to heat addition did not interfere with the nozzle flow. Fischer Porter flow tubes were used to monitor the mass flow into the nozzle and the small connecting chamber. Mass flow through the nozzle based on the measured chamber total temperature and pressure agreed within two percent of the mass flow indicated by the flow tube. An oil bath was set up to maintain the temperature of the Argon entering the nozzle at a constant 90°F.

Flow Measurement Probes

The Figures (21), (24), and (25) illustrate the pressure probes and their mounting arrangement. The pressure probes were constructed from ceramic tubing of 0.08" O.D. and 0.05" I.D. Ceramic instead of metal was used to prevent interaction with the R.F. coil. The probes are about 5 inches in length and were connected to stainless steel tubing which goes from the interior of the vacuum chamber to the exterior mounting system. An arrangement was made so that two probes could be mounted, one on each side of the duct and nozzle as seen in the above figures. A

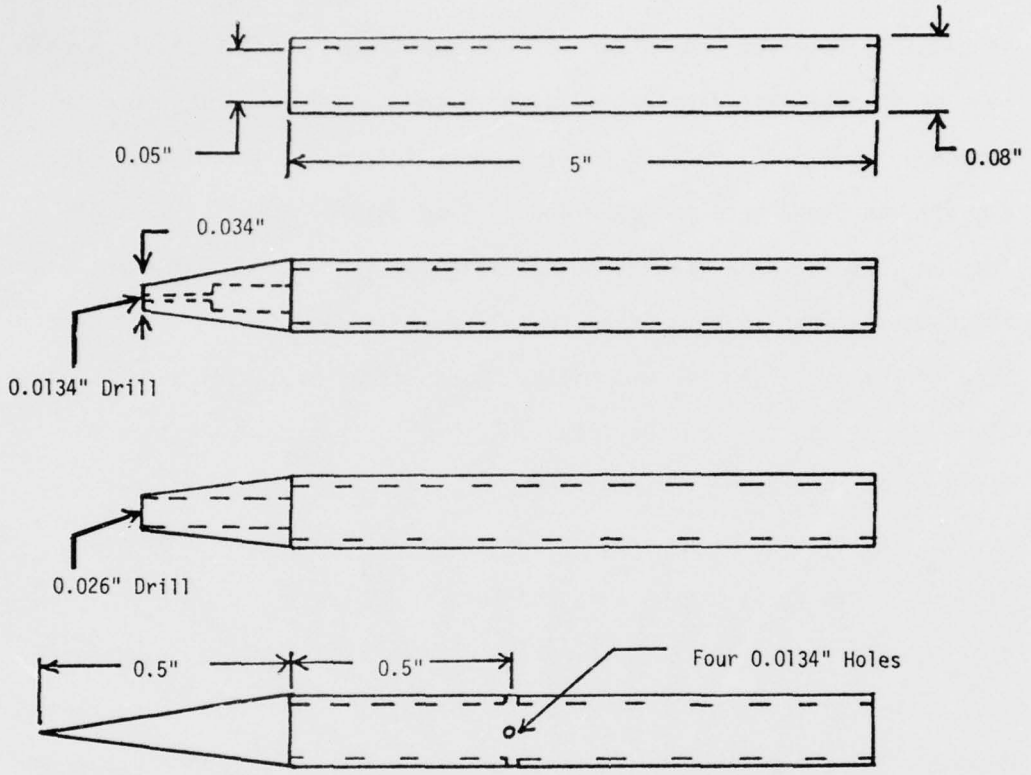

Figure 24. Pressure Probes.

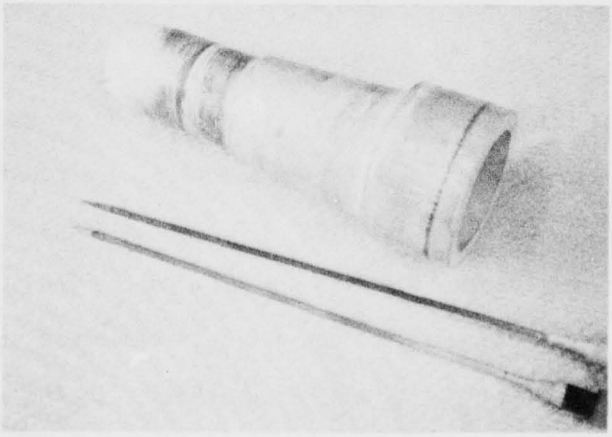

Figure 25. Static and Total Pressure Probes Along Side of a Boron Nitride Duct.

threaded rod was attached to the stainless steel tubing holding the probe; this rod passed through a threaded knurled nut which was driven by a low rpm motor permitting axial motion of the probe; movement was about 0.01" per second. The stainless steel tube holding the probe passed through a double O-ring seal in the flange attached to the vacuum chamber; this allowed the probe to be rotated, thus permitting radial measurements to be made in the duct. A securely-mounted (though still allowing rotation) slotted stainless tube surrounded the one to which the probe was attached; this acted as the guide for a 1/4" O.D. tube mounted 90° to the probe's stainless steel tube. A Tygon tube ran from the 1/4" O.D. tube to a Datametrics Barocel Electrometer Manometer, which has an accuracy of $\pm$ 0.03% of scale reading. Plots of static and total pressure along the length of the duct for a given radial position were obtained by having the movable probe attached to a Bourns 0-5000 Ω Align-O-Plot linear resistor and a battery which was connected to the X axis of a X-Y plotter. The 0-10 volt output of the electronic manometer was connected to the Y axis of the X-Y plotter. See Figure (26) for a sketch of X-Y plotter hook-up. Pressure measurements, static and total, were made along the duct at radial positions of 0.0R, 0.19R, 0.38R, 0.57R, and 0.76R from the center line. From these pressure measurements, the Mach number along the duct may be determined, using the Rayleigh pitot tube formula.

The 0.08" O.D. by 0.05" I.D. ceramic tubes were used for the probes because Pyrex tubing became plastic at the higher power levels when placed near the duct's wall. One total probe was just a flat-nosed ceramic tube; the other total probe had a truncated Boron Nitride 5°

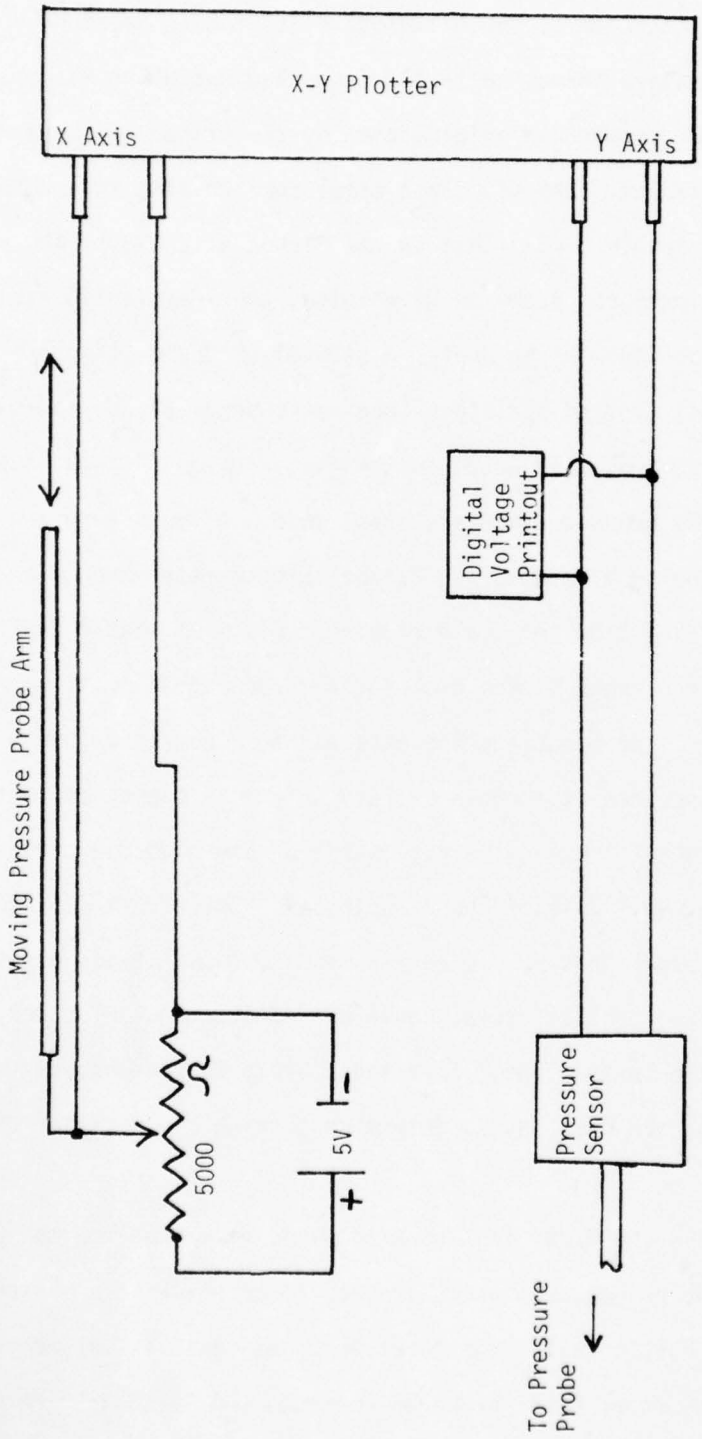

Figure 26. Pressure Measurement Schematic.

half-angle conical tip with a 0.026" hole. The static probe had a 5° half-angle 1/2" long Boron Nitride conical tip with four holes of 0.013" diameter ninety degrees apart at a distance of 1.0" from the cone's tip (the holes were drilled by Bendix Corp. using a cavitron drill). The total temperature probe had a Cromel-Alumel thermocouple placed in the center of the 0.08" O.D. ceramic tube 1/16" from the inlet with four 0.013" diameter holes ninety degrees apart 1/8" from the inlet to allow for a small mass bleed to help cancel heat conduction losses. The thermocouple is held in the center of the tube by a ceramic spacer to prevent it from touching the tube wall. Figures (24), (25), and (27) show the probes described above. Inclosing the thermocouple provides a low velocity flow around the thermocouple for which the static temperature is essentially the total temperature.

For use in conjunction with the total temperature probe, a Langmuir double probe was made to determine ionization levels so that corrections for ionization could be made to the measured total temperature. See Figures (28) and (29) for illustrations of the double probe. The double probe was constructed from ceramic tubing and 0.005" tungsten wire. The wires were spaced about 1/8 inch apart and were about 1/4 inch in length. The voltage was swept across the wires by a variable bi-polar power supply and the current was measured across a resistance in the probe circuit by the X-Y plotter. Reading the probe voltage on the other plotter axis resulted in a plot of probe current vs. voltage, see Figure (30) for a schematic of the circuit. The static and total pressures were measured first for all experiments; then, the pressure probes were removed and the total temperature probe and double probe were attached to the two probe

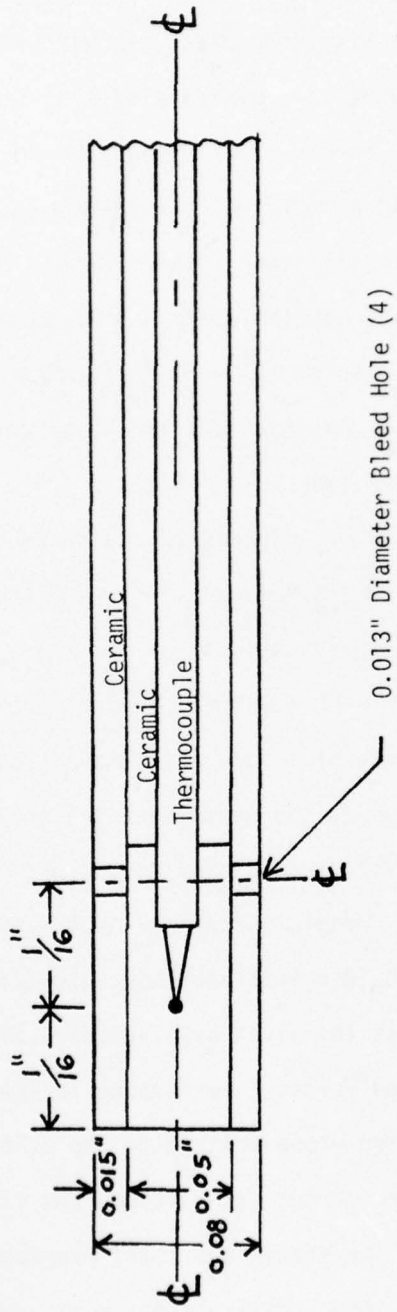

Figure 27. Total Temperature Probe Schematic.

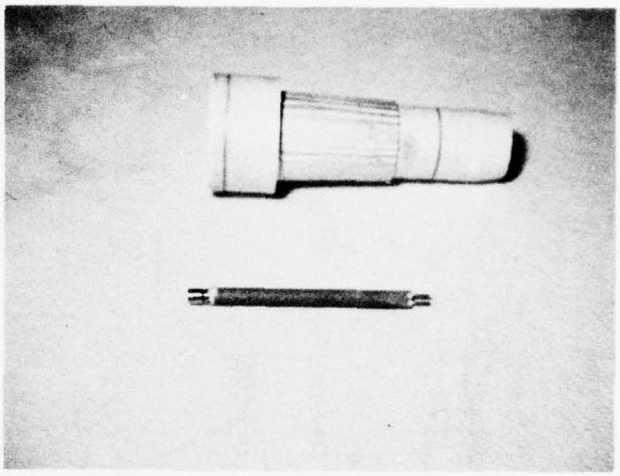

Figure 28. Double Probe.

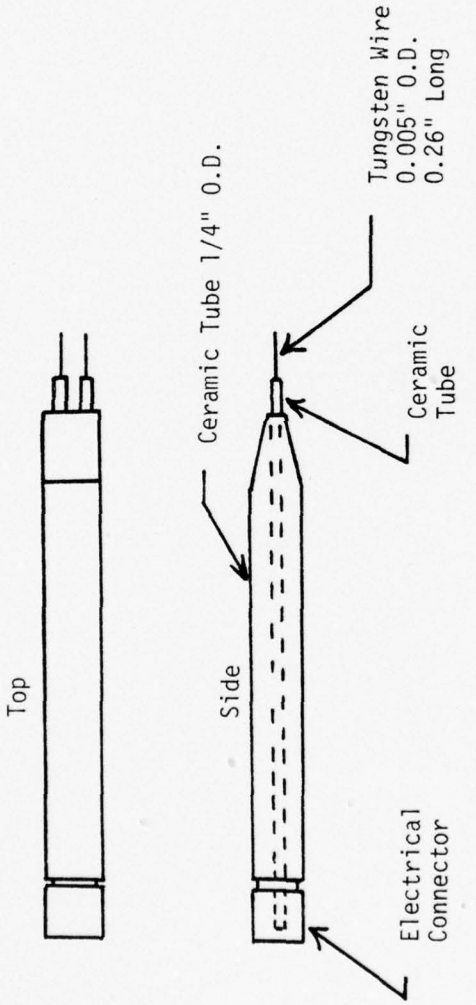

Figure 29. Double Probe Schematic.

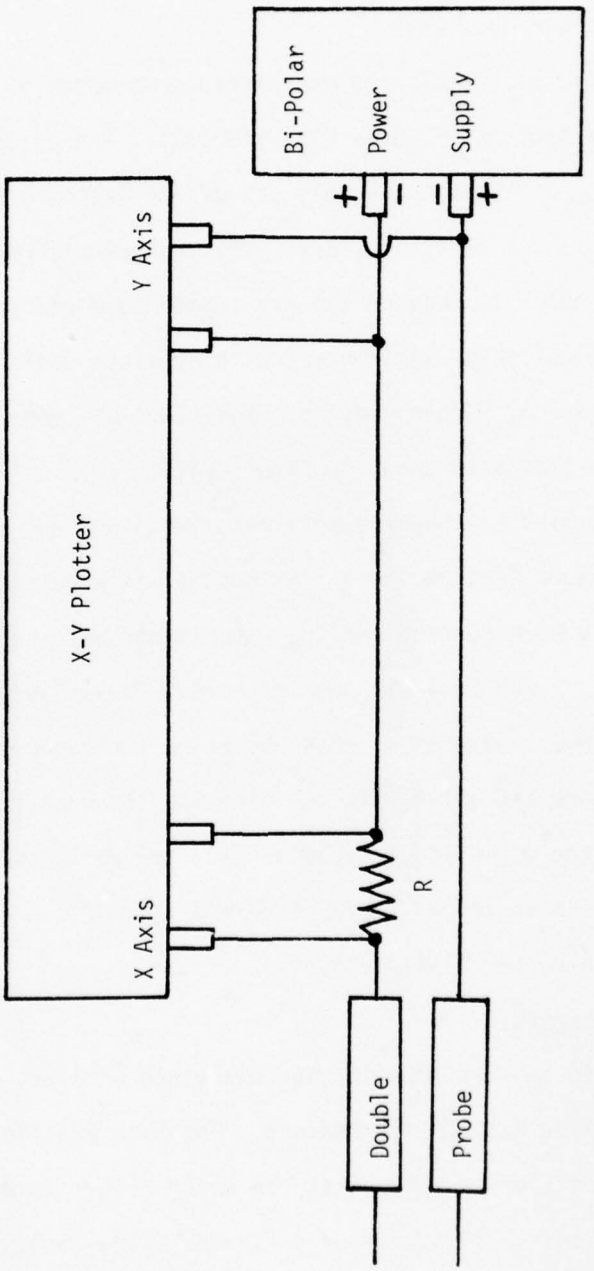

Figure 30. Schematic of Double Probe Circuit.

mounts. The flow conditions were then repeated for the previous experiments to obtain the corresponding total temperatures and ionization levels at the duct exit.

A collector was fabricated and placed downstream of the duct inside the vacuum chamber, see Figures (31) and (32). The collector was built to allow mixing of the hot and cold gas of the jet before emerging through four holes around the sides. Thermocouples were placed in the flow at these holes to measure the gas temperature before and after heat addition. The collector was covered with aluminum foil to reduce the amount of radiation. The collector temperature was monitored by thermocouples at the locations shown in Figure (31). This collector was used in conjunction with the power supply meter readings and mass by-pass readings to assure that the same flow conditions were repeated when the pressure probes were removed and the experiments were repeated using the total temperature and Langmuir double probe. The collector could also be used for a power measurement check by using the measured temperature difference before and after heat addition and the mass flow rate. A correction to the power input could be made for collector radiation loss by using the collector temperature and its surface area and the emissivity of aluminum (polished).

Water Table Apparatus

As noted in the introduction and discussed earlier, an analogy between water flow and gas flow exists. For heat addition to a gas this implies mass addition to the mainstream water flow. To accomplish this simulation the set-up illustrated in Figures (33), (34), and (35) was made for use on the Air Force Institute of Technology's water table.

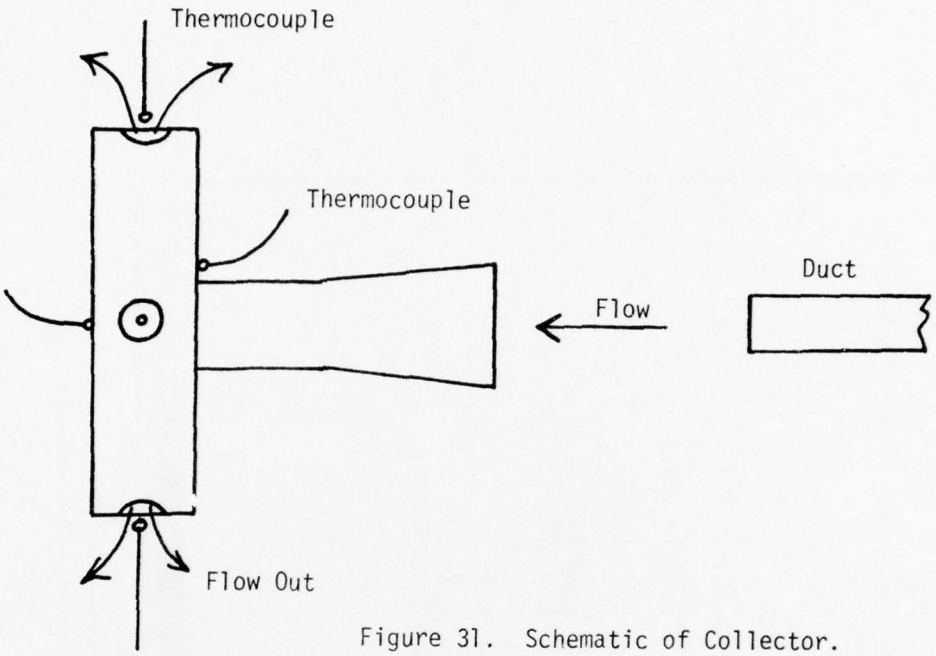

Figure 31. Schematic of Collector.

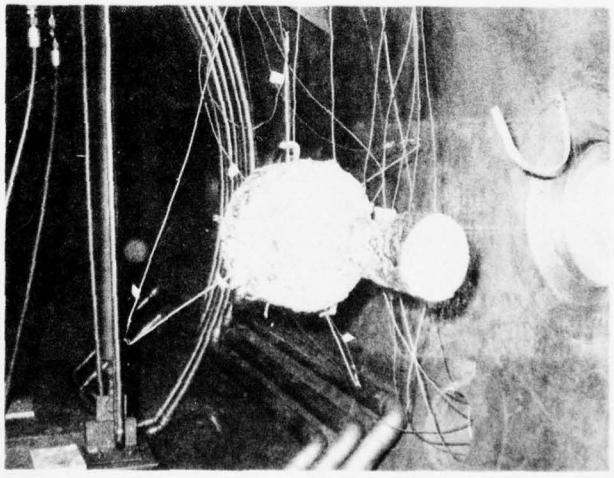

Figure 32. Collector As Seen Inside The Vacuum Chamber. To The Right Is The Port In Which The Collector Is Placed During Gas Flow Tests.

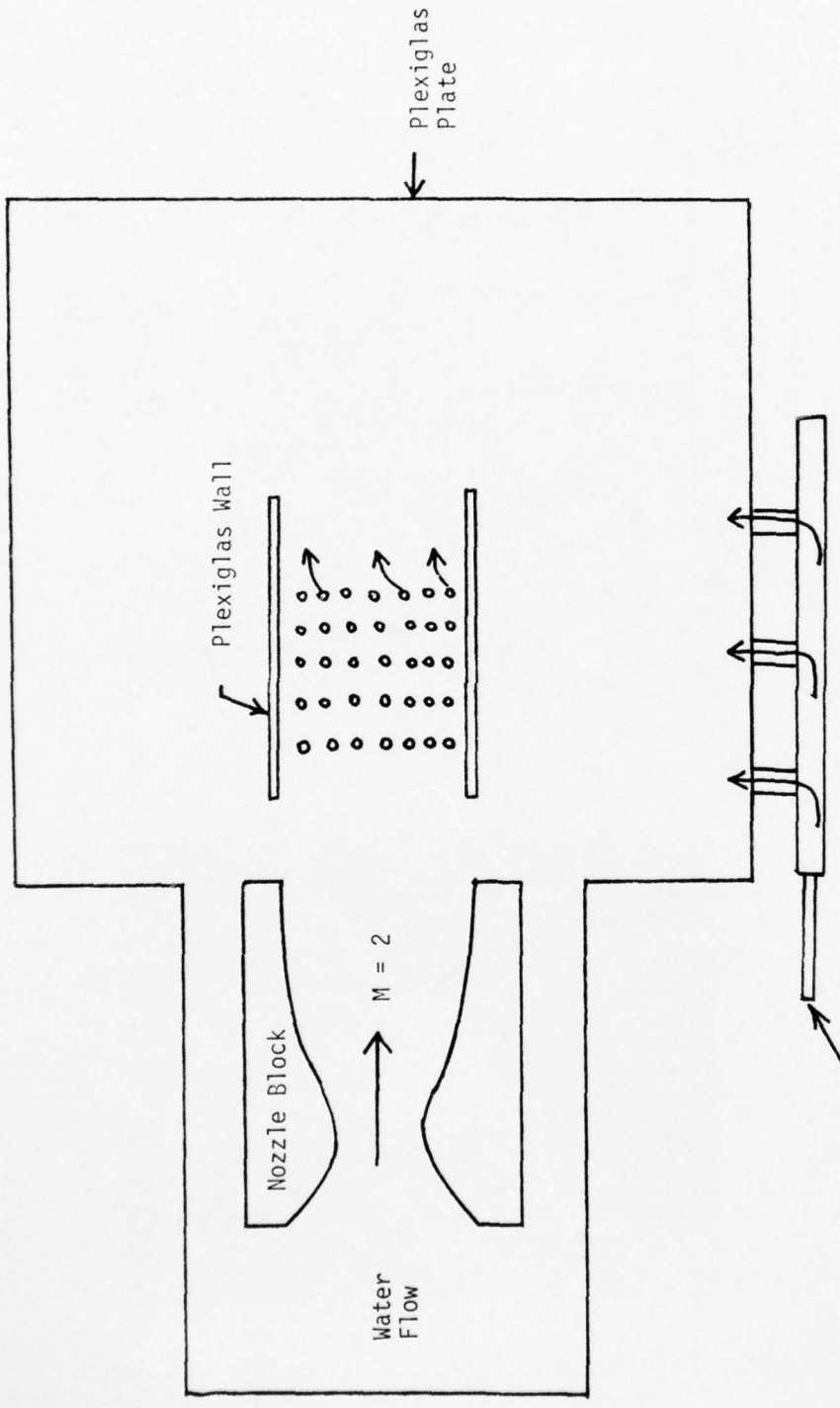

Figure 33. Water Table Schematic.

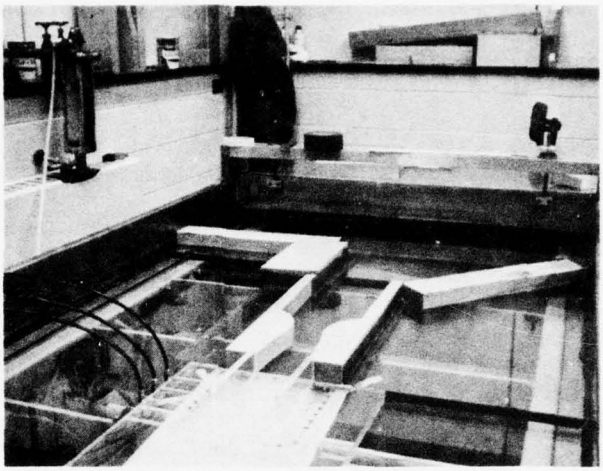

Figure 34. Water Table With Nozzle Direct-Connect Duct and Porous Injection Plate.

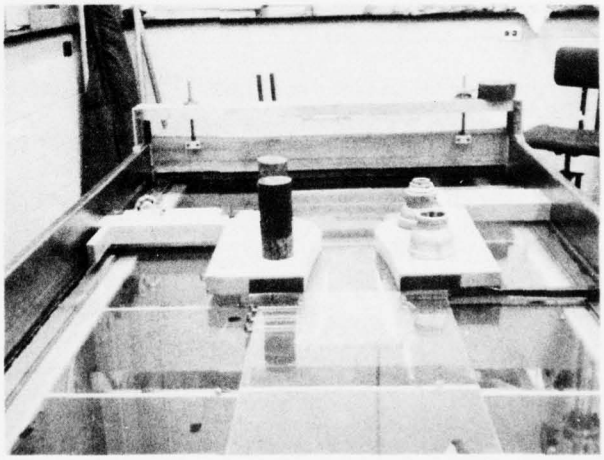

Figure 35. Water Table Test With Free Inlet Duct.

The water table is a device with a glass bottom which permits water flow from one end to the other at various adjustable flow rates. The glass bottom enables one to easily observe the wave patterns on the water surface.

A Mach 2 water nozzle was fabricated from wood based on two-dimensional wave characteristics for a gas having a gamma of two. The nozzle was placed on top of a 3/4" thick piece of plexiglas. Downstream of the nozzle a plenum was cut into the plexiglas and an injection plate with numerous holes was placed over this plenum flush with the surface. Walls for the simulated duct were made from plexiglas and were attached to or placed a few inches downstream of the nozzle exit; these walls were placed on both sides of the injection plate so that water could be injected from the bottom into the mainstream flow issuing from the water nozzle. This injection would simulate heat addition to a gas flow.

Photographs were taken from the side looking at the duct walls for various mass injection flow rates. These photographs permitted observation of the water height in the duct; since water height is analogous to the gas pressure, the water height permits a qualitative comparison with the gas flow tests. These water table and gas flow experiments are described in the next section.

SECTION V

EXPERIMENTS

Water Table Experiments

As noted earlier, there exists a qualitative analogy between gas flow and water flow. Therefore, an experiment was performed on the Air Force Institute of Technology water table for comparison with supersonic gas flow energy addition tests. These experiments qualitatively confirmed the phenomena observed in the gas flow experiments. If the nozzle is attached to the duct, heat addition or mass addition causes a pressure rise or a water level rise which can feed upstream in the subsonic portion of the boundary layer into the nozzle, thus changing the initial conditions, see Figures (36), (37), and (38). If the duct is detached from the nozzle, the pressure rise feeds upstream in the subsonic boundary affecting the inlet shock and causes mass spillage, see Figures (39), (40), and (41). The effect of friction is visible in Figures (42) and (43) where the length of the duct walls are increased (no mass addition in the duct) to allow for a significant friction increase. The effect of friction is similar to mass or heat addition; a rise in pressure or water level occurs which can be transmitted upstream through the subsonic boundary layer.

For a small mass flow injection there was a small but continuous rise in water level or pressure as one would expect in an ideal weak

AD-A032 389 AIR FORCE AERO PROPULSION LAB WRIGHT-PATTERSON AFB OHIO F/G 20/4
HEAT ADDITION TO A SUPERSONIC FLOW.(U)
OCT 76 W C BURSON

UNCLASSIFIED AFAPL-TR-76-57 NL

2 OF 2
ADA032389

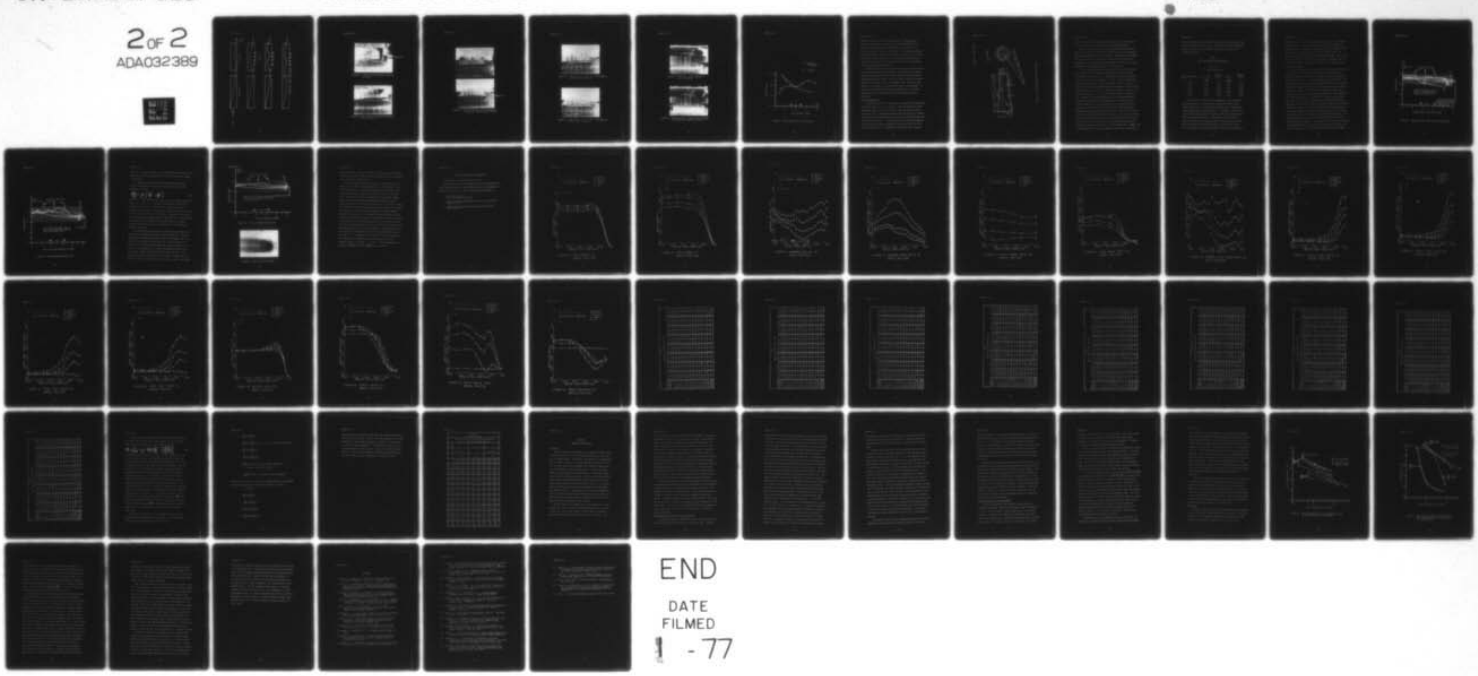

END

DATE
FILMED
1 -77

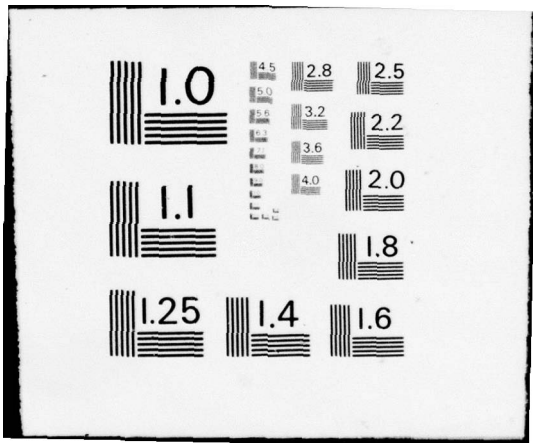
1.0
1.1
1.25
1.4
1.6
1.8
2.0
2.2
2.5
2.8
3.2
3.6
4.0
4.5
5.0
5.6

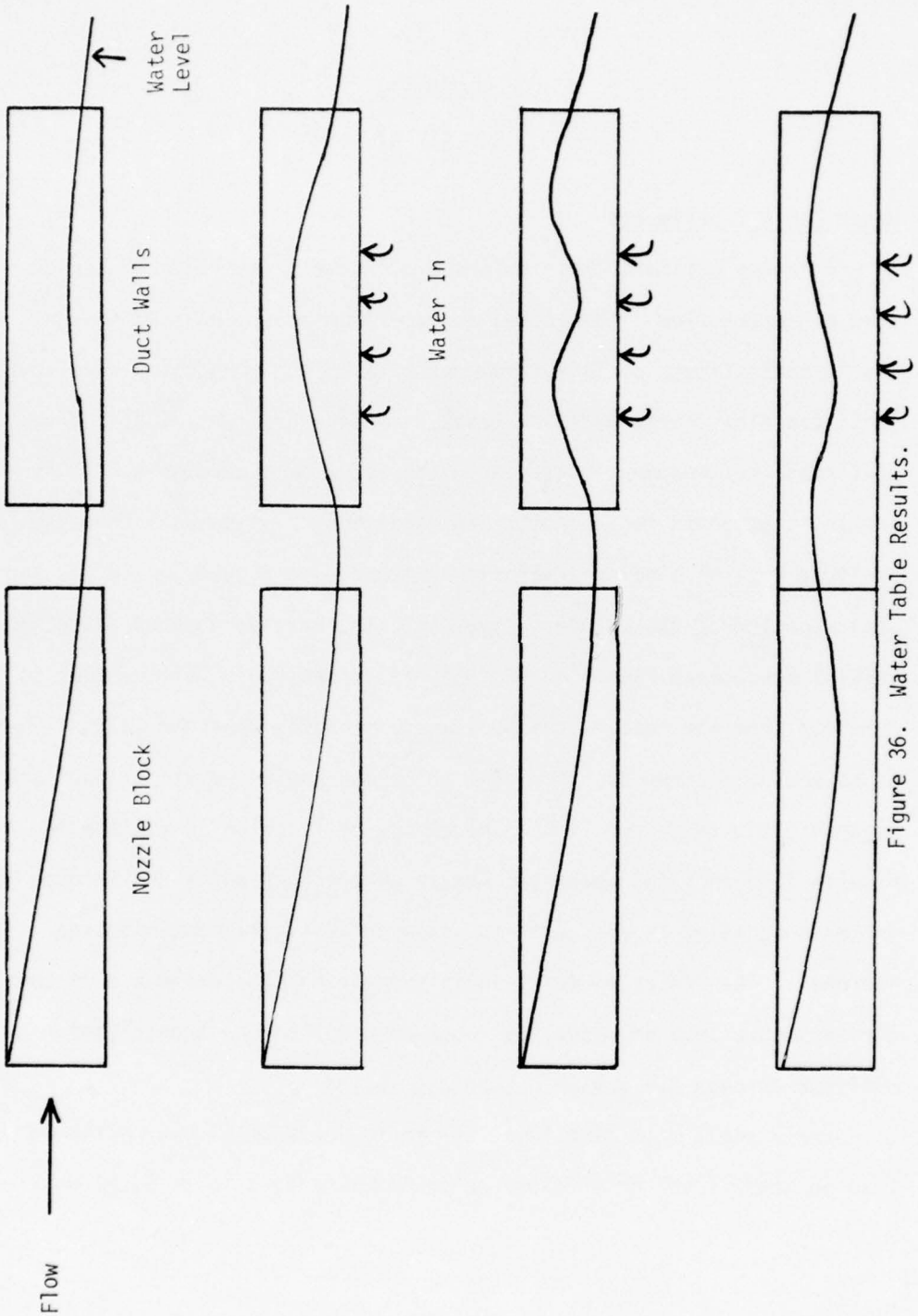

Figure 36. Water Table Results.

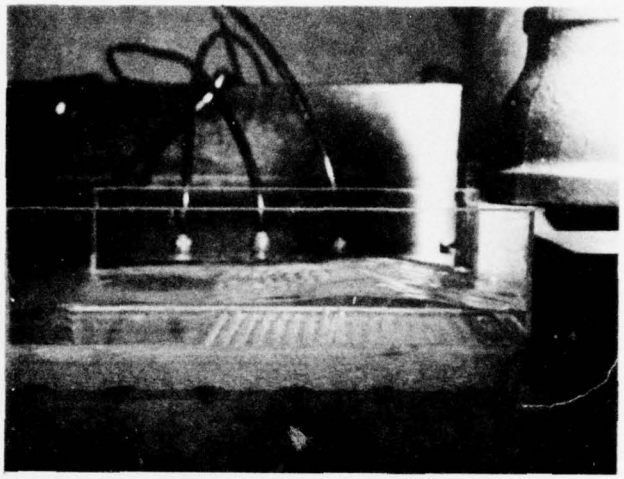

Figure 37. Side View of Duct Directly Connected to Nozzle.

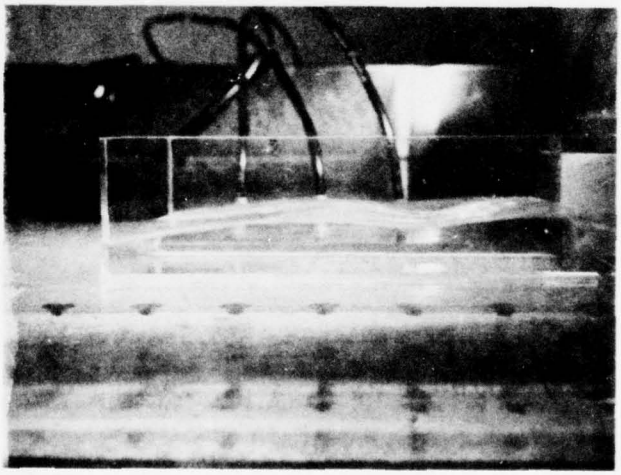

Figure 38. Mass Addition or Heat Addition Greater Than in Figure 37.

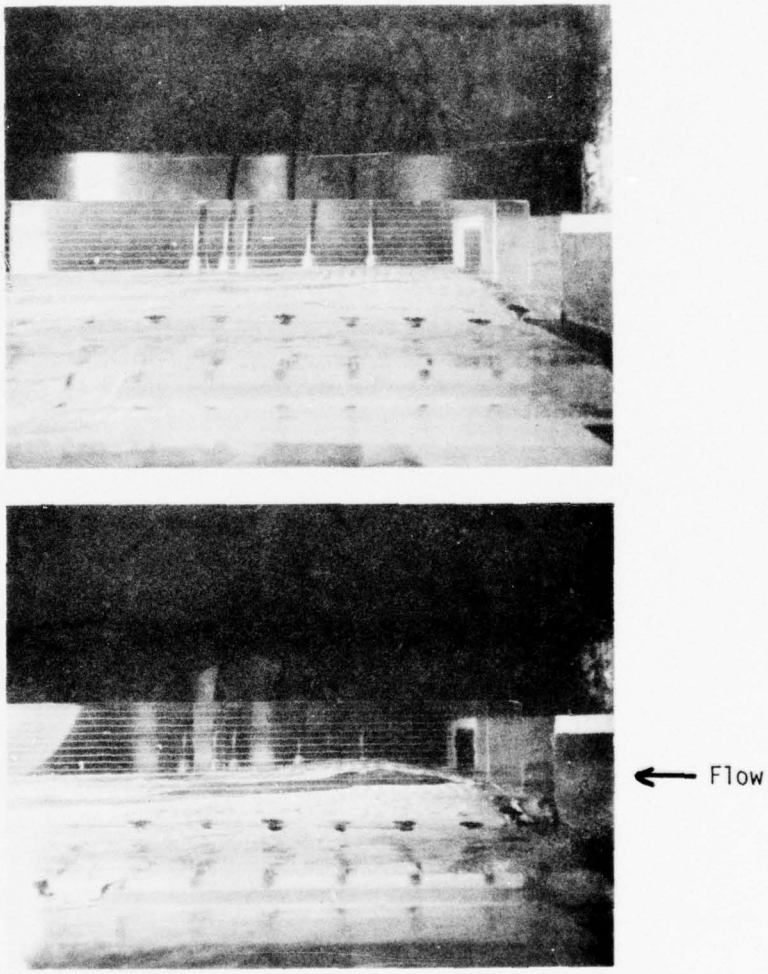

Figure 39. Side View of Free Inlet Duct Without and With Mass Addition (Heat) Addition.

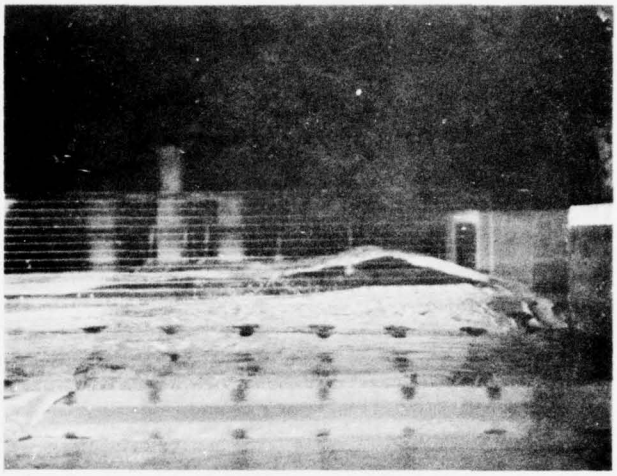

Figure 40. Side View of Free Inlet Duct. Mass Addition Greater Than in Figure 39.

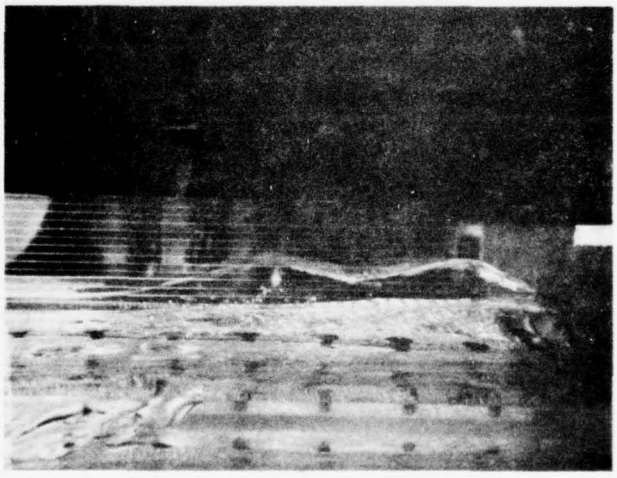

Figure 41. Side View of Free Inlet Duct. Mass Addition Greater Than in Figure 40.

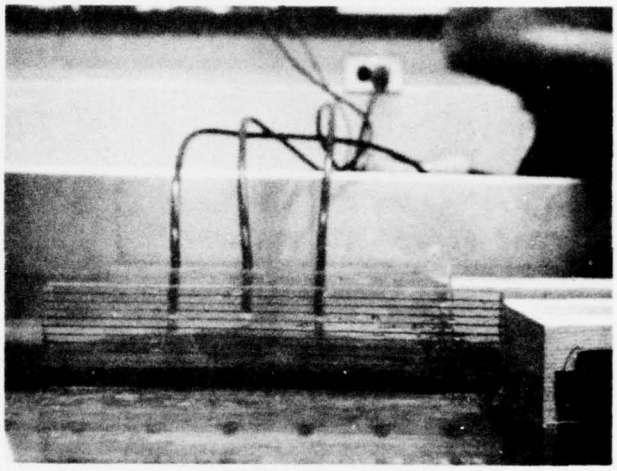

Figure 42. Side View. No Mass Addition and Ink in Water.

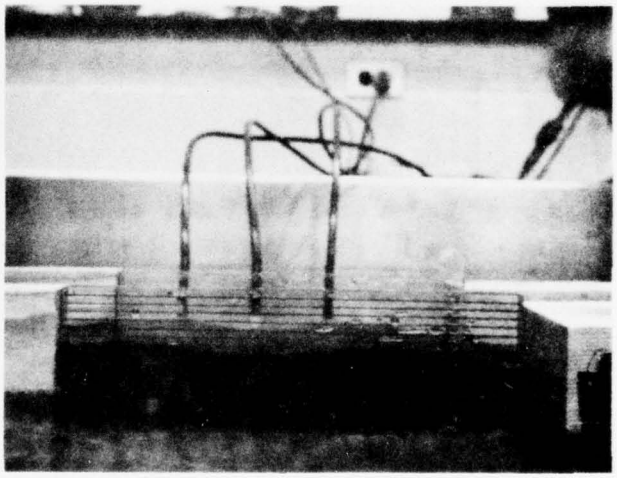

Figure 43. No Mass Addition. Length of Duct Extended, Illustrating the Effect of Friction.

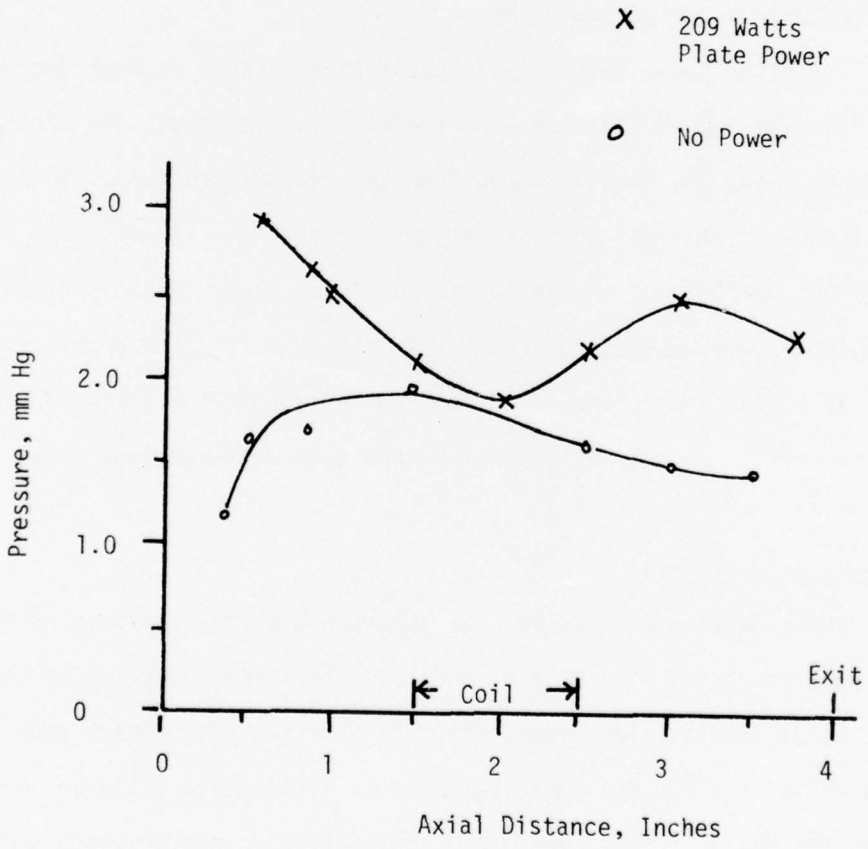

Figure 44. Static Pressure vs. Axial Position

detonation; but, with increasing mass injection, compression and expansion regions occur in the water duct as was observed in one of the initial gas flow tests, see Figures (38), (41), and (44). In most cases observed in gas flow experiments, there existed a pressure rise and decrease in the duct as in Figures (37) and (40). In all the water table pictures shown, the flow remained supersonic, which was verified by placing a pencil at various points in the duct and observing the Mach waves generated by it.

The water table gave a good qualitative picture of what occurred in the gas flow energy addition experiments. In both cases the pressure increase along the duct differed from the gradual continuous increase predicted by the ideal theory. As will be shown in the gas flow experiments this difference is due to the boundary layer. The water table facility is very useful in practically all types of flow problems. If available, it should be used to gain an insight into a flow problem before moving on to a more expensive and time-consuming gas flow experiment.

Gas Flow Experiments

Three ducts were used for the supersonic energy addition experiments having area ratios of 1.0, 1.6, and 2.0. They were operated at three heat input levels. See Figure (45) for a sketch of the duct with an area ratio of 2.0. Pressure measurements were made axially and radially along the ducts; total temperature and ionization measurements were made radially at the duct exit. The temperature and ionization measurements were limited to the duct exit because an insertion of about 1/2-inch into the duct led to R.F. interference on the probe output rendering

Material: Boron Nitride

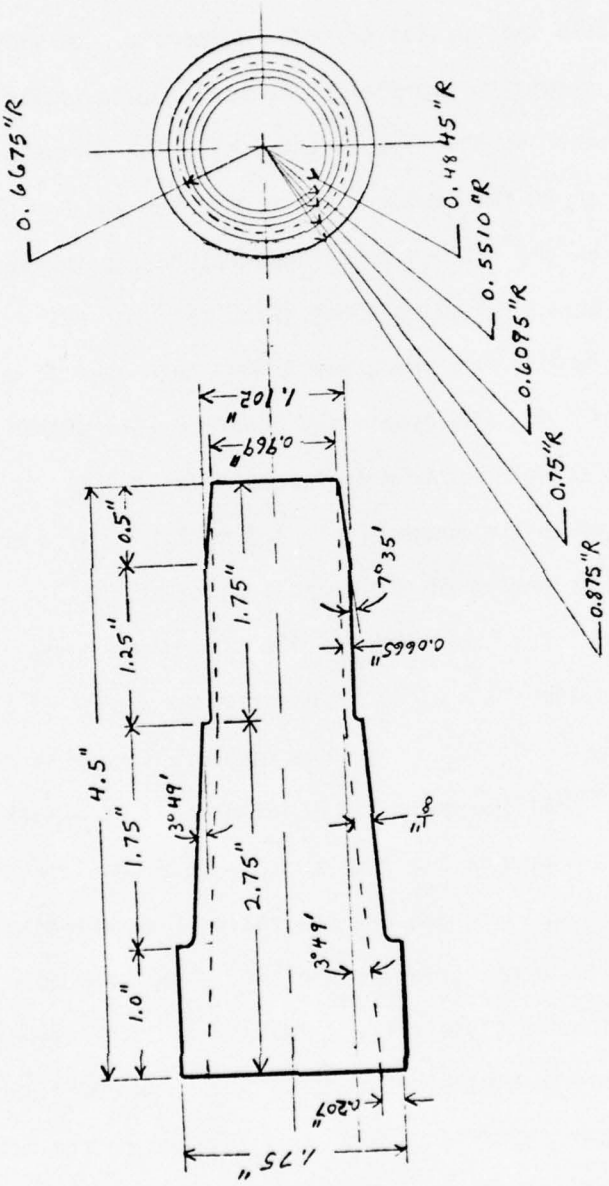

Figure 45. Varying Area Duct for Heat Addition.

useless information; in addition, the diameter of the double probe was too large for insertion without seriously disturbing the flow.

Table 1 shows the results of total temperature measurements made with the total temperature probe for several nozzle chamber temperatures. No energy was added to the flow in the duct. The nozzle chamber temperature was measured on the center line as were the duct inlet and exit measurements. As the chamber total temperature was increased, the probe measurement error decreased to about 2% at the duct exit.

The total temperature probe had a vent hole area to entrance area ratio (A_v/A_e) of 0.27. Goldstein and Scherrer [21] showed that the shielded probe recover factor r is insensitive to A_v/A_e in the range of 0.2 to 0.8. Also in the range of M = 1.3 to 2.1 r was a constant value and insensitive to angles of probe inclination up to 10°. Eber [22] shows a shielded total temperature probe with bleed holes (similar to the one used in this effort) that is insensitive to angles of attack of $\pm$ 10°; and, in the range of M = 1 to 3.0, the recovery factor is constant at 0.95. Bontrager [23] determined that for a ratio of entrance length (distance from entrance to the thermocouple in a shielded probe) to internal diameter equal to one and the ratio of an effective friction length to entrance length greater than one, then the measured total temperature approaches closely the actual value. The effective friction length is that length equivalent to a 45°, 90°, or 180° turn in the flow. Le/L for the present work was $\approx$ 60. Hence, based on the data in Table 1 and the results of the above authors, the total temperature measured should be accurate within at least $\approx$ 5% of the actual value. However, due to the recombination of ions and electrons in the probe, the measured

value must be corrected for recombination energy as was discussed in the double probe analysis given earlier. The error due to this recombination energy correction is more significant than the error in the total temperature reading.

TABLE 1

TOTAL TEMPERATURE PROBE MEASUREMENTS

$M_1 = 3.1$

T^o - Measured by Probe

T^o_{ℓ} Nozzle Chamber °R	Duct Inlet T^o/T^o_{ℓ}	Recovery Factor r	Duct Exit T^o/T^o_{ℓ}	Recovery Factor r
534.5	0.982	0.975	0.974	0.966
550.5	0.991	0.984	0.979	0.974
560.0	0.995	0.993	0.982	0.979
580.0	1.000	1.000	0.981	0.977

Initial static and total pressure measurements, using the probes discussed earlier, in a diverging duct attached to a Mach 5 nozzle showed large errors in calculated total pressure which increased with increasing Mach number along the duct axis. Therefore, a Mach 3.5 nozzle was fabricated along with a constant area duct with three pressure wall taps spaced one inch apart. The purpose of this duct was to observe the effect of the pressure probes as they moved down the duct. While the probe was moving down the duct, the pressures at the wall taps were recorded. No energy was added to the duct during these runs.

Figure (46) shows the effect of the conical tipped static pressure probe at the wall taps. Figure (47) shows the effect of a flat nosed total probe which has a considerable upstream influence on the flow due to the strong shock at the nose interacting with the boundary layer. The conical tipped static probe had a small upstream influence. Thus it was decided to fabricate a total pressure probe with a truncated conical tip to reduce the upstream influence of the probe which introduces errors into the calculations.

The first truncated conical tip for the total pressure probe was 0.3 inches long and had a base of 0.08" diameter through which a 0.013" diameter hole was drilled which was followed by a 0.025" diameter hole that fed into the 0.05" I.D. of the ceramic tube, see Figure (24). This probe reduced the upstream pressure influence significantly, as shown in Figure (48). However, when the measured total pressure was converted to actual total pressure, the result was consistently low, whereas the blunt-nosed probe gave results that were generally high when compared to the chamber total pressure. Checking the literature on total probes, [24], [25], it was found that, according to the presented curves, the dimensions of the tip hole diameter and outside diameter of the probe and the Reynolds number were such that the probe should give good results. It was then decided to double the hole diameter to 0.026" all the way through the conical tip, keeping the outside dimensions the same. This correction brought the calculated total pressure much closer to the nozzle chamber total pressure. The maximum errors which occur in regions of rapid (with respect to axial position) pressure variation were -20% and +15% compared to -50% and +200% for the blunt-nosed total probe. In

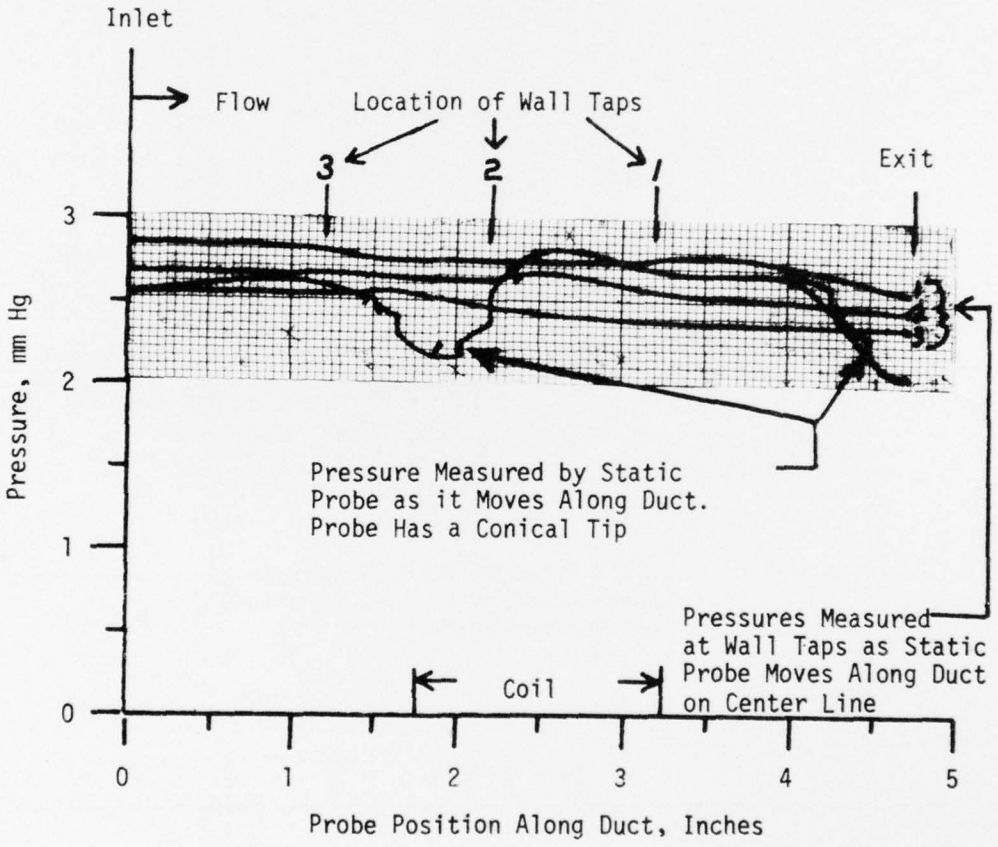

Figure 46. Pressure for Wall Taps & Static Pressure Probe.

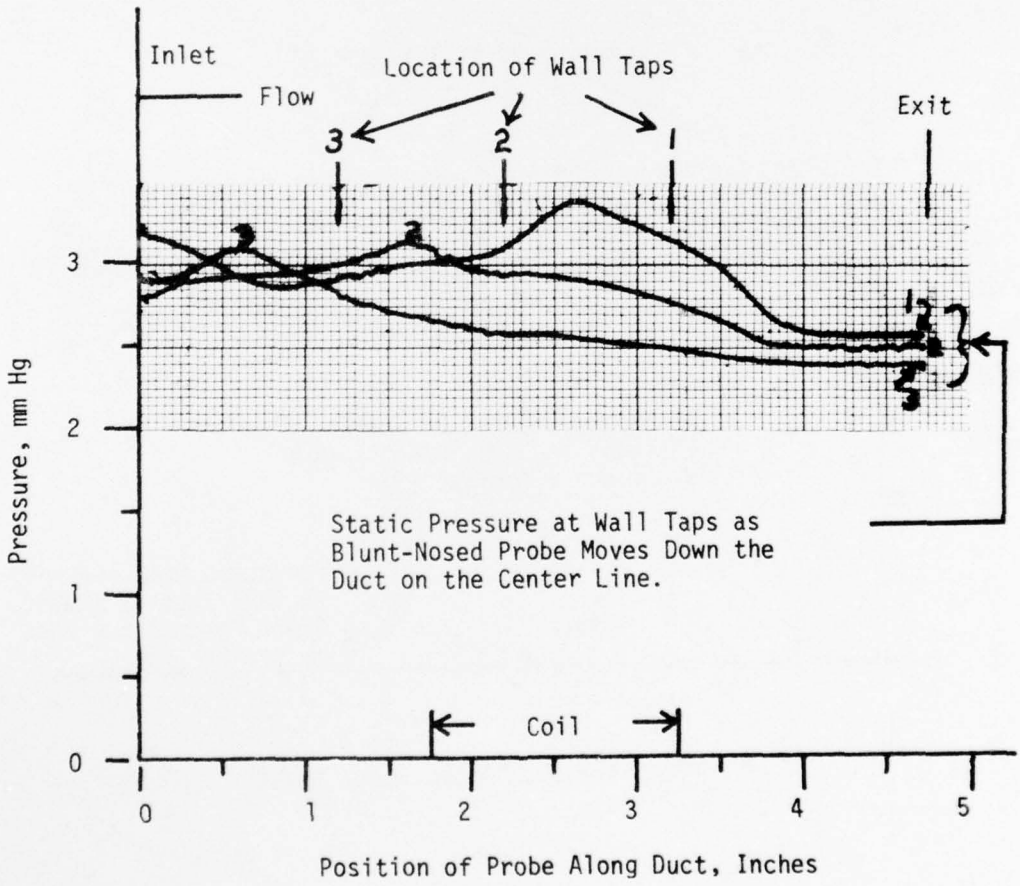

Figure 47. Pressure Measured by Wall Taps.

regions of slow (with respect to axial position) pressure variation, the calculated total pressure ranged from -6% to +6% of the nozzle chamber total pressure.

To illustrate the difficulty of determining the actual total pressure from measured total and static pressure, we can write the differential equation:

$$\frac{dP^{\circ}_{ACT}}{P^{\circ}_{ACT}} = \frac{\gamma}{\gamma-1}\left[\frac{dP^{\circ}}{P^{\circ}} - \frac{dP}{\gamma P}\right] \qquad (125)$$

where P & P_0 is the measured static and total pressure behind the probe shock wave. Since γ/γ-1 = 2.5, then the combination of the errors in measured total and static pressure can cause significant errors in calculated total pressure. For example, a 5% error in P^{O} and a -5% error in P will result in an error of 20% in P^{O}_{ACT}. Comparing the static pressure as measured by the probe with that of the wall taps, it was observed that probe and wall tap agreed within a percent when in a region of relatively slow pressure variation and the holes of the probe were in line with the wall tap.

Using the probes and three ducts discussed above, measurements were made for zero power and three power settings for each duct. Pressure measurements were made axially along the duct at the center line, 0.19R, 0.38R, 0.57R, and 0.76R from the center line. These pressures were recorded on an X-Y plotter continuously and a digital printout every 1/4 inch. The total temperature and ionization measurements were made at 11 positions radially from the center line at the duct exit. These measurements were also recorded on an X-Y plotter. The probes moved at about 0.01 inches per second; but, even at this slow speed a few seconds'

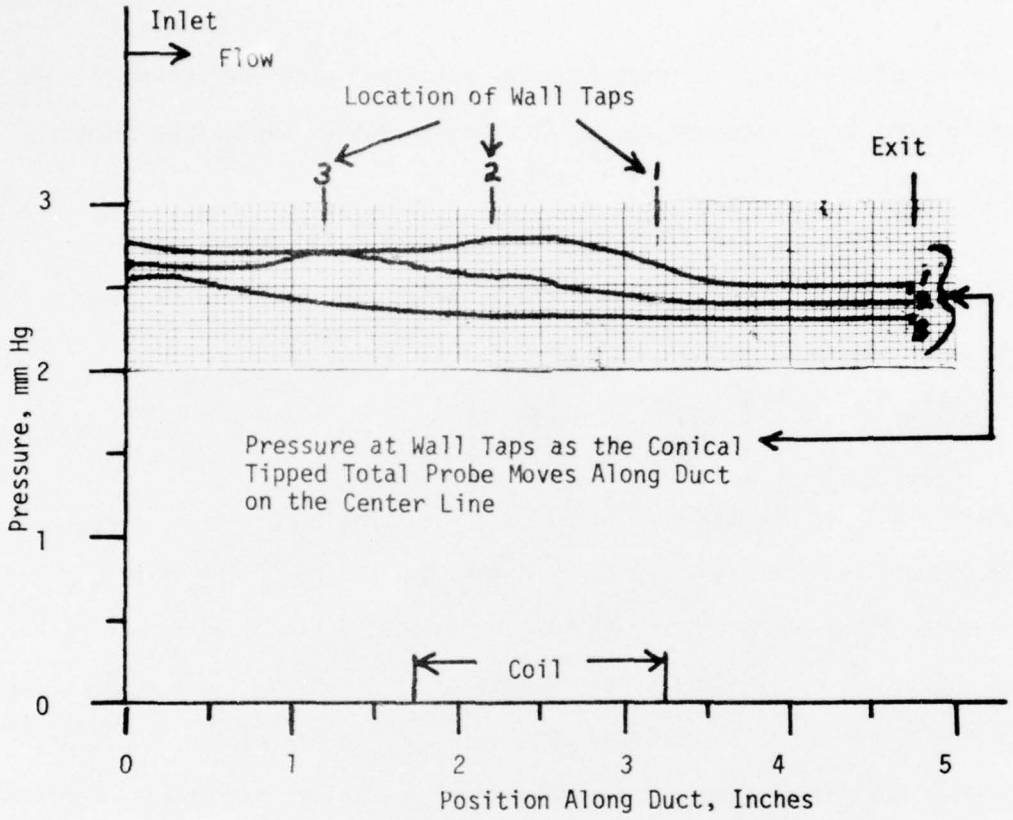

Figure 48. Pressure Measured by Wall Taps.

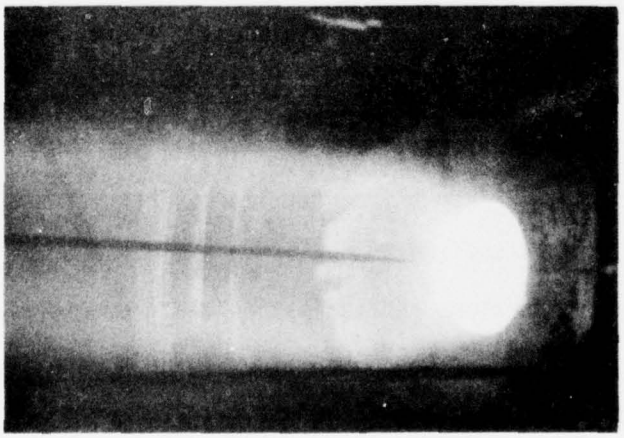

Figure 49. Probes at Exit of the Duct.

pause was necessary at each 1/4" interval to allow the static pressure to reach equilibrium. Figure (49) shows the probes in the jet downstream of the duct during a power-on run.

A computer program was utilized to analyze the data and to plot properties vs. radius or average properties vs. axial position. Equations (polynomials) as a function of radius were developed to satisfy the data points and the boundary conditions at the duct's center and wall. These equations listed as subroutines in the computer program could then be utilized to determine averages by integration and be called by the plot routine to develop the radial or axial plots. Figures (50) through (64) show the experimental results for the 2° 24' half-angle diverging duct. Tables 2 through 10 compare the calculated average properties of the data for all three ducts with the analytical program based on average properties, which was discussed in Section I. The input for the theoretical program was the average initial and final Mach numbers from the experimental data taken at inlet and exit of the duct; then other parameters were calculated for comparison. Average properties for the data were calculated two ways; one was integrated by RdR and divided by $R^2/2$, or, if a parameter is a function of two or more variables, an average value was obtained by using the average value of each variable involved; for example, $\rho = \langle P \rangle / R \langle T \rangle$. For the temperature, an average by $\int_0^R T\dot{m}RdT$ divided by $\int_0^R \dot{m}RdT$ was also made.

NOTES FOR FIGURES (50) THROUGH (64)

Curves are for a duct with area ratio of 1.6.

Total pressure and total temperature ratios are referenced to the nozzle chamber conditions. Other parameter ratios are referenced to the value at the duct inlet center line before energy addition.

α → degree of ionization
(α = 0 unless noted otherwise)

I → refers to position along the duct inlet (1) to exit (20) in intervals of 1/4"

N → refers to power setting or energy input given by total temperature ratio

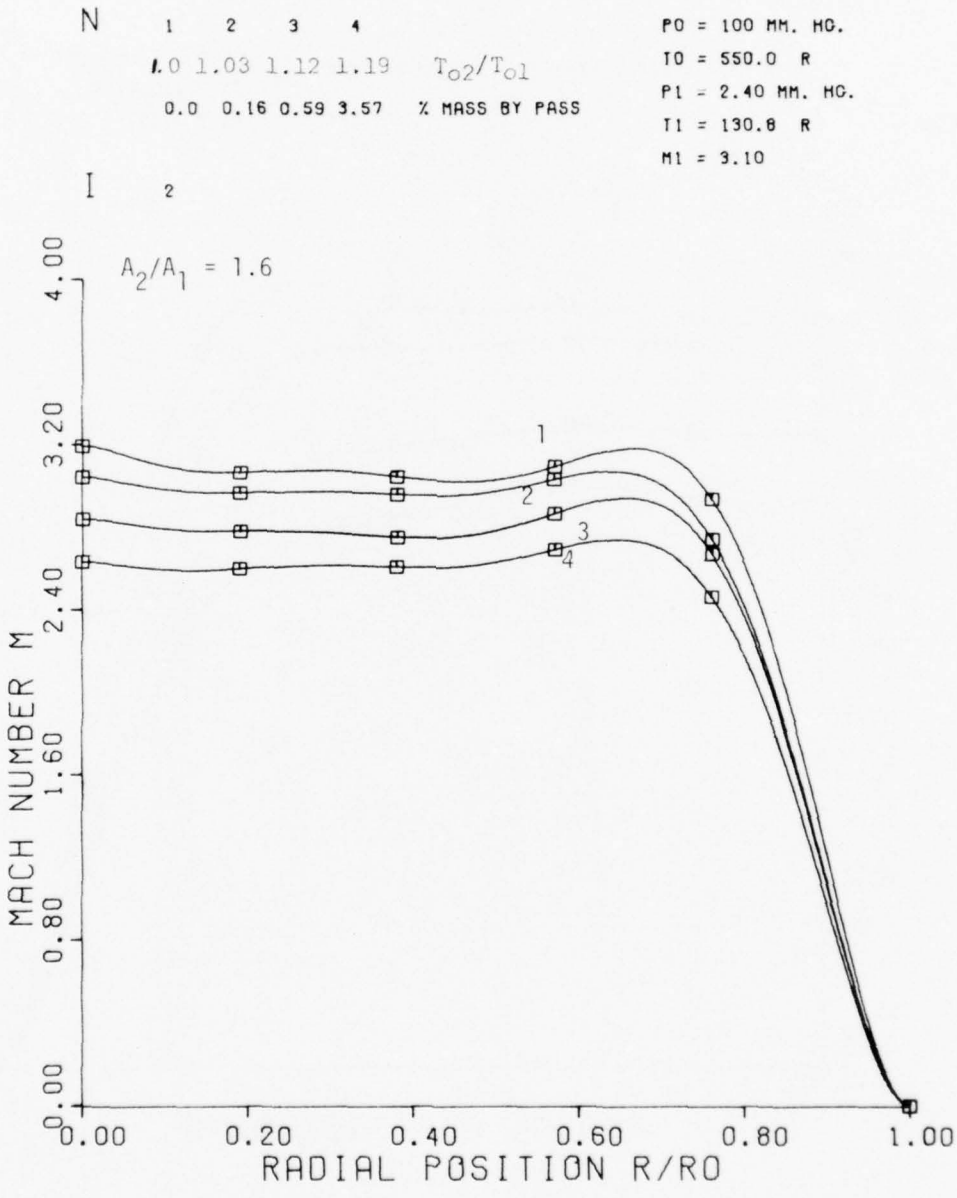

FIGURE 50 . MACH NUMBER VS. RADIAL POSITION

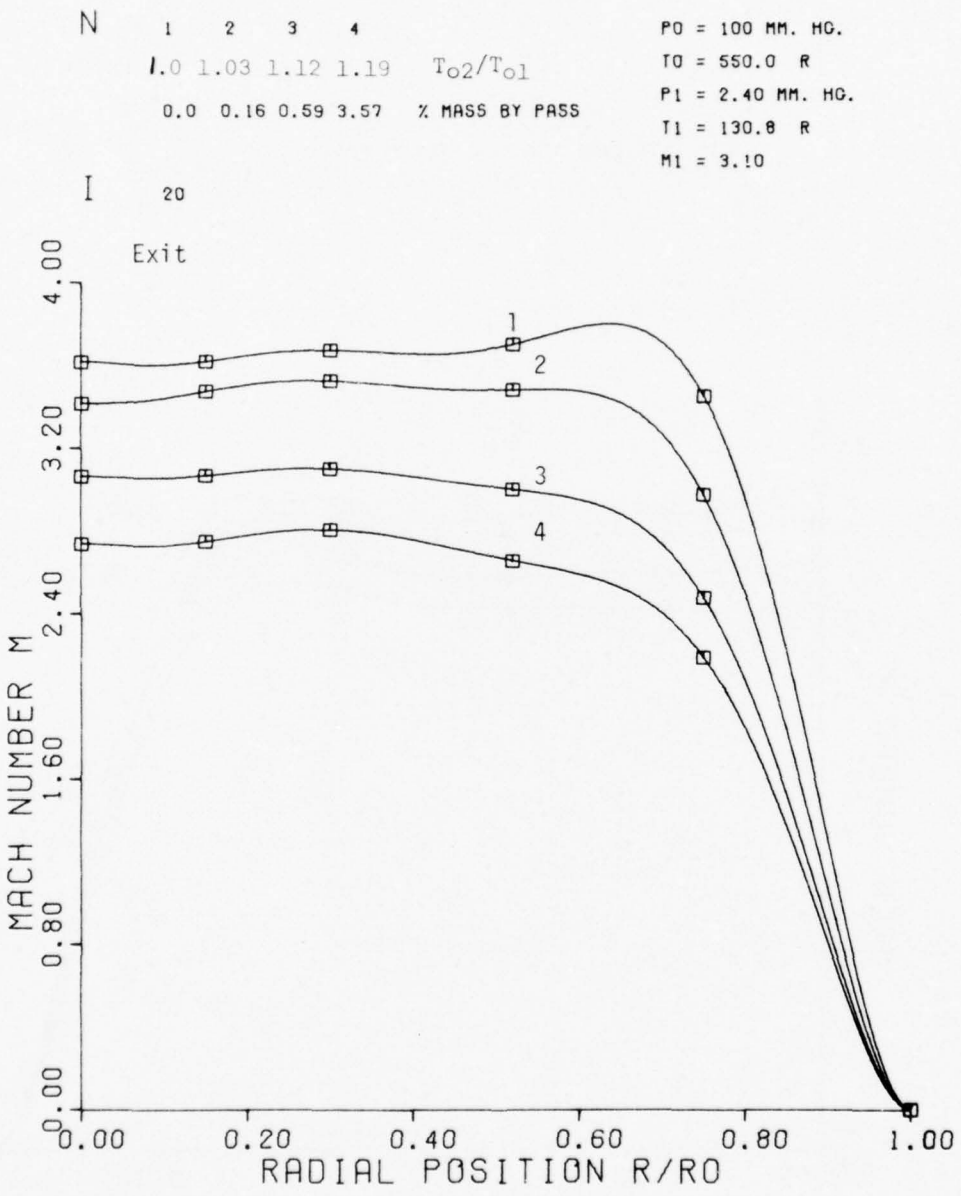

FIGURE 51. MACH NUMBER VS. RADIAL POSITION

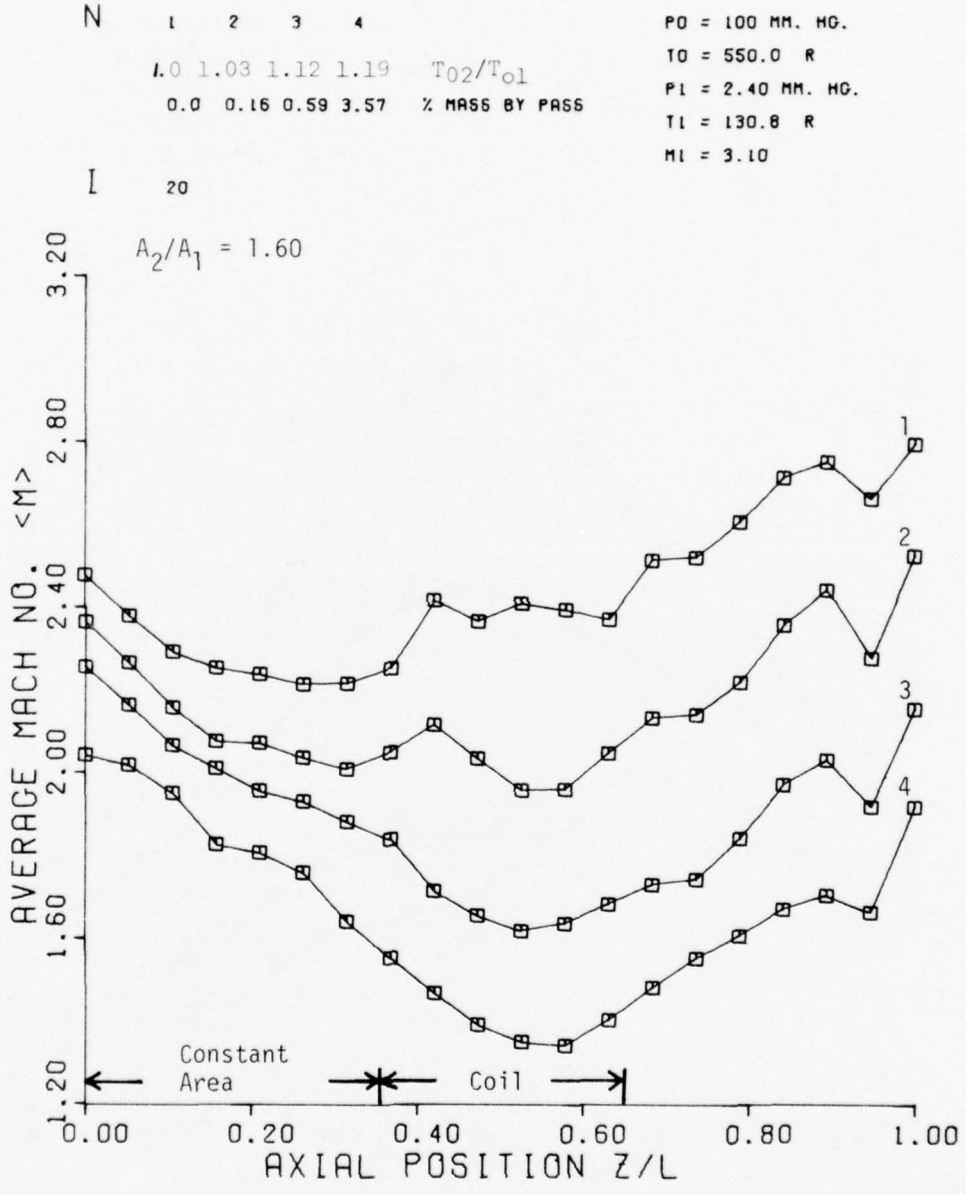

FIGURE 52 . AVERAGE MACH NO. VS. AXIAL POSITION

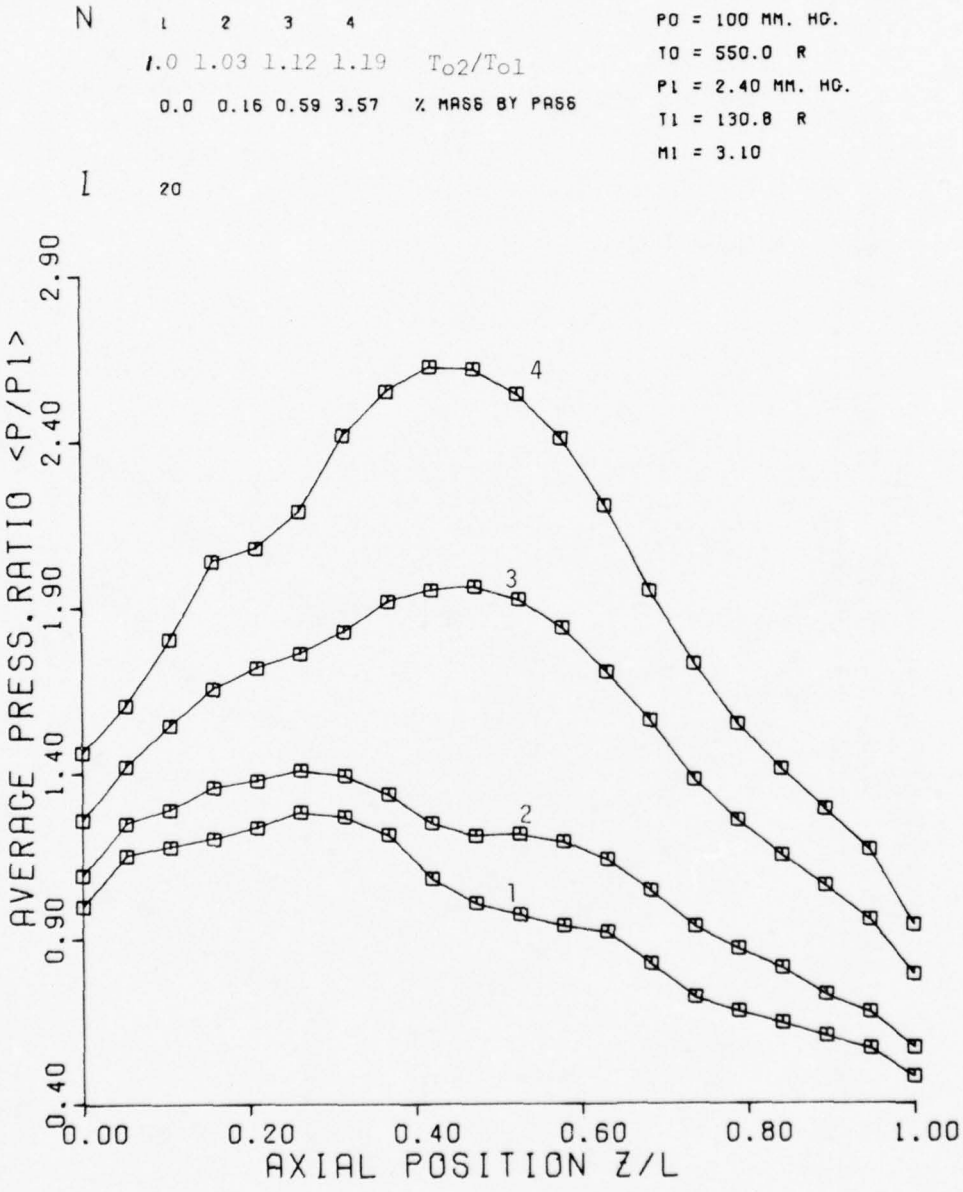

FIGURE 53. AVERAGE PRESS.RATIO VS. AXIAL POSITION

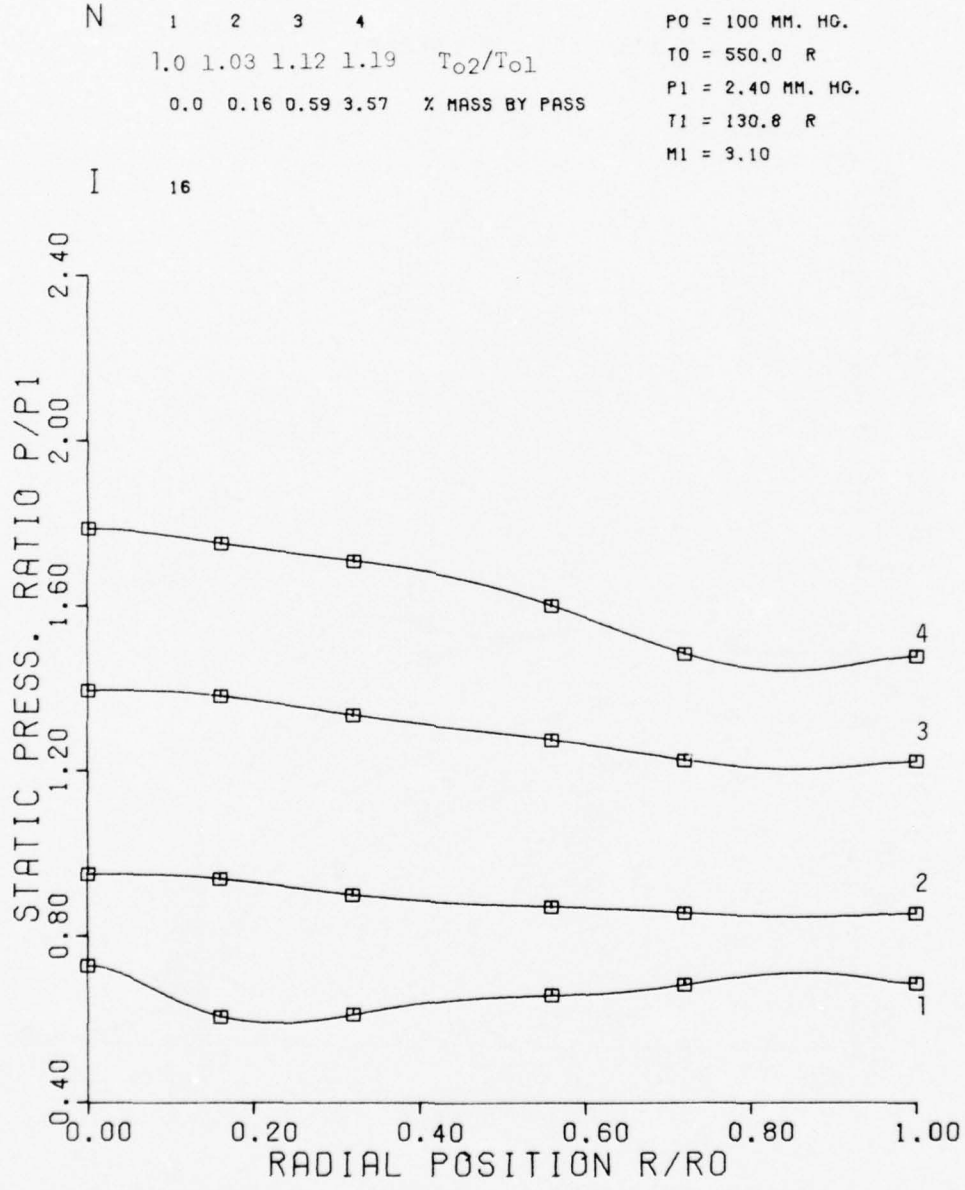

FIGURE 54. STATIC PRESS. RATIO VS. RADIAL POSITION

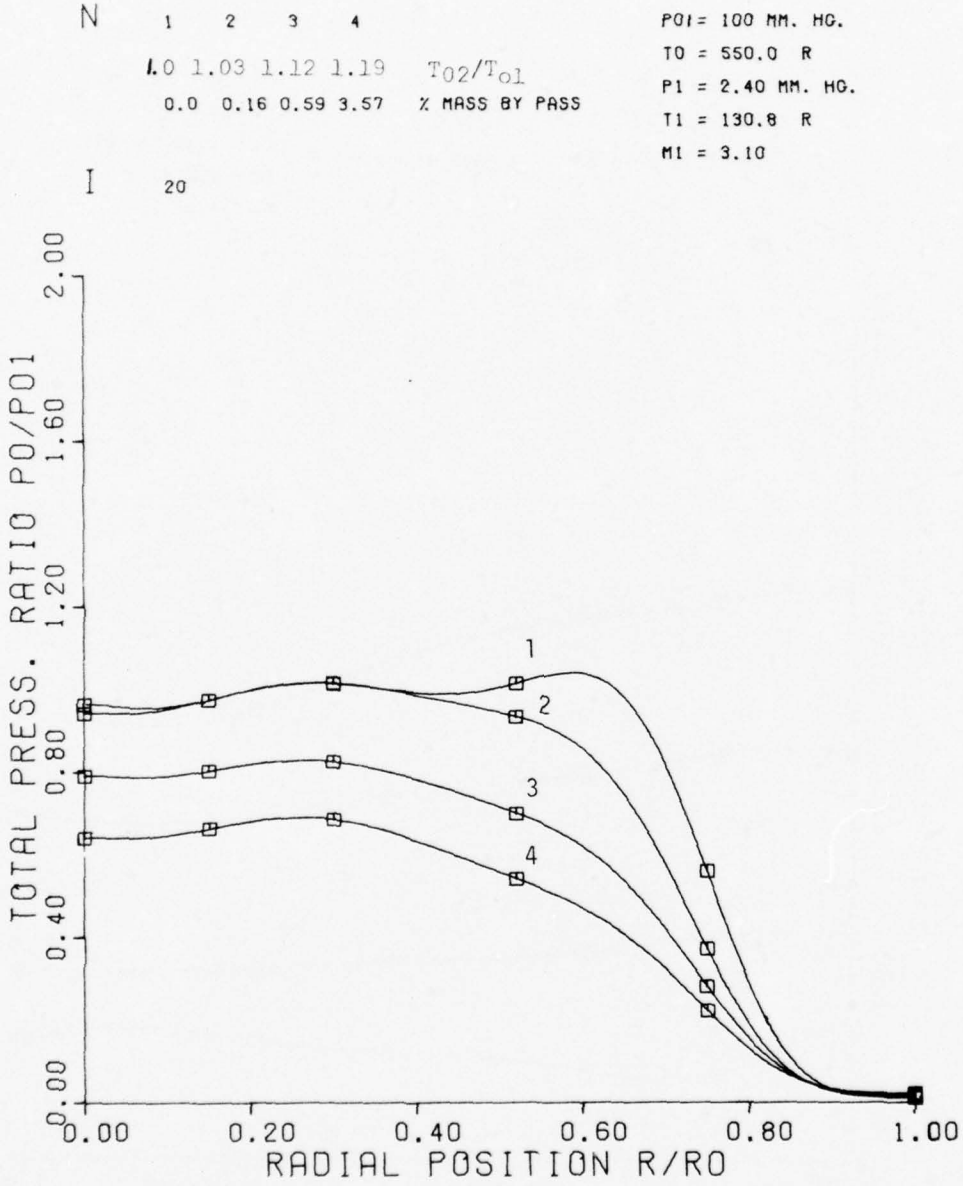

FIGURE 55 . TOTAL PRESS. RATIO VS. RADIAL POSITION

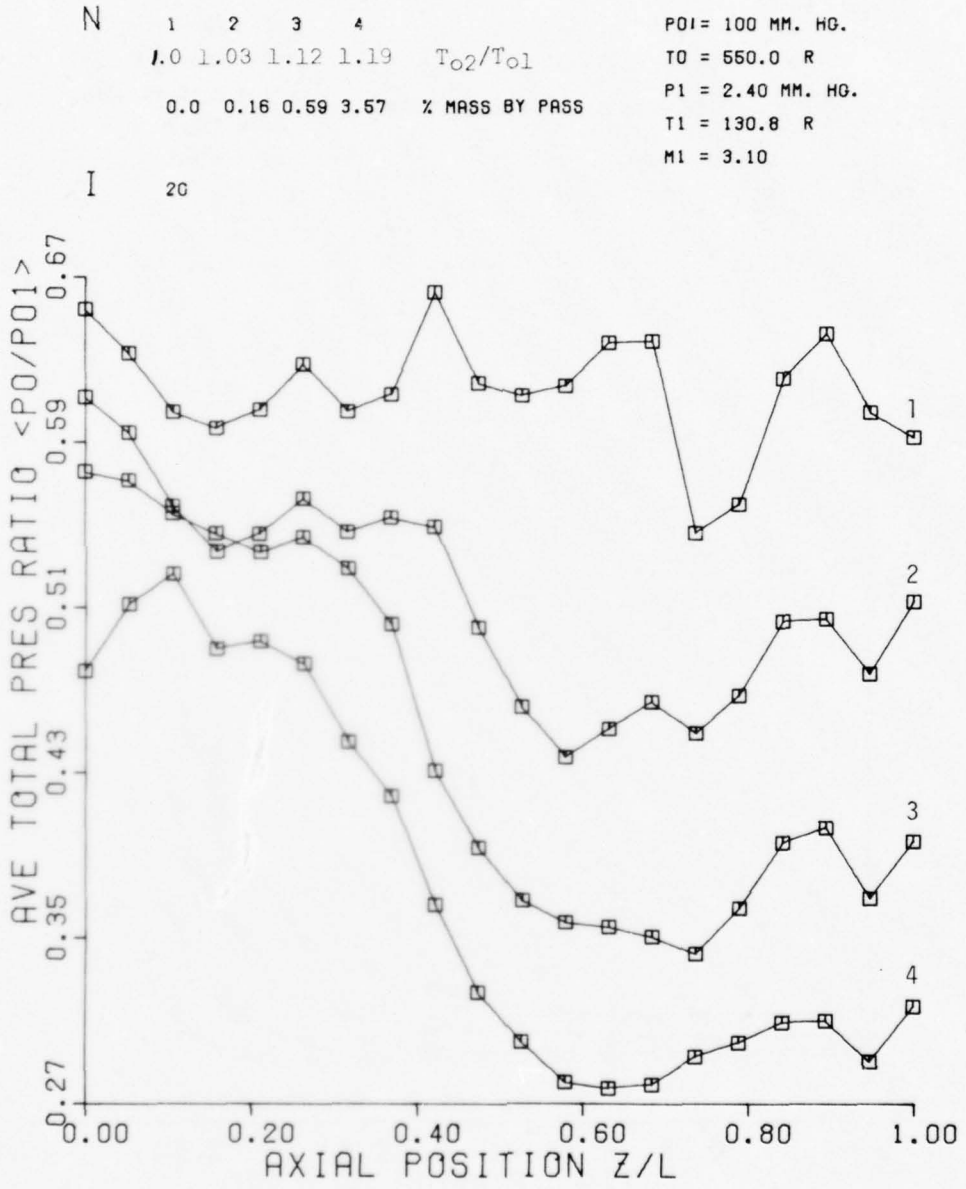

FIGURE 56. AVERAGE TOTAL PRESS RATIO VS. AXIAL POSITION

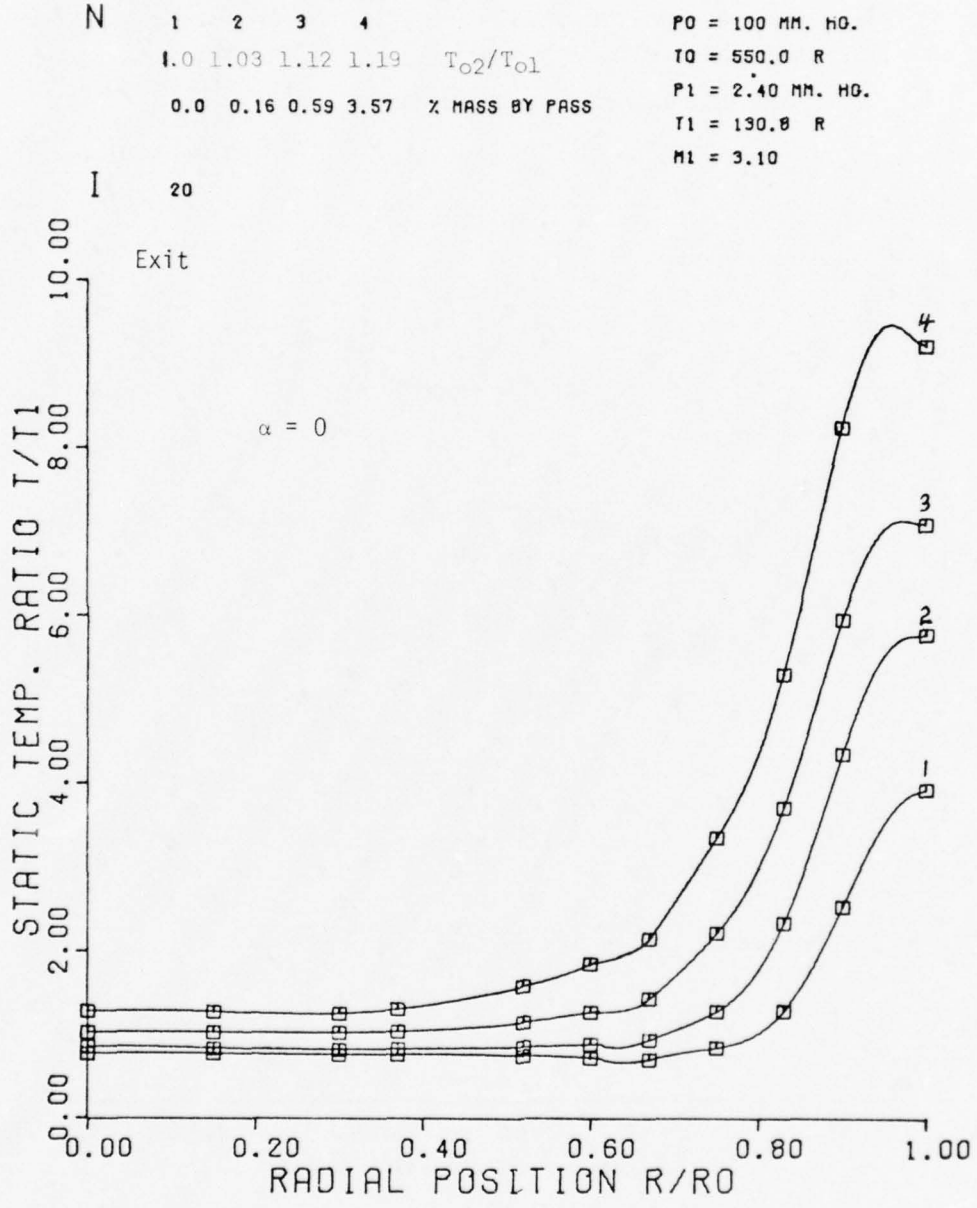

FIGURE 57. STATIC TEMP. RATIO VS. RADIAL POSITION

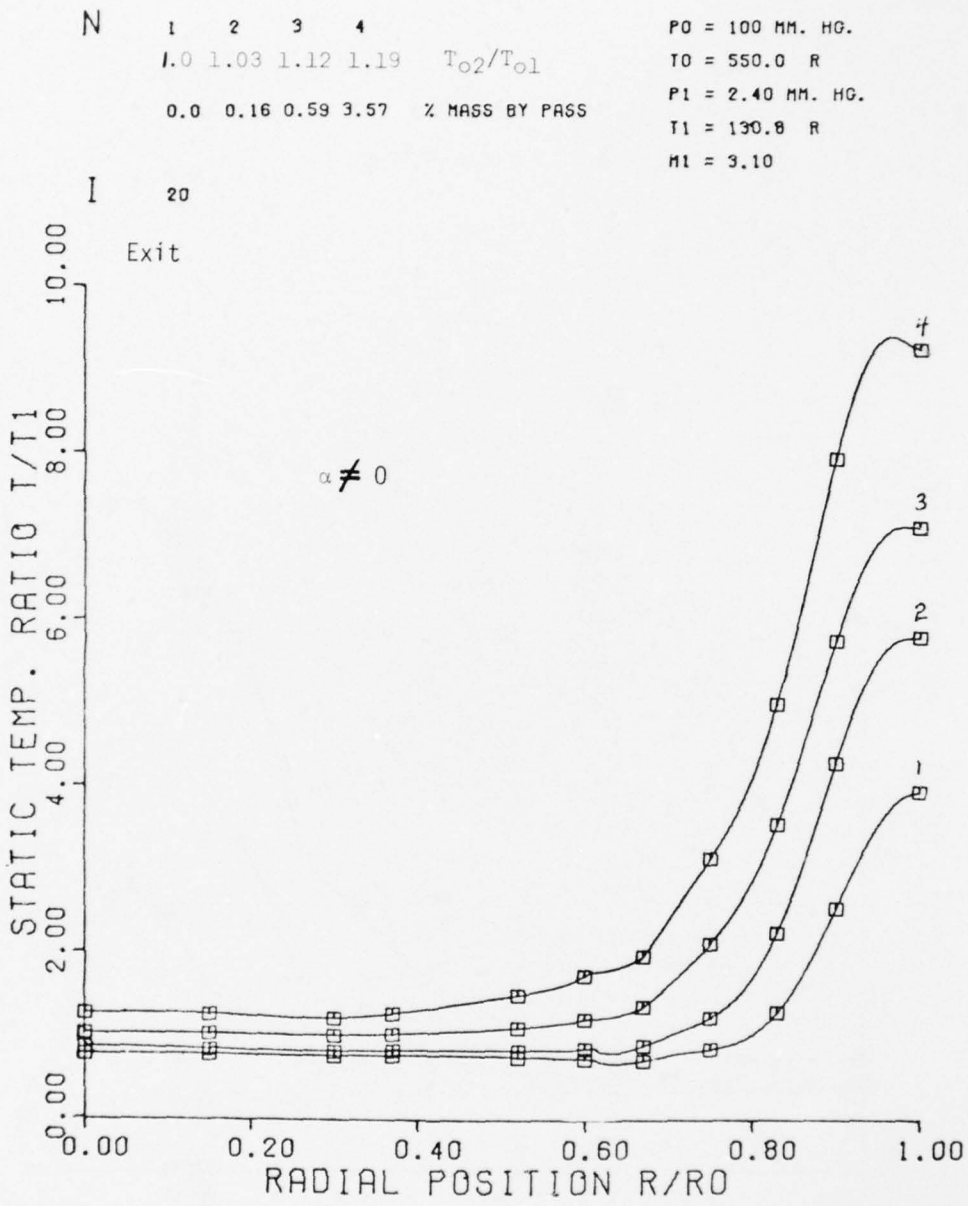

FIGURE 58 . STATIC TEMP. RATIO VS. RADIAL POSITION

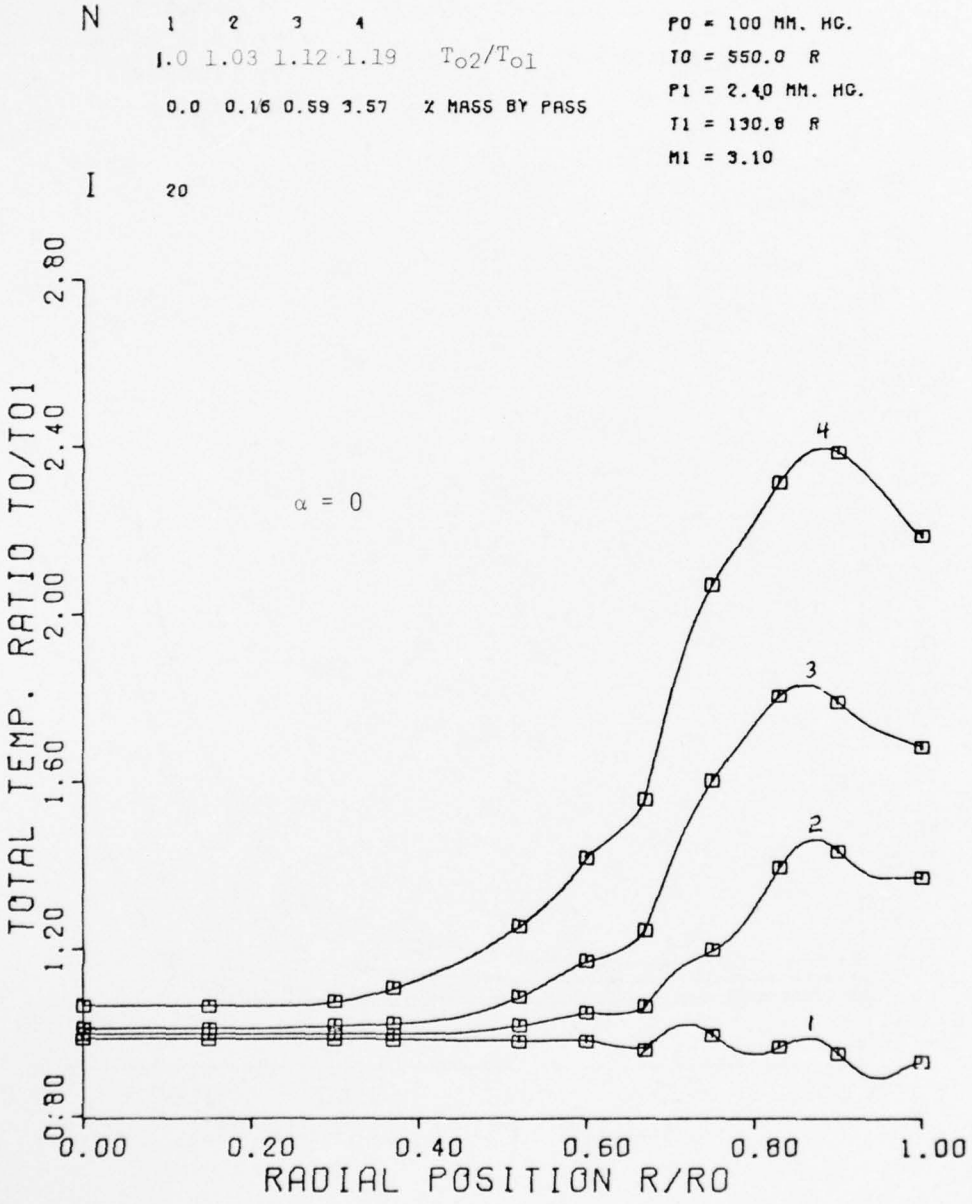

FIGURE 59. TOTAL TEMP. RATIO VS. RADIAL POSITION

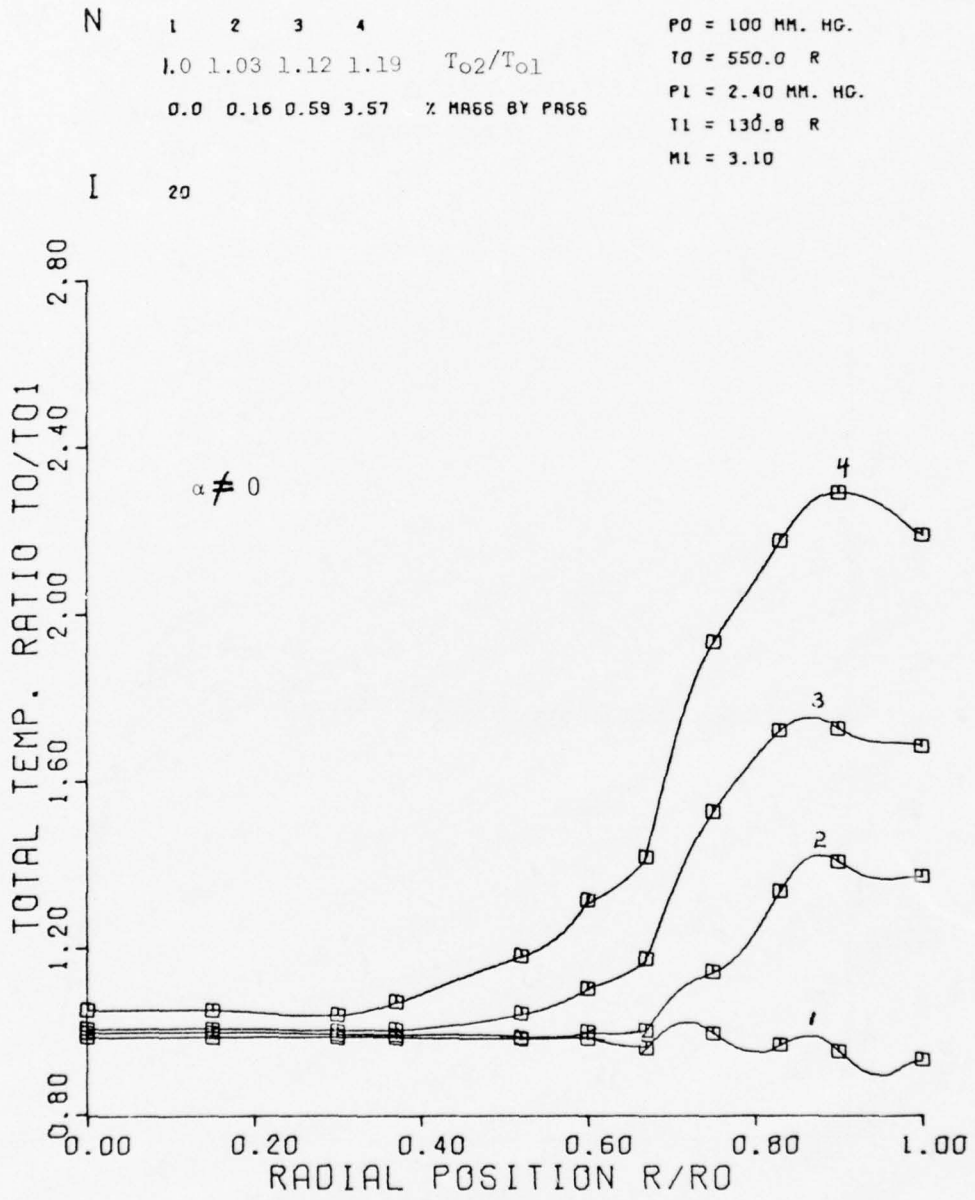

FIGURE 60 . TOTAL TEMP. RATIO VS. RADIAL POSITION

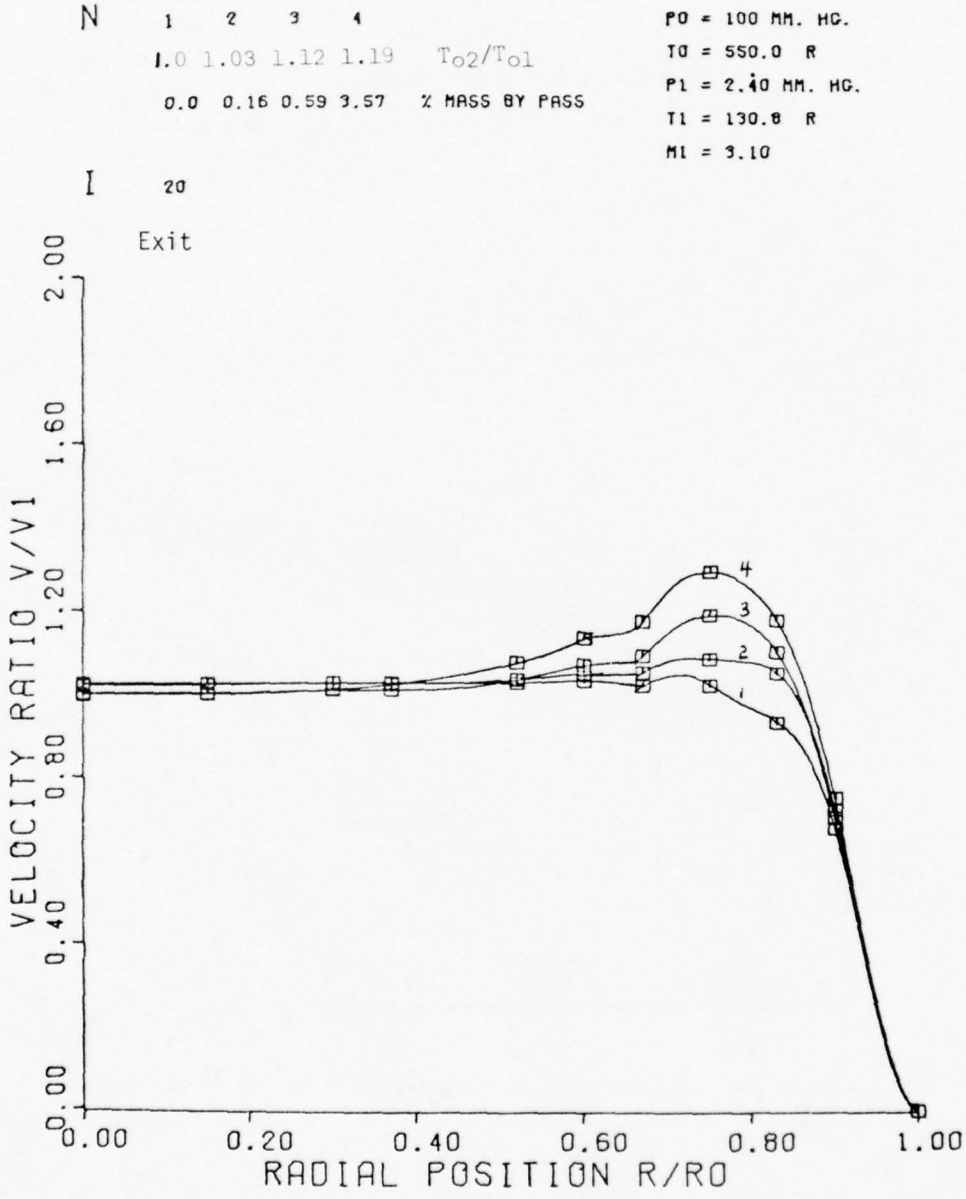

FIGURE 61. VELOCITY RATIO VS. RADIAL POSITION

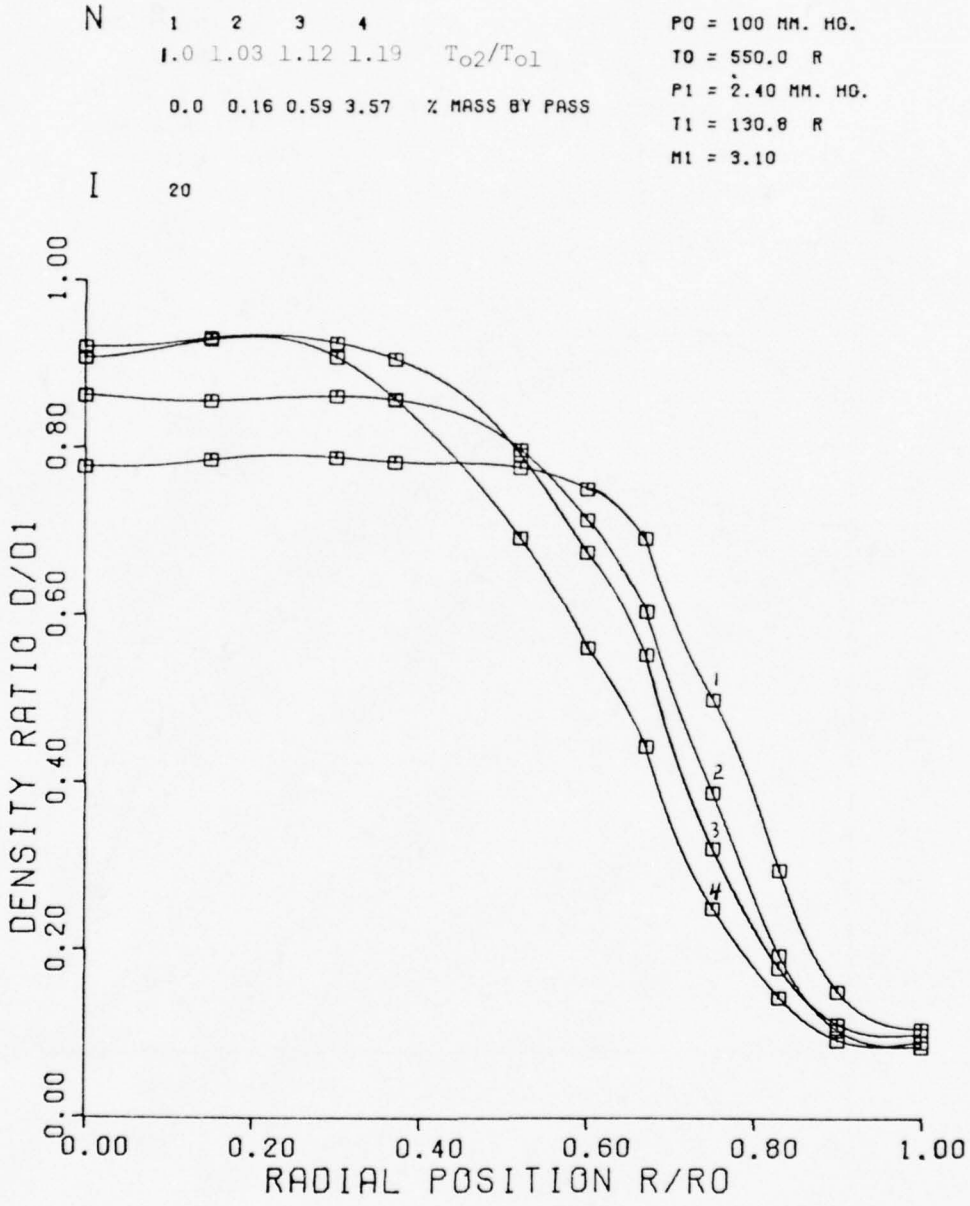

FIGURE 62 . DENSITY RATIO VS. RADIAL POSITION

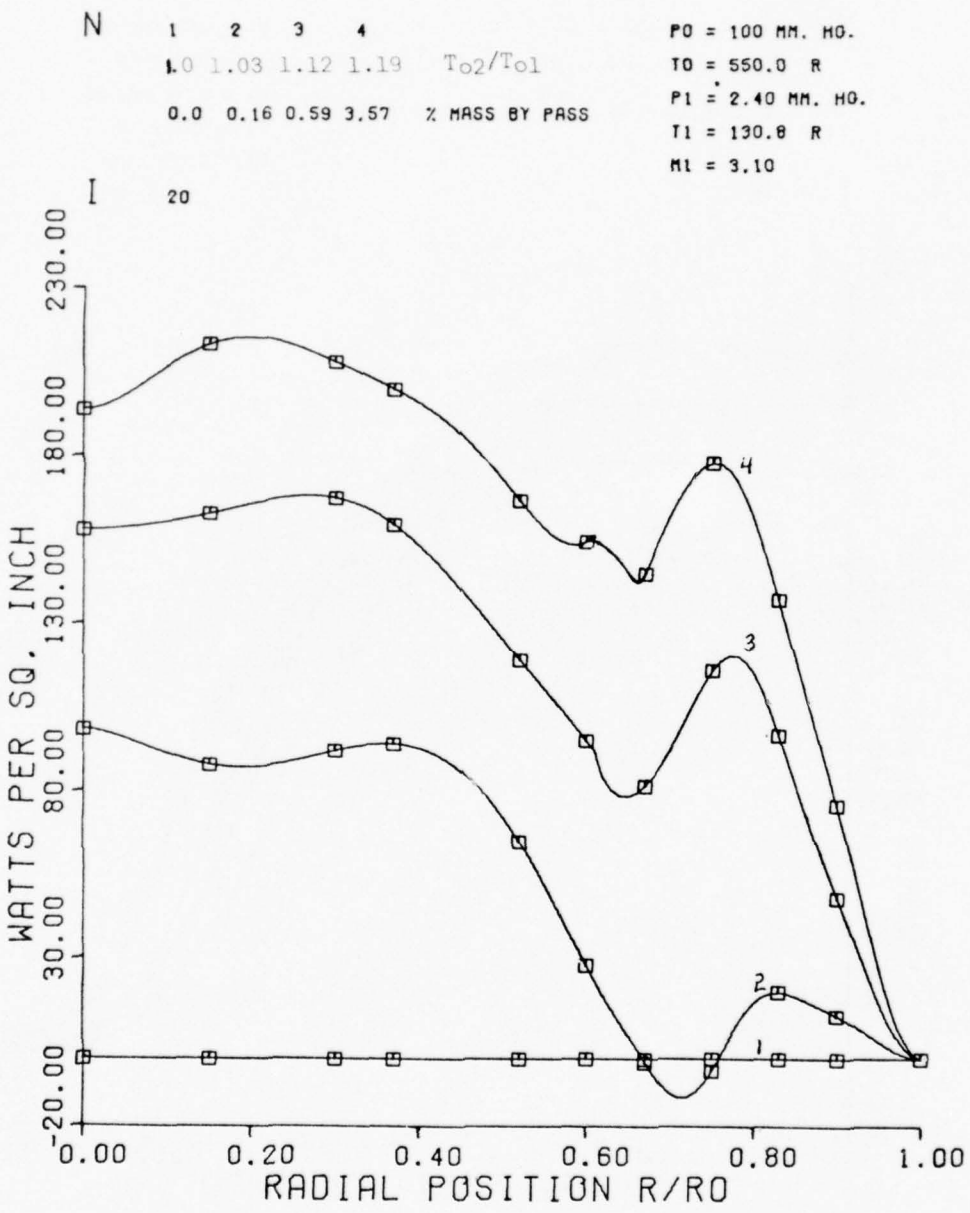

FIGURE 63. WATTS PER SQ. INCH RADIAL POSITION

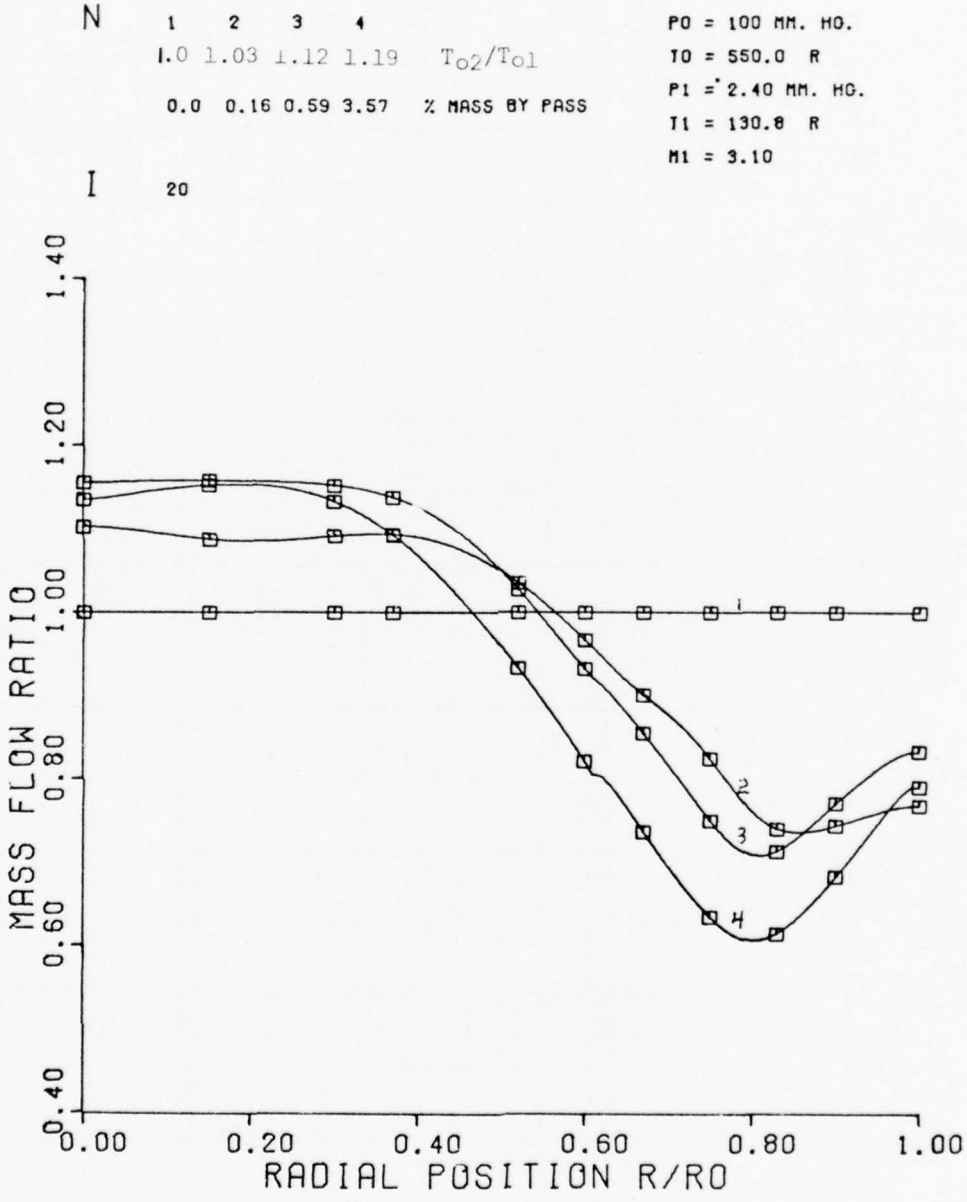

FIGURE 64 . MASS FLOW RATIO VS. RADIAL POSITION

TABLE 2

COMPARISON OF EXPERIMENT AND THEORY

Constant Area $\langle M_1 \rangle = 2.439$ $\langle M_2 \rangle = 2.07$

Averaging Method	T_2^o/T_1^o		P_2/P_1		T_2/T_1		P_2^o/P_1^o		ρ_2/ρ_1		V_2/V_1		S_2-S_1/R		$\dot{m}_2/\dot{m}_1$	
	Exp.	Theory	Exp.	Theory	Exp.	Theory	Exp.	Theory	Exp.	Theory	Exp.	Theory	Exp.	Theory	Exp.	Theory
$\int RdR$	1.125	1.052	1.405	1.337	1.322	1.292	0.802	0.799	1.081	1.035	1.000	0.965	0.427	0.350	0.993	0.998
$(\int RdR)_i$	1.110	1.052		1.337	1.303	1.292	0.802	0.799	1.094	1.035	0.997	0.965	0.392	0.350		0.998
$\int \dot{m} RdR$	1.074	1.051		1.335	1.351	1.291		0.798		1.034		0.964		0.349		0.998
$(\int \dot{m} RdR)_i$	1.060	1.050		1.334	1.334	1.290		0.798		1.034		0.964		0.348		0.997
$\int Pow/A\ RdR$	1.080	1.051		1.336		1.291		0.799		1.035		0.964		0.349		0.998
$(\int Pow/A\ RdR)_i$	1.075	1.051		1.335		1.291		0.798		1.035		0.964		0.349		0.997
Avg. Prop. $\int RdR$	1.095	1.051		1.336		1.292		0.799	1.046	1.035	0.984	0.964	0.398	0.350		0.998
Avg. Prop. $(\int RdR)_i$	1.090	1.051		1.336		1.291		0.799	1.060	1.035	0.977	0.964	0.364	0.350		0.998
Avg. Prop. $\int \dot{m} RdR$	1.070	1.051		1.335		1.291		0.798		1.034		0.964		0.349		0.998
Avg. Prop. $(\int \dot{m} RdR)_i$	1.061	1.050		1.334		1.290		0.799		1.034		0.964		0.348		0.997
Mea. From Collector	1.053															0.997
Theory Based on Collector		1.050		1.334		1.290		0.797		1.034		0.964		0.348		
Mea. From Flow Tube															0.998	
Theory Based on Flow Tube																0.997

TABLE 3

COMPARISON OF EXPERIMENT AND THEORY

Constant Area $\langle M_1 \rangle = 2.439$ $\langle M_2 \rangle = 1.821$

Averaging Method	T_2^o/T_1^o		P_2/P_1		T_2/T_1		P_2^o/P_1^o		ρ_2/ρ_1		V_2/V_1		S_2-S_1/R		$\dot{m}_2/\dot{m}_1$	
	Exp.	Theory	Exp.	Theory	Exp.	Theory	Exp.	Theory	Exp.	Theory	Exp.	Theory	Exp.	Theory	Exp.	Theory
$\int RdR$	1.300	1.102	1.757	1.652	1.743	1.561	0.686	0.691	1.055	1.058	1.008	0.933	0.876	0.611	0.972	0.987
$(\int RdR)_i$	1.260	1.102		1.649	1.687	1.561	0.686	0.690	1.090	1.056	0.990	0.933	0.791	0.613		0.985
$\int \dot{m} RdR$	1.185	1.102		1.641	1.734	1.562		0.687		1.050		0.933		0.620		0.980
$(\int \dot{m} RdR)_i$	1.148	1.103		1.633	1.676	1.563		0.684		1.045		0.933		0.625		0.976
$\int Pow/A\ RdR$	1.165	1.103		1.638		1.562		0.686		1.049		0.933		0.622		0.979
$(\int Pow/A\ RdR)_i$	1.145	1.103		1.633		1.563		0.683		1.045		0.933		0.626		0.975
Avg. Prop. $\int RdR$	1.190	1.102		1.642		1.562		0.687	1.034	1.051	0.973	0.933	0.761	0.619		0.981
Avg. Prop. $(\int RdR)_i$	1.171	1.103		1.638		1.562		0.686	1.077	1.049	0.954	0.933	0.660	0.622		0.979
Avg. Prop. $\int \dot{m} RdR$	1.140	1.103		1.631		1.563		0.683		1.044		0.933		0.627		0.974
Avg. Prop. $(\int \dot{m} RdR)_i$	1.125	1.103		1.627		1.563		0.681		1.041		0.933		0.631		0.971
Mea. From Collector	1.100															
Theory Based on Collector		1.104		1.616		1.565		0.676		1.033		0.940		0.639		
Mea. From Flow Tube															0.967	
Theory Based on Flow Tube																0.964

TABLE 4

COMPARISON OF EXPERIMENT AND THEORY

Constant Area $\langle M_1 \rangle = 2.439$ $\langle M_2 \rangle = 1.589$

Averaging Method	T_2^o/T_1^o		P_2/P_1		T_2/T_1		P_2^o/P_1^o		ρ_2/ρ_1		V_2/V_1		S_2-S_1/R		$\dot{m}_2/\dot{m}_1$	
	Exp.	Theory	Exp.	Theory	Exp.	Theory	Exp.	Theory	Exp.	Theory	Exp.	Theory	Exp.	Theory	Exp.	Theory
$\int RdR$	1.565	1.154	2.161	2.069	2.335	1.868	0.564	0.620	0.942	1.107	1.027	0.891	1.415	0.836	0.874	0.986
$(\int RdR)_i$	1.510	1.154		2.066	2.249	1.869		0.619	0.976	1.106	1.006	0.891	1.321	0.834		0.985
$\int \dot{m} RdR$	1.395	1.155		2.059	2.392	1.870		0.617		1.101		0.891		0.843		0.981
$(\int \dot{m} RdR)_i$	1.345	1.155		2.055	2.302	1.871		0.615		1.098		0.891		0.846		0.979
$\int Pow/A\ RdR$	1.230	1.157		2.036		1.874		0.610		1.087		0.892		0.859		0.969
$(\int Pow/A\ RdR)_i$	1.210	1.158		2.029		1.875		0.608		1.082		0.892		0.864		0.965
Avg. Prop. $\int RdR$	1.300	1.156		2.049		1.872		0.614	0.921	1.095	0.998	0.891	1.362	0.850		0.976
Avg. Prop. $(\int RdR)_i$	1.270	1.156		2.046		1.872		0.613	0.959	1.093	0.978	0.891	1.262	0.852		0.974
Avg. Prop. $\int \dot{m} RdR$	1.220	1.157		2.034		1.874		0.609		1.085				0.860		0.968
Avg. Prop. $(\int \dot{m} RdR)_i$	1.200	1.158		2.028		1.875		0.607		1.081				0.865		0.965
Mea. From Collector	1.180															
Theory Based on Collector		1.158		2.017		1.877		0.604		1.074		0.893		0.873		
Mea. From Flow Tube															0.957	
Theory Based on Flow Tube																0.959

TABLE 5

COMPARISON OF EXPERIMENT AND THEORY

A_2/A_1 = 1.60 $\langle M_1 \rangle$ = 2.479 $\langle M_2 \rangle$ = 2.526

Averaging Method	T_2^o/T_1^o		A_2/A_1		$\dot{m}_2/\dot{m}_1$		P_2/P_1		T_2/T_1		P_2^o/P_1^o		ρ_2/ρ_1		N	$\frac{f}{\tan}$
	Exp.	Theory	Exp.	Theory	Exp.	Theory	Exp.	Theory	Exp.	Theory	Exp.	Theory	Exp.	Theory	Exp.	
$\int RdR$	1.187	0.988	1.6	0.962	0.978		0.568		1.309		0.784		0.597		0.320	0.001
$(\int RdR)_i$	1.150	0.989		0.972					1.281				0.616		0.370	0.001
$\int \dot{m} RdR$	1.070	1.070		1.538					1.170						0.146	0.01
$(\int \dot{m} RdR)_i$	1.033	*1.032		1.585		0.998		0.620	1.138	1.007		0.661		0.616	0.070	*0.10
$\int Pow/A\ RdR$	1.055	1.054		1.574											0.115	0.05
$(\int Pow/A\ RdR)$	1.041	1.040		1.575											0.087	0.08
Avg. Prop. $\int RdR$	1.045	1.056		1.610									0.486		0.095	0.07
$(\int RdR)_i$	1.031	*1.031		1.590		0.993		0.618		1.005		0.658	0.499	0.615	0.066	*0.10
$\int \dot{m} RdR$	1.035	*1.035		1.547		0.998		0.616		1.004		0.657		0.611	0.074	*0.09
$(\int \dot{m} RdR)_i$	1.022	1.022		1.602											0.047	0.12
Mea. By Collector	1.031														0.066	*0.10
Theory Based on Collector		*1.031		1.590				0.618		1.005		0.658		0.615		
Mea. Flow Tube					0.998											
Theory Based on Flow Tube						0.998										

TABLE 6

COMPARISON OF EXPERIMENT AND THEORY

A_2/A_1 = 1.60 $\langle M_1 \rangle$ = 2.479 $\langle M_2 \rangle$ = 2.156

Averaging Method	T_2^o/T_1^o		A_2/A_1		$\dot{m}_2/\dot{m}_1$		P_2/P_1		T_2/T_1		P_2^o/P_1^o		ρ_2/ρ_1		N	$\frac{f}{\tan\theta}$
	Exp.	Theory	Exp.	Theory	Exp.	Theory	Exp.	Theory	Exp.	Theory	Exp.	Theory	Exp.	Theory	Exp.	
$\int RdR$	1.415	1.062	1.60	1.084	0.968	0.999	0.790		1.810		0.607		0.592		0.750	0.00
$(\int RdR)_i$	1.361	1.066		1.100		0.999			1.753				0.614		0.665	0.00
$\int \dot{m} RdR$	1.195	1.099		1.278		0.997			1.653						0.385	0.00
$(\int \dot{m} RdR)_i$	1.149	1.152		1.602		0.994			1.594						0.300	0.00
$\int Pow/A\ RdR$	1.160	1.132		1.470											0.321	0.00
$(\int Pow/A\ RdR)_i$	1.140	1.143		1.603		0.994									0.283	0.02
Avg. Prop. $\int RdR$	1.185	1.106		1.320									0.478		0.366	.000
$(\int RdR)_i$	1.165	1.125		1.430									0.496		0.330	.000
$\int \dot{m} RdR$	1.135	1.138		1.603		0.994									0.274	0.03
$(\int \dot{m} RdR)_i$	1.118	1.121		* 1.605		0.994		0.824		1.340		0.527		0.615	0.241	* 0.06
Mea. By Collector	1.120														0.245	* 0.06
Theory Based on Collector		1.122		* 1.602				0.826		1.342		0.530		0.616		
Mea. Flow Tube																
Theory Based on Flow Tube						0.994										

TABLE 7

COMPARISON OF EXPERIMENT AND THEORY

A_2/A_1 = 1.60 $\langle M_1 \rangle$ = 2.479 $\langle M_2 \rangle$ = 1.919

Averaging Method	T_2^o/T_1^o		A_2/A_1		$\dot{m}_2/\dot{m}_1$		P_2/P_1		T_2/T_1		P_2^o/P_1^o		ρ_2/ρ_1		N	$\frac{f}{\tan\theta}$
	Exp.	Theory	Exp.	Theory	Exp.	Theory	Exp.	Theory	Exp.	Theory	Exp.	Theory	Exp.	Theory	Exp.	
$\int RdR$	1.765	1.109	1.60	1.088	0.888		0.939		2.503		0.485		0.524		1.228	.0001
$(\int RdR)_i$	1.675	1.112		1.100					2.400				0.552		1.113	.0001
$\int \dot{m} RdR$	1.390	1.135		1.196					2.265						0.710	.0001
$(\int \dot{m} RdR)_i$	1.312	1.158		1.294					2.151						0.570	.0001
$\int Pow/A\ RdR$	1.231	1.206		1.520											0.440	.0001
$(\int Pow/A\ RdR)_i$	1.199	1.203		1.601											0.392	0.040
Avg. Prop. $\int RdR$	1.280	1.168		1.340									0.414		0.538	.0001
$(\int RdR)_i$	1.252	1.186		1.422									0.436		0.486	0.004
$\int \dot{m} RdR$	1.188	1.191		1.600		0.962		0.992		1.630		0.453		0.608	0.372	0.060
$(\int \dot{m} RdR)_i$	1.160	*1.164		1.603		0.962		0.978		1.592		0.446		0.614	0.320	*0.120
Mea. By Collector	1.190														0.375	
Theory Based on Collector		1.192		1.598				0.993		1.632		0.453		0.609		0.060
Mea. Flow Tube					0.963											
Theory Based on Flow Tube						0.962										

TABLE 8

COMPARISON OF EXPERIMENT AND THEORY

A_2/A_1 = 2.0 $\langle M_1 \rangle$ = 2.517 $\langle M_2 \rangle$ = 2.341

Averaging Method	T_2^o/T_1^o		A_2/A_1		$\dot{m}_2/\dot{m}_1$		P_2/P_1		T_2/T_1		P_2^o/P_1^o		ρ_2/ρ_1		N	$\frac{f}{\tan\theta}$
	Exp.	Theory	Exp.	Theory	Exp.	Theory	Exp.	Theory	Exp.	Theory	Exp.	Theory	Exp.	Theory	Exp.	
$\int RdR$	1.270	1.049	2.0	1.145	0.927		0.508		1.552		0.509		0.454		0.347	.0001
$(\int RdR)_i$	1.215	1.066		1.255					1.486				0.475		0.283	.000
$\int \dot{m} RdR$	1.091	* 1.091		1.997		0.999		0.589	1.424	1.201		0.464		0.490	0.12	* 0.10
$(\int \dot{m} RdR)_i$	1.052	1.053		2.016					1.371						0.074	0.16
$\int Pow/A\ RdR$	1.020	1.015		1.703											0.02	0.22
$(\int Pow/A\ RdR)_i$	1.083	1.003		1.831											0.00	0.24
Avg. Prop. $\int RdR$	1.032	1.031		1.963									0.357		0.04	0.19
$(\int RdR)_i$	1.015	1.011		1.660									0.371		0.02	0.23
$\int \dot{m} RdR$	0.983	0.987		1.686											-0.02	.28
$(\int \dot{m} RdR)_i$	0.970	0.983		1.500											-0.04	0.31
Mea. By Collector	1.080														0.11	
Theory Based on Collector		* 1.080		1.997				0.586		1.190		0.461		0.493		* 0.11
Mea. Flow Tube					0.998											
Theory Based on Flow Tube						0.999										

TABLE 9

COMPARISON OF EXPERIMENT AND THEORY

$A_2/A_1 = 2.0$ $\langle M_1 \rangle = 2.517$ $\langle M_E \rangle = 1.988$

Averaging Method	T_2^o/T_1^o		A_2/A_1		$\dot{m}_2/\dot{m}_1$		P_2/P_1		T_2/T_1		P_2^o/P_1^o		ρ_2/ρ_1		N	$\frac{f}{\tan\theta}$
	Exp.	Theory	Exp.	Theory	Exp.	Theory	Exp.	Theory	Exp.	Theory	Exp.	Theory	Exp.	Theory	Exp.	
$\int RdR$	1.620	1.117	2.00	1.171	0.855		0.662		2.283		0.407		0.408		0.700	.0001
$(\int RdR)_i$	1.495	1.130		1.233					2.082				0.432		0.583	.0001
$\int \dot{m} RdR$	1.350	1.168		1.430					2.076						0.436	.0001
$(\int \dot{m} RdR)_i$	1.232	1.238		2.023					1.950						0.303	0.038
$\int Pow/A\ RdR$	1.111	1.121		2.110											0.153	0.190
$(\int Pow/A\ RdR)_i$	1.083	1.083		1.994											0.116	0.250
Avg. Prop. $\int RdR$	1.145	1.147		2.006									0.318		0.197	0.158
$(\int RdR)_i$	1.184	*1.182		2.005		0.986		0.784		1.586		0.375	0.339	0.494	0.240	*0.108
$\int \dot{m} RdR$	1.065	1.064		1.960											0.092	0.280
$(\int \dot{m} RdR)_i$	1.040	1.049		2.320											0.057	0.290
Mea. By Collector	1.178														0.238	
Theory Based on Collector				2.019				0.778		1.587		0.373		0.490		*0.110
Mea. Flow Tube		*1.182			0.986											
Theory Based on Flow Tube						0.986										

TABLE 10

COMPARISON OF EXPERIMENT AND THEORY

A_2/A_1 = 2.0 $\langle M_1 \rangle$ = 2.517 $\langle M_2 \rangle$ = 1.641

Averaging Method	T_2^o/T_1^o		A_2/A_1		$\dot{m}_2/\dot{m}_1$		P_2/P_1		T_2/T_1		P_2^o/P_1^o		ρ_2/ρ_1		N	$\frac{f}{\tan\theta}$
	Exp.	Theory	Exp.	Theory	Exp.	Theory	Exp.	Theory	Exp.	Theory	Exp.	Theory	Exp.	Theory	Exp.	
$\int RdR$	1.751	1.235	2.0	1.300	0.814		0.680		2.931		0.288		0.353		0.812	.0001
$(\int RdR)_i$	1.670	1.248		1.346					2.787				0.370		0.745	.0001
$\int \dot{m} RdR$	1.295	1.298*		2.003		0.978		1.093	2.37	2.127		0.317		0.514	0.375	0.130*
$(\int \dot{m} RdR)_i$	1.235	1.232		1.977		0.979		1.079	2.258	2.020		0.313		0.534	0.306	0.21
$\int Pow/A\ RdR$	0.930	1.041		0.682											-0.106	.0001
$(\int Pow/A\ RdR)_i$	0.905	1.066		0.643											-0.145	.0001
Avg. Prop. $\int RdR$	0.935	1.039		0.676									0.286		-0.093	.0001
$(\int RdR)_i$	0.994	1.005		0.590									0.301		-0.009	.0001
$\int \dot{m} RdR$	0.864	1.064		0.744											-0.212	.0001
$(\int \dot{m} RdR)_i$	0.850	1.068		0.755											-0.236	.0001
Mea. By Collector	1.220														0.289	
Theory Based on Collector		1.246		1.982				0.999		2.043		0.290		0.489		0.21
Mea. Flow Tube					0.978											
Theory Based on Flow Tube						0.976										

To determine the friction factor for the constant area duct, the experimental average inlet and exit Mach numbers for cold flow were used in the ideal constant area friction factor equation:

$$\frac{4fL}{D} = \frac{1}{\gamma}\left[\frac{1}{M_1^2} - \frac{1}{M_2^2} + \frac{\gamma+1}{2}\ln\left\{\frac{M_1^2}{M_2^2}\cdot\frac{1+\frac{\gamma-1}{2}M_2^2}{1+\frac{\gamma-1}{2}M_1^2}\right\}\right] \qquad (126)$$

This equation gave a value of f = 0.0003. For the diverging duct the friction factor term f/tanθ was determined by using the initial and final average Mach numbers determined from the experiment for cold flow and varying f/tanθ until the proper area ratio was obtained. The value for f/tanθ was ≈ 0.093; however, to establish reasonable agreement between the measured and calculated total temperature ratios and the corresponding area ratio, it was necessary to correct the value of f/tanθ by multiplying it by the square root of the ratio of the wall temperature after heat addition to that before heat addition. The reason for the above is that in laminar flow, which was the experimental condition, the friction factor f is proportional to 1/Re which makes it proportional to the viscosity μ; f is the wall friction term. For a monatomic gas such as Argon the viscosity is proportional to $\sqrt{T}$; thus, as the gas temperature increases at the wall, one can expect the wall friction term to increase by $\sqrt{T}$. The values marked by an asterisk in Tables 2 through 10 represent those values close to the corrected f/tanθ term.

The values of N and n for use in the theoretical analysis were determined from the experimental data as follows. Total temperature ratio values were determined for the following cases:

1. $\int_0^R T^o R dR / \int_0^R R dR$

2. $\left(\int_0^R T^o R dR / \int_0^R R dR\right)_i$ (i → refers to ionization correction)

3. $\int_0^R T^o \dot{m} R dR / \int_0^R \dot{m} R dR$

4. $\left(\int_0^R T^o \dot{m} R dR / \int_0^R \dot{m} R dR\right)_i$

5. $2\pi \int_0^R Pow/A \; R dR$ → converted to total temperature
   (Pow/A → power per unit area)

6. $\left(2\pi \int_0^R Pow/A \; R dR\right)_i$ → converted to total temperature

Power per unit area written in terms of average properties and converted to total temperature where averages are determined as follows:

P → parameter

7. $\int_0^R P R dR / \int_0^R R dR$

8. $\left(\int_0^R P R dR / \int_0^R R dR\right)_i$

9. $\left(\int_0^R P \dot{m} R dR / \int_0^R \dot{m} R dR\right)$

10. $\left(\int_0^R P \dot{m} R dR / \int_0^R \dot{m} R dR\right)_i$

Knowing the area ratio and using the above total temperatures ratios, N was calculated from $T_2^o/T_1^o = (A_2/A_1)^N$. From the experimental flow rate measurements, n was determined by $\dot{m}_2/\dot{m}_1 = (A_2/A_1)^n$. All these cases are listed in Tables 2 through 10. For the constant area case, n and N were determined by letting A_2/A_1 be a number only slightly greater than one. Table 11 shows ionization values and electron temperatures for the constant area duct experiments as a function of radius.

TABLE 11

CONSTANT AREA DUCT

Double Probe Data for Three Total Temperature Ratios as Function of Radial Position

r/R	n_e			T_e			α		
	Particles/cc			°K			Ionization		
	X 10^{-13}			X 10^{-4}			X 10^{4}		
	T_2^o/T_1^o 1.05	T_2^o/T_1^o 1.10	T_2^o/T_1^o 1.18	T_2^o/T_1^o 1.05	T_2^o/T_1^o 1.10	T_2^o/T_1^o 1.18	T_2^o/T_1^o 1.05	T_2^o/T_1^o 1.10	T_2^o/T_1^o 1.18
0.0	0.092	0.531	0.665	2.58	2.44	3.87	0.023	0.121	0.161
0.095	0.115	0.706	0.811	2.00	1.800	3.50	0.029	0.165	0.208
0.190	0.180	1.235	1.078	1.37	1.12	3.06	0.043	0.278	0.271
0.381	1.279	2.684	1.559	1.00	1.13	3.95	0.297	0.601	0.376
0.475	1.570	4.461	4.726	0.805	1.10	2.10	0.398	1.079	1.236
0.571	1.235	7.063	7.018	1.18	1.18	1.77	0.327	1.752	2.047
0.700	2.984	9.114	9.150	1.51	1.47	1.84	0.738	2.305	3.141
0.762	3.412	8.379	8.497	1.40	1.53	1.90	0.911	2.521	3.669
0.820	2.984	5.566	6.205	1.33	1.66	2.04	1.026	2.234	3.417
0.856	2.643	3.797	4.798	1.20	1.79	2.19	1.177	1.989	3.183
0.909	1.699	3.272	3.421	1.11	1.20	2.10	1.203	2.472	2.995
1.00	0.0	0.0	0.0	0.0	0.0	0.0	0.0	0.0	0.0

SECTION VI

SUMMARY AND CONCLUSIONS

Experiments

The flow analyzed was heat addition to a supersonic flow of Argon gas passing through a 4 3/4-inch long Boron Nitride (B.N.) duct with a one-inch diameter inlet. The duct was located one-half inch downstream of an axisymmetric nozzle. The nozzle, designed for parallel flow at the exit, had a one-inch exit diameter and a stagnation chamber pressure and temperature of 100 mm Hg and 550°R. The center line Mach number at the duct entrance was approximately 3.1, while the average across the duct diameter was about 2.5. The flow inside the duct contained compression and expansion regions which were a result of the flow not entering exactly parallel to the duct inlet lip. These compression and expansion regions remained essentially the same during heat addition to the gas. The static pressure in the gap between the nozzle exit and duct entrance was maintained constant by a small mass flow bleed which could be decreased to compensate for any mass flow bypass caused by heat addition to the gas flow.

Heat was added to the supersonic duct flow by means of a one and one-half inch long R.F. copper coil wrapped around the B.N. duct and connected to a five Kilowatt Lepel R.F. power supply. Experiments were made with ducts having area ratios of 1.0, 1.6, and 2.0. For

each duct, three heat addition values were investigated. The necessary measurements were made with a static pressure probe, a total pressure probe, a total temperature probe, and a Langmuir double probe. The probes were made of ceramic to avoid interference with the R.F. discharge and to withstand the high temperature environment. Static and total pressure measurements were made at five different radial positions along the length of the duct. The double probe and total temperature measurements were made only at the duct exit because the double probe was too large to insert without drastically changing the flow and the thermocouple began to interact with the R.F. coil when inserted about one-half inch into the duct exit. The double probe was used to measure ionization levels so that a correction for ion-electron recombination could be made to the total temperature probe measurement.

A water table experiment was performed to determine if the hydraulic analogy would qualitatively predict the flow phenomena for heat addition to a supersonic gas. Heat addition was simulated by water mass flow addition to a stream of supersonic water. The mass addition was accomplished by injection through a porous plate beneath the main water stream. A properly-contoured wood nozzle provided the Mach 2 water flow and the duct walls were made of plexiglas for visual observation of the water height. The results of this experiment qualitatively showed the same pressure (water height) profiles along the duct as observed in the gas experiments.

Radial and Axial Variations for Gas Experiments

The graphs presented in Figures (50) to (64) illustrate the radial and axial property variations for the 1.6 area ratio duct. The Mach

number profiles are fairly flat out to about 0.7 of the radius and show the proper trend for heat addition, that is, decreasing with increasing heat input. The graph of static pressure versus axial position illustrates two important points. First, the pressure rise due to heat addition propagates upstream into the inlet even though the flow is supersonic and second, the pressure first increases and then decreases within the duct for the two highest heating values. The upstream pressure rise can only be due to the subsonic portion of the boundary layer which permits the pressure disturbance from heat addition to propagate upstream into the inlet region, causing mass flow spillage. The pressure rise and decrease within the duct can be explained if a separation region occurs within the duct and reattaches near the duct exit. The graphs of density ratio and mass flow ratio in Figures (62) and (64) show that density and mass flow both decrease near the wall and increase in the center region of the duct. Therefore, this could indicate a converging of the streamlines caused by heat addition and separation due to an adverse pressure gradient. From Shapiro [8], Vol II, the pressure ratio necessary for separation of a laminar boundary layer interacting with a shock wave can be written $P_2/P_1 = 1 + 1/2\ \gamma M_1^2 \cdot f$ (Reynolds number). For the conditions in the experiment, P_2/P_1 is equal to $1 + .05\ \gamma M_1^2$. For $M_1 = 3.1$, we find $P_2/P_1 \simeq 1.8$ which is exceeded in the higher heat input values between the inlet and center of the duct; thus, separation is a possibility. Separation causes an effective decrease in flow area which increases the static pressure in a supersonic flow. A separation thickness of about 0.065" would result in a pressure ratio of about two as a result of the decrease in flow area.

The magnetic pressure force was estimated to be on the order of 0.001 mm Hg near the wall and hence should not be a significant factor in flow separation since the duct pressure is on the order of 4 mm Hg or higher.

The wave pattern observed in the duct could be the result of the interaction of the oblique shock wave with a laminar boundary layer as discussed in Shapiro, page 1141, Vol. II [8]. The interaction, however, implies a separated zone which occurs at a pressure ratio less than that mentioned above. According to Young [26], a pressure rise due to a shock wave impinging on a laminar boundary layer can extend 100 boundary layer thicknesses upstream of the intersection point. This upstream influence will occur whether the boundary layer separates or not. Thus, the pressure disturbance from heat addition can likewise propagate upstream a substantial distance due to the subsonic part of the boundary layer. This upstream pressure propagation causes a thickening of the boundary layer which effectively increases the flow area and hence increases the duct static pressure. The large pressure rise and decrease within the duct during heat input could be due to a combination of two phenomena. The pressure variation can be caused by the flow separation discussed previously; and, secondly, the heating and expansion of the gas in the R.F. coil region forces mass towards the center of the duct resulting in an effective area decrease. Following this rapid heating, radial conduction of heat occurs, thus relieving the pressure.

The figures for static and total temperature show that most of the temperature rise occurs within a region out to about 1/2 the duct

radius from the wall. This region occurs because the R.F. discharge tends to shield the interior flow from the electric and magnetic fields of the coil. This shielding can be considered similar to the skin effect in a metal conductor. Figure (63) for power vs. radial position illustrates that even though the center region of the duct receives little R.F. heating, the power per unit area increases largely due to the heated gas near the wall forcing mass flow into the center region of the flow.

From the plot of average total pressure along the duct axis, it is observed that the total pressure tends to decrease along the duct with heat addition and then increases again before reaching the exit. This trend is due to errors in the measured total and static temperatures. As mentioned in the section entitled Gas Flow Experiments, a -5% error in measured static pressure and a 5% error in impact pressure can lead to a 20% error in calculated total pressure. Thus the fluctuations of average total pressure along the axis is not surprising. Figure (55) shows total pressure as a function of radius at the duct exit; the total pressure decreases with increasing heat input as it should in a supersonic flow with heat addition.

Average Properties for Gas Experiments

A quasi-one-dimensional theory based on average properties (averaged with respect to radius) was developed using the assumptions $(T_2^o / T_1^o) = (A_2/A_1)^N$; $\dot{m}_2/\dot{m}_1 = (A_2/A_1)^n$, where N and n are variable parameters. The above two assumptions are reasonable since eight special flow conditions can be described by them (see section entitled Flow Equations). In general, one can, by using N and n as variable

parameters (and including wall friction by means of the friction factor, f), analyze flows in axisymmetric ducts with area change, energy exchange, and variable mass flow occurring simultaneously. The theory was developed to compare with the experimental results.

Tables 2 through 10 show the calculated average experimental results with those calculated by the quasi-one-dimensional theory. The N and n required were determined from the total temperature averages discussed in the section entitled Gas Flow Experiments and the measured mass flows. The initial and final Mach numbers needed for the theoretical inputs were based on the average inlet Mach number before heat addition and the average Mach number at the exit after heat addition.

It is seen from the above tables that averaging by $\int_0^R T^o \dot{m} R dR / \int_0^R \dot{m} R dR$ was more appropriate than averaging by $\int_0^R T^o R dR / \int_0^R R dR$ as assumed in the quasi-one-dimensional theory. The reason is that an energy change (which is related to the total temperature or static temperature) is a unit mass property and when significant radial variations exist, a substantial error can be obtained by averaging by RdR. The static temperature also agreed better with theory when averaged by $\dot{m}RdR$. Total temperature measured by the probe can sense the energy released by electron-ion recombination; this energy release was taken into account by the ionization level determined from the Langmuir double probe; and, averages with and without the ionization correction are shown in Tables 2 through 10. In most cases, correcting for ionization gave closer agreement with the theoretical values.

The experimental static temperature was always higher than the theoretical value which indicates the total temperature probe probably

read too high a value; this difference in temperature may be due to the error in the ionization level correction, which could be off by an order of magnitude of two. The static pressures agreed fairly well between theory and experiment and surprisingly the total pressure also agreed well in many cases. The value of $f/\tan\theta$ for the diverging area ducts was $\simeq 0.093$ as determined from the cold flow (no heat addition) condition. The values of Tables 5 through 10 were obtained by varying $f/\tan\theta$ until the correct area ratio was obtained for a given duct and heat addition value. The correct area ratio was obtained in the majority of cases for $f/\tan\theta$ close to 0.093 multiplied by the temperature correction discussed in the section entitled Gas Flow Experiments and corresponded to averages based on $\dot{m}RdR$ and corrected for ionization.

Figure (65) illustrates the average total pressure variation with increasing average T_2^o/T_1^o and increasing area; the trend is correct, decreasing for increasing T_2^o/T_1^o and decreasing for increasing area which implies energy addition at a higher Mach number. Figure (66) illustrates the mass flow ratio bypass with heat addition for constant area and diverging ducts; again the trend is correct, the mass bypass is decreased with increasing area for a given energy input because of the pressure relieve offered by a larger area duct.

Conclusions

A steady, radially non-uniform weak detonation wave corresponding to point c of Figure (1) was simulated by R.F. heating of a supersonic Argon gas flow. The quasi-one-dimensional theory based on average properties, where $T_2^o/T_1^o = (A_2/A_1)^N$ and $\dot{m}_2/\dot{m}_1 = (A_2/A_1)^n$ can

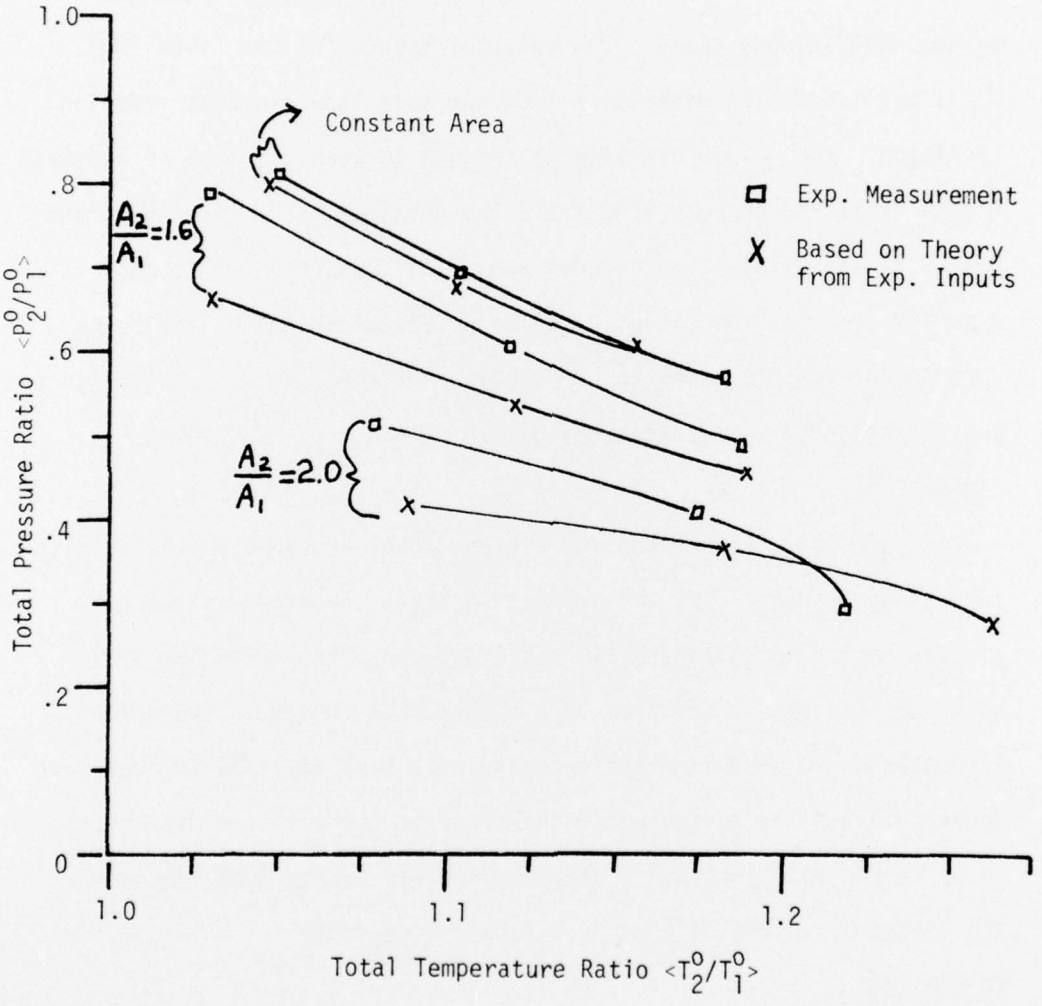

Figure 65. Total Pressure Ratio vs. Total Temperature Ratio for Constant Area and Diverging Ducts.

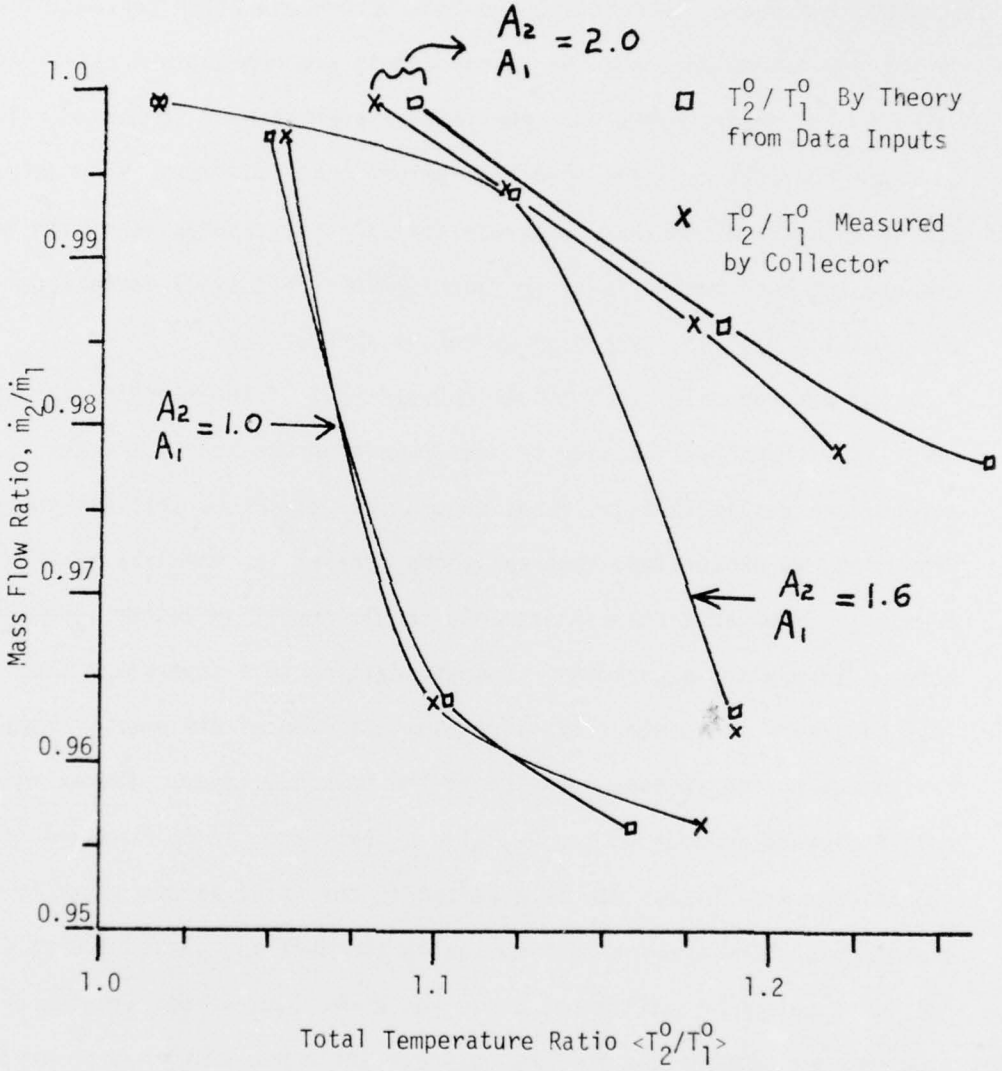

Figure 66. Mass Flow Ratio Caused by Heat Addition vs. Total Temperature Ratio for Constant Area and Diverging Ducts.

satisfactorily describe the weak detonation mode for constant and varying area ducts, even though the flow before and after heat addition is not one-dimensional and the energy inputs are non-uniform across the radius. The theory works when the initial average Mach number $\langle M_1 \rangle$ is based on the initial inlet condition before heat addition. When determining an average temperature across the radius for comparison with the theory, the best method is by $\int_0^R \dot{T}_m R dR / \int_0^R \dot{m} R dR$. For small variations in the radial direction, averaging by RdR is appropriate.

The discrepancies that appear between some of the experimental and calculated properties are due to measurement errors which, however slight, can result in significant errors for quantities that are computed from measured properties; this was shown earlier for the case of total pressure. More accurate measurements should result in better agreement between theory and experiment. Energy addition to a supersonic flow in a real situation can cause a pressure rise upstream of the energy input region due to the subsonic portion of the boundary layer. The extent of this influence depends on the Reynolds number; and, if it is small enough, significant mass bypass can be expected at the inlet as was shown in the experiments. The average Mach number in the duct approached 1.0 only in one instance, and in all other cases was above 1.0; hence, choking of the flow was not responsible for the upstream influence which was observed. The water table experiments qualitatively exhibited the same phenomena seen in the gas flow tests, thus validating its use for gaining an insight into gas flow energy addition. An electric double probe was built to measure ionization levels in a supersonic gas stream and it functioned well. The equation developed for the degree of ionization

was derived by analyzing the theories of Cohen, Waymouth, and Lam for dense plasmas. It was shown that all three theories, although of different initial form, reduced to the same expression for the case of ion collection at large negative potentials and electron temperatures much greater than ion or neutral temperatures.

When a practical supersonic combustion engine is developed, it may rely on the combustion or energy addition occurring near the wall region as in these experiments; so, the test results obtained here should provide an insight to the problems to be encountered in high altitude supersonic combustion. As was mentioned in the Introduction, supersonic energy addition can be by a subsonic diffusion flame propagating in a supersonic stream or by a weak detonation wave which travels at a supersonic speed relative to both the heated and unheated gas. The latter is difficult to obtain with a chemical reaction, but was simulated in these experiments with R.F. heating. However, energy addition by R.F. was not assumed to be a practical means of energy transfer, but only a method to achieve a weak detonation without resorting to a reacting gas mixture. To be practical, R.F. energy addition efficiency must be greatly increased over the 10% which was measured in a "dummy" load test.

The effort has added to the knowledge of energy exchange with a flowing gas by analyzing non-uniform (radially), low Reynolds number (35,000), varying area supersonic energy addition. The major energy input was restricted to a region near the wall of the duct. A future effort may be one that adds energy to the center of the duct by passing an electric arc along the center line. This would add the energy in a region of high Mach number compared to the wall region; for the same

energy input, it would be interesting to see if the results are the same as in the present work. If the results are equivalent, then this would help confirm the averaging method proposed and the quasi-one-dimensional theory outlined earlier. Another area that could be explored is a non-steady theory that can predict for supersonic heat addition, the upstream pressure rise which propagates in the subsonic portion of the boundary layer; in the ideal supersonic theory there is no upstream influence as long as no choking occurs. The achievement of a steady weak detonation wave in a chemically-reacting gas mixture must wait the development of a highly efficient, low power mechanism (perhaps laser radiation) which will initiate and sustain the chemical reaction in a small region.

REFERENCES

1. MacKay, J., and Weber, R., "An Analysis of Ramjet Engines Using Supersonic Combustion," NACA TN 4386, September, 1958.

2. Billig, F. S., "Supersonic Combustion of Storable Liquid Fuels in Mach 3 to 5 Air Streams," Tenth Symposium (International) on Combustion, The Combustion Institute, Pittsburgh, Pennsylvania, 1965, pp 1167-1178.

3. Cookson, R., Flanagan, P., and Penny, G., "A Study of Free-Jet and Enclosed Supersonic Diffusion Flames," Twelfth Symposium (International) on Combustion, 1969, pp 1115-1123.

4. Levy, M. E., Cerkanowicz, A. E., and McAlvey, R. F., III, "Ignition of Subatmospheric Gaseous Fuel-Oxidant Mixtures by Ultraviolet Irradiation," AIAA Paper No. 69-88, New York, January, 1969.

5. Edse, R., Rice, E. E., and Kitzmiller, C. T., "Supersonic Combustion and Burning in Ramjet Combustors," 1973, The Ohio State University, AFOSR-TR-73-2025.

6. Oppenheim, A. K., "Water-Channel Analog to High Velocity Combustion," Journal of Applied Mechanics, March, 1953, pp 115-121.

7. Tearnen, J. O., "A Water Channel Analogy to a Problem in Gaseous Combustion," Dissertation, Mechanical Engineering Dept., University of California, November, 1951.

8. Shapiro, A. H., The Dynamics and Thermodynamics of Compressible Fluid Flow, Vol. I & II, N.Y. The Ronald Press Co., 1953.

9. Langmuir, I., and Mott-Smith, H. M., General Electric Review, 27, 1924.

10. Johnson, E. O., and Malter, L., "A Floating Double Probe Method for Measurements in Gas Discharges," Physical Review, 80, October, 1950, pp 58-68.

11. Waymouth, J. F., "Perturbation of a Plasma by a Probe," The Physics of Fluids, Vol. 7, No. 1, November, 1974, pp 1843-1854.

12. Cohen, I. M., "Asymptotic Theory of Spherical Electrostatic Probes in a Slightly Ionized Gas, Collision-Dominated Gas," The Physics of Fluids, Vol. 6, No. 10, October 1963, pp 1492-1499.

13. Lam, S. H., and Su, C. H., "Continuum Theory of Spherical Electrostatic Probes," The Physics of Fluids, Vol. 6, No. 10, October 1963, pp 1479-1491.

14. Danikov, V., and Gruglyakov, E., "Cylindrical Probe in Nitrogen Plasma of Glow Discharges at Mean Pressures," FTD Translation, December 17, 1973.

15. Schulz, G. J., and Brown, S. C., "Microwave Study of Positive Ion Collection by Probes," The Physical Review, Vol. 98, No. 6, June 15, 1955, pp 1642-1649.

16. Huddlestone, R. H., and Leonard, S. L., Plasma Diagnostic Techniques, New York-London: Academic Press, 1969.

17. Hurnov, E., and Hirschberg, J. G., "Electron-Ion Recombination in Dense Plasmas," The Physical Review, Vol. 125, No. 3, February, 1962, pp 795-801.

18. Chen, Che Jen, "Partition of Recombination Energy in the Decaying Rare-Gas Plasmas," The Physical Review, Vol. 163, No. 1, November, 1967, pp 1-7.

19. Brown, S. C., Basic Data of Plasma Physics, New York: John Wiley & Sons, Inc., 1966.

20. Foelsch, K., "The Analytical Design of an Axially Symmetric Level Nozzle for a Parallel and Uniform Jet," Journal of the Aeronautical Sciences, 1949, pp 162-164.

21. Goldstein, D., and Scherrer, S. "Design and Calibration of a Total-Temperature Probe for Use at Supersonic Speeds," NACA Technical Note No. 1885, May, 1949.

22. Eber, R. G., "Shielded Thermocouples," Physical Measurements in Gas Dynamics and Combustion, Princeton Series, 1954, pp 186-197.

23. Bontrager, P. J., "Development of Thermocouple Type Total Temperature Probes in the Hypersonic Flow Regime," M.S. Thesis, The University of Tennessee Space Institute, March, 1968.

24. Wuest, W., "Measurement of Flow Spread and Flow Direction by Aerodynamic Probes and Vanes," 30th Flight Mechanics Panel Meeting, Montreal, Canada, June, 1967.

25. Sherman, F. S., "New Experiments on Impact-Pressure Interpretation in Supersonic and Subsonic Rarefied Air Streams," NACA Tech. Note 2995, University of California, 1953.

26. Young, A. D., "Boundary Layers," Modern Developments in Fluid Dynamics High Speed Flow, Vol. I, Oxford, 1953, pp 375-475.

27. Pope, A., "Wind Tunnel Calibration Techniques," NATO AGARDograph 54, April, 1961.

28. Billig, F. S., and Dugger, G. L., "The Interaction of Shock Waves and Heat Addition in the Design of Supersonic Combustors," Twelfth Symposium (International) on Combustion, 1969, pp 1125-1139.

29. Francis, G., Ionization Phenomena In Gases, Academic Press, 1960.

☆ U. S. GOVERNMENT PRINTING OFFICE: 1976 — 757-001/4